UNIVERSITY OF
BIRMINGHAM

Study, investigate and fabricate optical nanostructures and devices using advanced techniques and novel materials

By

Ijaz Rashid

A thesis submitted to

The University of Birmingham

for the degree of

DOCTOR OF PHILOSOPHY

December 2019

School of Engineering

The University of Birmingham

Abstract

This thesis covers studies on nano-photonic bandgap structures and devices inspired from nature, with the potentials to be used as filters and smart sensors such as hydrogel based photonic bandgap sensors for detection in various industries including medical applications, food and cosmetics. Research was conducted on two samples of feathers that exist in nature namely Nicobar pigeon and Monal pheasant bird species in order to study the structural colouration originating from the internal barbule nanostructures. The structural colouration of these species have not been studied or reported anywhere else before. Optical microscopy and spectroscopy measurements were performed showing a variety of colours observed with change in illumination and viewing angle. The variation in colour observed is reflected by red, green and blue photonic bandgap structures present in the internal structure of the feathers. Hydrophilic and Hydrophobic properties of the optical material were also investigated. Contact angle measurements were performed resulting in ~ 156° in the case of Nicobar pigeons demonstrating it to be super hydrophobic whereas a contact angle of ~ 120° was recorded in case of Monal pheasant. Feathers were also immersed in different liquids and the spectral shifts were recorded and analysed which were correlated with the refractive indices of these liquids. The structural colouration in Nicobar pigeon and Monal pheasants can be mimicked for applications such as colour filters, non-reflecting coating, bio sensors, photonic bandgap hydrogel sensors and sensors based on refractive indices used in food, medical, health monitoring and cosmetic industries.

To support the theory, a simple silica thin film grating structure was designed using silicon and silicon dioxide having different refractive indices. The structure was simulated with variation of various parameters in order to get the best colour change. Two samples were successfully fabricated for testing and confirmation purposes. Both concepts of thin film and diffraction

grating were in combination and the mechanism was studied in detail. Titanium nanostructures were also fabricated with varied dimensions in size using laser interference ablation method in order to study the interaction of a liquid droplet with nanostructures. The change in hydrophobicity with respect to change in nanostructure size was captured, analysed and studied in detail. A surface profile with large spacing and size in nanostructures prevents the absorption on the surface with availability of wider channels for the liquid's excessive flow allowing very low contact angles whereas very narrow and smaller size of nanostructures allow no wettability with ability of nanostructures to hold the liquid drop resulting higher contact angles.

The main focus was to explore more on photonic bandgap structures that exist in nature and have not been investigated and suggest their possible use in applications such as integration in hydrogel based photonic bandgap sensors to enhance fast and facile fabrication with simple detection methods using change in physiological conditions of the photonic bandgap structure integrated in the hydrogel.

Dedicated to my parents

Acknowledgements

First and foremost, I would like to take the opportunity to deeply thank Dr Haider Butt for his supervision and guidance. His insight and enthusiasm enriched my ambitions for science. He always encouraged me with a positive attitude and a stream on new ideas and advices for which I am greatly thankful. I would also like to express my gratitude to Dr Carl Anthony for being my supervisor. I thank him for his invaluable feedback and support.

I am greatly indebted to Dr Raya Al-Dadah for everything she has done to make it possible for me to complete my research whether its school funding issues, progress reviews, PGR Seminars, and even desk allocations, her kindness and thoughtfulness has humbled me and I am grateful to her.

My particular thanks to Dr Muhammad Umair Hassan, Dr Ali Yetisen, Dr Aydin Sabouri, and Dr Daniel Espino for reviewing my work and giving me feedback.

I would also like to thank all the collaborators namely Dr Affar Karimullah, Dr Qing Dai, Rayan Ameen, Dr Bruno Dlubak and his team for remarkable contributions they have done to my research work.

I thank my fellow friends Tawfiq, Mohamed Elsherif, Bader and Yousaf for their help and support. Thank you guys!

I owe special thanks to my wife Sadia for her patience and endless support.

Table of Contents

List of Figures

Chapter 2

Chapter 3

Chapter 4

Chapter 5

Appendix A

Appendix C

Nomenclature

$\overline{E}$ /E	Electric Field	$\overline{H}$ /H	Magnetic Field
$\overline{D}$	Electric Flux Density	$\overline{B}$	Magnetic Flux Density
$\overline{J}$	Electric Current Density	$\overline{\rho}$	Electric Charge Density
ε_0	Free-Space Permittivity	μ_0	Free-Space Permeability
ε_r	Relative Permittivity	μ_r	Relative Permeability
λ	Wavelength	θ	Angle
T	Transmission	R	Reflection
d / Λ	Grating Period	φ	Phase
i	Incident Light	r	Reflected Light
Φ	azimuthal angle	η	Efficiency
θ_m	Diffraction angle for order m	n	Refractive Index
δ	Extra path length travelled by light in a thin film layer	A_r	Amplitude of reflection
E	Energy	I	Intensity
v	Speed of wave	h	Height
c	Speed of light	A	Amplitude

Abbreviations

BF	**B**right **f**ield
DF	**D**ark **f**ield
FT	**F**ourier **T**ransform
IFT	**I**nverse **F**ourier **T**ransform
SEM	**S**canning **e**lectron **m**icroscopy
TEM	**T**ransmission **e**lectron **m**icroscopy
CIE	**C**olour **i**llumination **e**ffect
1D	**O**ne **D**imensional
2D	**T**wo **D**imensional
3D	**T**hree **D**imensional
PC	**P**hotonic **C**rystal
DC	**D**irect **C**urrent
UV	**U**ltra**v**iolet
AFM	**A**tomic **F**orce **M**icroscopy
PECVD	**P**lasma **e**nhanced **c**hemical **v**apour **d**ecomposition
DLIP	**D**irect **L**aser **I**nterference **P**atterning
Nd:YAG	**N**eodymium-**d**oped **y**ttrium **a**luminium **g**arnet
DI	**De**i**o**nised
mM	**M**illi**m**olar
nm	**n**ano**m**eter
SPR	**S**urface **P**lasmon **R**esonance
SERS	**S**urface **E**nhanced **R**aman **S**cattering
PBG	**P**hotonic **B**and**g**ap

Chapter 1: Introduction

1.1 Background

Our ability to see objects and identify them is based on the basic concept of light reaching to our eye and providing us information. Our eye can detect the colour, shape and size of the objects around us with the help of light waves in the wavelength range of approximately 400 nm to 700 nm. The majority of the objects we see; their colours are from pigments on the surface or in the body of the object. However, some bright colours seen around us in nature are due to the interaction of light with micro and nanostructures on the surface of these objects or embedded inside their structure along with or without the presence of any dyes or pigments. These colours are produced due to coherent scattering, interference, refraction and diffraction of light from their internal structures hence known as structural colours. These structural colours are caused by modulation of light with these periodic structures known as photonic bandgap structures that determine the colour (particular wavelength of light) to be seen.

Structural colours have been an interest to researchers for many years. The earliest recorded study of iridescence of birds' feathers is found in Robert Hooke's book Micrographia (1665) [1], in which he researched on Peacock feathers and discovered the effect of colour changes in different refractive index media. However, birds are not the only species which possess these colours; –insects [2-12], marine life [13-18], and plants [19-24] also exhibit pure structural colouration beside some examples combining structural colourations with colourants or pigments [25]. Morpho butterflies [10], beetles [11] and dragonflies [12] show iridescent colouration purely due to their complex structural nanoscale features on their wings and bodies. Irish moss also possesses layered structure in its cuticles, where organization and dimensions of lamellae are responsible for its blue colour [17]. Bragg gratings and multilayer reflectors are responsible for vivid colours of marine crustaceans [15]. Anhydrous guanine-based biogenic

photonic crystal plates have been reported to be found in fish and spiders [18]. Additionally, the pointillist appearance of blue *Pollia* fruit is because of its multilayer stacks of cells[23]. Such structural colouration in nature has evolved to provide Batesian mimicry, camouflage, conspecific recognition, predation, signal communication, and mating behavior.

Many species of birds show structural colours [26-33]. Multiple optical processes can also be simultaneously present in one species [34]. Combination of these different optical processes complements each other to generate brilliant colours. Optical effects occur mainly because of photonic bandgap structures including thin films [35], multilayer Bragg reflectors [26] and diffraction gratings [36]. The iridescent colouration of specula of ducks is because of the single 2D hexagonal lattice of melanosomes as well as thin film of keratin [30]. Feathers of hummingbirds exhibit brilliant colour because of optical periodic arrays containing layered air gaps [37]. Investigation of structural colouration and underlying nanoscale architecture has led to many practical applications through adopting modern synthetic routes and nanofabrication techniques to bioinspired replication of nanophotonic structures [38-44]. Their applications include self-cleaning surfaces [42], colour-selective filters [44] and antireflective coatings [45], sensors [46], supercapacitors [47], fabrics [48], tough materials [49], and art [50].

Development in the field of scanning and transmission electron microscopy has increased the interest of scientists to study and investigate micro and nanostructures having unique optical behaviours and characteristics that may address existing optical problems such as strong light polarisation, spectral filtering, high reflectivity and as well as contribute towards the field of optical sensing, optical filters, biomedical sciences, food, cosmetics and security industry. Photonic bandgap structures have been widely used in optical biosensors [51]. Optical hydrogel sensors have been fabricated through soft nanoimprint lithography techniques and they act as photonic band gap sensors for detecting and sensing glucose concentrations [52-54]. Diabetes being a major chronic illness affecting millions of people worldwide also has a significant

burden on costs in healthcare. It requires constant monitoring of glucose levels in blood to inject the right amount of insulin. Long term fluctuations in glucose levels can lead to seizures, kidney failure, neurotherapy, pain in muscles and cardiovascular diseases. Measurements on concentrations of glucose are conventionally done by pin prick methods which cannot be performed frequently due to pain and inconvenience and carry the potential risk for infections. Glucose sensors based on optical sensing have been under study for the last decade. They are classified under four main optical phenomena which are Surface Plasmon Resonance (SPR) [55], Surface Enhanced Raman Scattering (SERS) [56, 57], Fluorescence [58, 59] and Photonic bandgap (PBG) sensors [60-63]. The fabrication of first two types (SPR and SERS) requires costly and complicated methods such as high vacuum, atomic layer deposition, e-beam lithography and high cost optic fibres or Raman Spectrometers for detecting the change. Fluorescent sensors have the disadvantage of photo bleaching of the fluorophore and the variation in illumination can cause error of higher or lower levels of detection effecting the accuracy of the results. Photonic bandgap structures have been integrated in hydrogels to fabricate photonic bandgap based hydrogel sensors. These hydrogel photonic bandgap sensors are reversible and have the tendency to detect glucose, pH, ionic strength, temperature, humidity and biomolecule binding. They are sensitive to volumetric change in the hydrogel and this change can be detected through optical methods. These sensors can be classified as 1D, 2D and 3D photonic bandgap sensors depending on the refractive index and dimension of the integrated photonic bandgap structure. The detection in change is recorded by colorimetric and spectral peak shift measurements. Silver, gold and polystyrene particles have been used previously to form composite layers separated by hydrogel layers modulating the refractive index in that particular dimension. However, these sensors require a well ordered monolayer of particles demanding high optimisation techniques in fabrication. The type of photonic bandgap structure integrated with hydrogel plays a significant role in the sensor device towards sensing

the change. This research work focuses on exploring more on photonic bandgap structures that exist in nature and suggests their integration in hydrogel photonic bandgap sensors to enhance fast and facile fabrication with simple detection methods using change in physiological conditions of the photonic bandgap structures based hydrogel.

1.2 Overview

In this work, we present two unique studies that were conducted on structural colouration in birds from two different bird species that exist in nature and have not been reported before. The inspiration was to learn from nature and contribute towards manufacturing artificial nature inspired photonic bandgap sensor devices and systems with less complexity but better performance. The complex photonic bandgap structures observed were analysed in detail. Two novel devices were also fabricated for experimental study of the phenomena.

The first study is on the Nicobar pigeon (*Caloenas Nicobarica*) which belongs to the extinct dodo-bird family. Microscopic and spectroscopic measurements were carried out on the bird's feathers to study the structural coloration originating from the barbule nanostructures. A range of colour shades was recorded with changing viewing and illumination angles at different locations of the feathers. A spectacular variation in colours is generated by photonic bandgap structures; red, green and blue and their blends were observed. Hydrophobicity of the optical material has also been investigated. Experimental observations of the optical properties were analyzed on these feathers for sensing made possible due to the material and structural properties at the interface between barbule's surface and solution.

The second study was conducted on Himalayan Monal which is a bird in the pheasant family, and it is the national bird of Nepal. The bird possesses spectacular iridescent plumage with a range of different metallic colours. The internal structure of its feathers was explored from different parts of the bird's body. It showed that the beautiful colours and irrediscence are

due to photonic bandgap structures present in the internal structure of the feathers. Sharp changes in the reflected brilliance were observed from the feathers upon changing the illumination conditions, such that, horizontal and azimuthal angles. Hydrophobicity was studied and optical responses were recorded. Liquids with varied refractive indices were used to analyse and sense the change in response due to the phenomenon of the liquid drop being absorbed by the feather barbules.

Two different novel devices were designed and fabricated using Si and SiO_2 materials to understand the colour selective mechanism of nanostructures with their interaction with light. Refractive index modulation of light and its properties were studied in detail. The first device simulated and fabricated was a reflective diffraction grating with a periodic square-wave profile which has combine effects of thin-film interference with conventional grating behaviour when composed of features having different refractive index than that of the substrate. Finite element analysis was used to study nanostructures having a multirefractive index grating and a conventional single material grating. A sample device was fabricated for optical characterisation and experimental purposes.

The second device fabricated was based on the assumption that a nanostructured surface profile can influence the interaction between the surface and the material in contact. Hence change in contact angle will change the hydrophobicity of the surface. Nanostructures were fabricated with different shape and dimensions such as circular ring structures, 1D and 2D grating with different periods on titanium surface using an alternate fast direct laser interference patterning method and, demonstrated changes in their hydrophobicity with respect to change in size, shape and surface roughness of these nanostructures as the parameters to control the wettability and hydrophobicity properties required for any specific application.

1.3 Aims and Objectives

The aims of this research were to study and develop optical bandgap devices inspired from nature and gain invaluable knowledge about producing novel photonic bandgap structures that can modulate the flow of light and further enhance the development of optical bandgap devices such as optical filters and optical hydrogel sensors for applications in the field of biomedical sciences, food, cosmetics and security industry. The significance of this work is to investigate unique samples from nature and develop novel optical bandgap devices that has not been studied and developed before. The research approach includes investigation, modelling and optical characterisation of novel photonic bandgap devices and demonstrates possible applications in real life.

This research work possesses several challenges such as:

1. Understand theoretical concepts of light interference, diffraction, reflection and transmission, diffraction grating, 2D surface patterning and optical properties of nanostructures and their interaction with light.

2. Search unique samples in nature with potential characteristics of desired optical bandgap devices.

3. Familiarise with FEM modelling technique to carry out accurate simulation of optical bandgap devices. fabrication and optical characterisation.

4. Familiarise with up to date state of the art fabrication methods currently being used for producing optical bandgap devices.

5. Perform optical, scanning electron, transmission electron and atomic force microscopy on fabricated optical bandgap devices.

6. Perform optical characterisation on the fabricated optical nanostructures and devices and propose their possible use in industry with any limitations and future work.

To achieve the aims, objectives were set as following:

1. Study and review on photonic bandgap structures that exist in nature and have been studied.

2. Study on any existing applications based on these photonic bandgap structures.

3. Study on methods of modelling, characterisation and fabrication techniques of these photonic bandgap structures.

4. Find samples in nature that exist and have not been studied before.

5. Perform optical, scanning electron, transmission electron and atomic force microscopy on samples.

6. Study on how to make optical experiment setups and conduct experiments safely.

7. Perform optical characterization of the optical bandgap devices, result analysis, and comparison with the computational modelling results.

8. Finally, propose the possible use of these optical nanostructures in hydrogel based photonic bandgap sensors in industry with any limitations and future work.

1.4 Thesis Outline

This thesis is constructed under the alternative thesis format guidelines provided by the University of Birmingham. This format allows the incorporation of publication style chapters for the research work that has already been published or it is in process of being published.

The first part of the thesis is focused mainly on study of photonic bandgap structures in which two samples from nature were studied in detail. The later part is covering the modelling and fabrication side of photonic bandgap structures in order to gain some experience and study the optical characteristics of these structures under interaction with light. More details are as follows:

Chapter 1 is on introduction to thesis.

Chapter 2 focuses on the study of structural colouration in Nicobar pigeons. Optical microscopy and modelling was conducted to explore the samples. Experiments were carried out to study the surface profile of the feathers. Hydrophobicity experiments were conducted and interaction of the droplet with feather was studied in detail.

Chapter 3 is on the study of structural colouration in Monal pheasants. A different internal structure was explored and studied. Optical microscopy and optical characterisation was conducted on the samples. Transmission Electron Microscopy was performed to further analyse the samples. A study on hydrophobicity of the feathers was carried out which showed change in colour when samples were immersed in liquids with different refractive indices. This change in colour effect evolved different ideas in mind that can only be explored by fabricating and studying the nanostructures; their hydrophobicity and interaction with liquids.

Chapter 4 explains modelling and fabrication of nanostructure using COMSOL Multiphysics and electron beam lithography. To gain more understanding in colour selection mechanism of nanostructures, a simple grating structure was designed and fabricated using two different materials having two different refractive indices namely Silicon and Silicon dioxide. Silicon dioxide acted as a thin film on top of silicon. This Silica grating structure fabricated was a unique structure where thin film and diffraction grating effects occur in combination. The colour selection mechanism of the structure was studied in detail.

Chapter 5 is on understanding and fabrication of nanostructures using laser interference method. Nanostructures were fabricated in varied dimensions on Titanium surfaces. The effect of change in size of structure and change in hydrophobic properties was studied in detail.

Chapter 6 is on contributions, conclusions, limitations and future work.

Bibliography

1. Hooke, R. and R.T. Gunther, *Micrographia, 1665*. 1938: Subscribers.
2. Han, Z., et al., *Active Antifogging Property of Monolayer SiO2 Film with Bioinspired Multiscale Hierarchical Pagoda Structures.* ACS nano, 2016. **10**(9): p. 8591-8602.
3. Regan, E.C., et al., *Substrate-Independent Light Confinement in Bioinspired All-Dielectric Surface Resonators.* Acs Photonics, 2016. **3**(4): p. 532-536.
4. Yang, Q., et al., *Bioinspired fabrication of hierarchically structured, pH-tunable photonic crystals with unique transition.* ACS nano, 2013. **7**(6): p. 4911-4918.
5. Stavenga, D., et al., *Butterfly wing colours: scale beads make white pierid wings brighter.* Proceedings of the Royal Society of London B: Biological Sciences, 2004. **271**(1548): p. 1577-1584.
6. Onslow, H., *The iridescent colours of insects.* Nature, 1920. **106**(2658): p. 181-183.
7. Seago, A.E., et al., *Gold bugs and beyond: a review of iridescence and structural colour mechanisms in beetles (Coleoptera).* Journal of the Royal Society Interface, 2009. **6**(Suppl 2): p. S165-S184.
8. Kinoshita, S., S. Yoshioka, and J. Miyazaki, *Physics of structural colors.* Reports on Progress in Physics, 2008. **71**(7): p. 076401.
9. Vukusic, P., R. Wootton, and J. Sambles, *Remarkable iridescence in the hindwings of the damselfly Neurobasis chinensis chinensis (Linnaeus)(Zygoptera: Calopterygidae).* Proceedings of the Royal Society of London B: Biological Sciences, 2004. **271**(1539): p. 595-601.
10. Butt, H., et al., *Morpho Butterfly-Inspired Nanostructures.* Advanced Optical Materials, 2016. **4**(4): p. 489.

11. Sharma, V., et al., *Structural origin of circularly polarized iridescence in jeweled beetles.* science, 2009. **325**(5939): p. 449-451.
12. Vukusic, P. and D. Stavenga, *Physical methods for investigating structural colours in biological systems.* Journal of the Royal Society Interface, 2009. **6**(Suppl 2): p. S133-S148.
13. Lythgoe, J. and J. SHAND, *The structural basis for iridescent colour changes in dermal and corneal irddophores in fish.* Journal of Experimental Biology, 1989. **141**(1): p. 313-325.
14. Brink, D.J., N.G. van der Berg, and A.J. Botha, *Iridescent colors on seashells: an optical and structural investigation of Helcion pruinosus.* Applied Optics, 2002. **41**(4): p. 717-722.
15. Parker, A.R., *The diversity and implications of animal structural colours.* Journal of Experimental Biology, 1998. **201**(16): p. 2343-2347.
16. Amiri, M. and H.M. Shaheen, *Chromatophores and color revelation in the blue variant of the Siamese fighting fish (Betta splendens).* Micron, 2012. **43**(2): p. 159-169.
17. Chandler, C.J., et al., *Structural colour in Chondrus crispus.* Scientific reports, 2015. **5**.
18. Levy-Lior, A., et al., *Guanine-Based Biogenic Photonic-Crystal Arrays in Fish and Spiders.* Advanced Functional Materials, 2010. **20**(2): p. 320-329.
19. Bai, L., et al., *Bio-inspired vapor-responsive colloidal photonic crystal patterns by inkjet printing.* ACS nano, 2014. **8**(11): p. 11094-11100.
20. Merindol, R., et al., *Bio-inspired multiproperty materials: Strong, self-healing, and transparent artificial wood nanostructures.* ACS nano, 2015. **9**(2): p. 1127-1136.
21. Glover, B.J. and H.M. Whitney, *Structural colour and iridescence in plants: the poorly studied relations of pigment colour.* Annals of botany, 2010. **105**(4): p. 505-511.
22. Hébant, C. and D.W. Lee, *Ultrastructural basis and developmental control of blue iridescence in Selaginella leaves.* American Journal of Botany, 1984. **71**(2): p. 216-219.
23. Vignolini, S., et al., *Pointillist structural color in Pollia fruit.* Proceedings of the National Academy of Sciences, 2012. **109**(39): p. 15712-15715.
24. Vignolini, S., B. Glover, and U. Steiner, *Photonic Structures in Plants*, in *Biomimetics in Photonics*. 2012, Taylor & Francis. p. 1-18.
25. Braun, P.V., *Materials science: Colour without colourants.* Nature, 2011. **472**(7344): p. 423-424.

26. Stavenga, D.G., et al., *Dramatic colour changes in a bird of paradise caused by uniquely structured breast feather barbules.* Proceedings of the Royal Society of London B: Biological Sciences, 2010: p. rspb20102293.
27. Remsen Jr, J., *HBW and BirdLife International Illustrated Checklist of the Birds of the World Volume 1: Non-passerines Josep del Hoyo and Nigel J. Collar 2014. Lynx Edicions, Barcelona. 903 pages, hundreds of color plates. ISBN 9788496553941. $209 (Hardcover).* Journal of Field Ornithology, 2015. **86**(2): p. 182-187.
28. Stavenga, D.G., *Thin film and multilayer optics cause structural colors of many insects and birds.* Materials Today: Proceedings, 2014. **1**: p. 109-121.
29. Liu, Y., X. Chen, and J. Xin, *Hydrophobic duck feathers and their simulation on textile substrates for water repellent treatment.* Bioinspiration & biomimetics, 2008. **3**(4): p. 046007.
30. Eliason, C.M. and M.D. Shawkey, *A photonic heterostructure produces diverse iridescent colours in duck wing patches.* Journal of the Royal Society Interface, 2012. **9**(74): p. 2279-2289.
31. Steadman, D., *The historic biogeography and community ecology of Polynesian pigeons and doves.* Journal of Biogeography, 1997. **24**(6): p. 737-753.
32. Leclaire, S., et al., *Feather bacterial load affects plumage condition, iridescent color, and investment in preening in pigeons.* Behavioral Ecology, 2014. **25**(5): p. 1192 - 1198.
33. Yin, H., et al., *Iridescence in the neck feathers of domestic pigeons.* Physical Review E, 2006. **74**(5): p. 051916.
34. Sun, J., B. Bhushan, and J. Tong, *Structural coloration in nature.* Rsc Advances, 2013. **3**(35): p. 14862-14889.
35. Doucet, S.M., et al., *Iridescent plumage in satin bowerbirds: structure, mechanisms and nanostructural predictors of individual variation in colour.* Journal of Experimental Biology, 2006. **209**(2): p. 380-390.
36. Yoshioka, S. and S. Kinoshita, *Effect of macroscopic structure in iridescent color of the peacock feathers.* Forma-tokyo-, 2002. **17**(2): p. 169-181.
37. Greenewalt, C.H., W. Brandt, and D.D. Friel, *Iridescent colors of hummingbird feathers.* JOSA, 1960. **50**(10): p. 1005-1013.
38. Liu, K. and L. Jiang, *Multifunctional integration: from biological to bio-inspired materials.* ACS nano, 2011. **5**(9): p. 6786-6790.
39. Xiao, M., et al., *Bio-inspired structural colors produced via self-assembly of synthetic melanin nanoparticles.* ACS nano, 2015. **9**(5): p. 5454-5460.

40. Liu, K. and L. Jiang, *Bio-inspired design of multiscale structures for function integration.* Nano Today, 2011. **6**(2): p. 155-175.
41. Wang, X., et al., *Engineering biomimetic superhydrophobic surfaces of electrospun nanomaterials.* Nano Today, 2011. **6**(5): p. 510-530.
42. Zhang, X., et al., *Bioinspired Multifunctional Foam with Self-Cleaning and Oil/Water Separation.* Advanced Functional Materials, 2013. **23**(22): p. 2881-2886.
43. Zhang, S. and Y. Chen, *Nanofabrication and coloration study of artificial Morpho butterfly wings with aligned lamellae layers.* Scientific reports, 2015. **5**.
44. Meylan, L. and S. Susstrunk. *Bio-inspired color image enhancement*. in *Electronic Imaging 2004*. 2004: International Society for Optics and Photonics.
45. Huang, J., X. Wang, and Z.L. Wang, *Bio-inspired fabrication of antireflection nanostructures by replicating fly eyes.* Nanotechnology, 2007. **19**(2): p. 025602.
46. Tsangarides, C.P., et al., *Computational modelling and characterisation of nanoparticle-based tuneable photonic crystal sensors.* Rsc Advances, 2014. **4**(21): p. 10454-10461.
47. Yang, X., et al., *Bioinspired effective prevention of restacking in multilayered graphene films: towards the next generation of high-performance supercapacitors.* Advanced Materials, 2011. **23**(25): p. 2833-2838.
48. Yetisen, A.K., et al., *Nanotechnology in textiles.* ACS nano, 2016. **10**(3): p. 3042-3068.
49. Li, X., et al., *Nanoscale structural and mechanical characterization of a natural nanocomposite material: the shell of red abalone.* Nano Letters, 2004. **4**(4): p. 613-617.
50. Yetisen, A.K., et al., *Art on the Nanoscale and Beyond.* Advanced Materials, 2015. **28**(9): p. 1724 - 1742.
51. Kabilan, S., et al., *Holographic glucose sensors.* Biosensors and Bioelectronics, 2005. **20**(8): p. 1602-1610.
52. Kabilan, S., et al., *Glucose-sensitive holographic sensors.* Journal of Molecular Recognition, 2004. **17**(3): p. 162-166.
53. Xue, F., et al., *A 2-D photonic crystal hydrogel for selective sensing of glucose.* Journal of Materials Chemistry A, 2014. **2**(25): p. 9559-9565.
54. Chen, C., et al., *2D Photonic Crystal Hydrogel Sensor for Tear Glucose Monitoring.* ACS Omega, 2018. **3**(3): p. 3211-3217.
55. Zhao, Y., et al., *Smart hydrogel-based optical fiber SPR sensor for pH measurements.* Sensors and Actuators B: Chemical, 2018. **261**: p. 226-232.

56. Yuan, H., et al., *Fiber-optic surface plasmon resonance glucose sensor enhanced with phenylboronic acid modified Au nanoparticles.* Biosensors and Bioelectronics, 2018. **117**: p. 637-643.
57. Gupta, V.K., et al., *A novel glucose biosensor platform based on Ag@AuNPs modified graphene oxide nanocomposite and SERS application.* Journal of Colloid and Interface Science, 2013. **406**: p. 231-237.
58. Moschou, E.A., et al., *Fluorescence Glucose Detection: Advances Toward the Ideal In Vivo Biosensor.* Journal of Fluorescence, 2004. **14**(5): p. 535-547.
59. Badugu, R., J.R. Lakowicz, and C.D. Geddes, *Noninvasive Continuous Monitoring of Physiological Glucose Using a Monosaccharide-Sensing Contact Lens.* Analytical Chemistry, 2004. **76**(3): p. 610-618.
60. Alexeev, V.L., et al., *High Ionic Strength Glucose-Sensing Photonic Crystal.* Analytical Chemistry, 2003. **75**(10): p. 2316-2323.
61. Asher, S.A., et al., *Photonic Crystal Carbohydrate Sensors: Low Ionic Strength Sugar Sensing.* Journal of the American Chemical Society, 2003. **125**(11): p. 3322-3329.
62. Huang, J., et al., *pH and ionic strength responsive photonic polymers fabricated by using colloidal crystal templating.* Colloid and Polymer Science, 2008. **286**(1): p. 113-118.
63. Lee, Y.-J., S.A. Pruzinsky, and P.V. Braun, *Glucose-Sensitive Inverse Opal Hydrogels: Analysis of Optical Diffraction Response.* Langmuir, 2004. **20**(8): p. 3096-3106.

Chapter 2: Study on Structural Colouration in *Caloenas Nicobarica* pigeons

The research work in this chapter is also published in Advanced Optical Materials. I am the main (first) author of this published paper. Further details and co-authors contributions are as following:

Ijaz Rashid, Muhammad Umair Hassan, Abbas Khandwalla, Rayan Mohammed Ameen, Ali Kemal Yetisen, Qing Dai, Haider Butt. (2018). *"Structural Coloration in Caloenas Nicobarica Pigeons and Refractive Index Modulated Sensing."* Advanced Optical Materials 6(9): 1701218.

Ijaz Rashid: is the main (first) author and he observed the angle dependent colour change in the feathers. He modelled the experimental setups and conducted the experiments. He designed optical characterization setups and optical spectra setups. He has written the manuscript that was reviewed by Dr Muhammad Umair Hassan, Dr Qing Dai, Dr Ali Kemal Yetisen and lead supervisor Dr Haider Butt (*).

Abbas Khandwalla: contributed towards collecting data for optical spectra during rotation stage experiments.

Rayan M. Ameen: contributed towards the SEM imaging.

Chapter 2: Study on Structural Colouration in *Caloenas Nicobarica* pigeons

2.1 Introduction

Nicobar pigeon (*Caloenas Nicobarica*), is an iridescent near-threatened bird species in the family of pigeons or doves [1]. Nicobar pigeons inhabit the Nicobar islands of Malay Archipelago, Solomons, Palu and south-eastern coastal regions of India, and its population has been decreasing due to lowland deforestations [2]. The bird's feathers exhibit all colours (blue, green, red) across the visible spectrum as shown in **Figure 2.1** below.

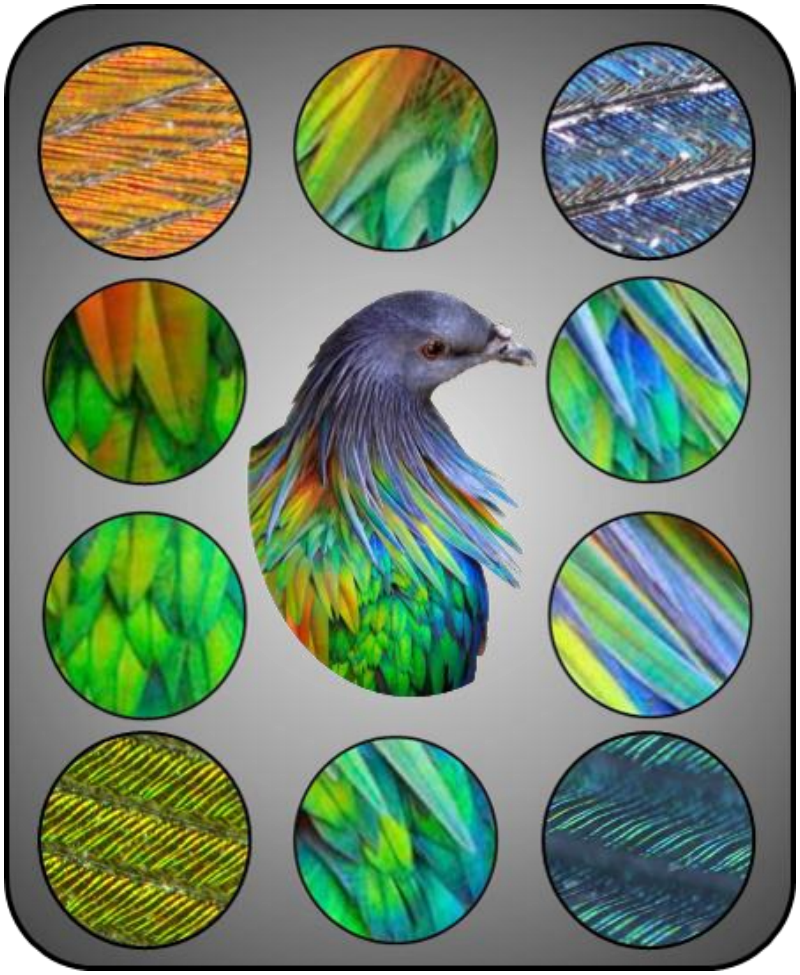

Figure 2.1. Nicobar pigeon

Surprisingly, colour mechanism / photonic effects of the Nicobar pigeon have not been reported. In this work, optical microscopy and spectroscopy techniques were used to study the structural colouration in Nicobar pigeon feathers. With an incident broadband light, the bird's barbule diffracted highly-intense colours (red, green, blue), which undergo a systematic shift at an angle of ~45°. Feathers showed low transmittance and hardly allowed light to pass though indicating high absorption across a wide range of the incident wavelengths. The consideration that low transmittance across the entire visible range can be due to the high reflectance from the feather top surface was ruled out, as reflectance occurs only for selective wavelengths recorded in reflection experiments as detailed in the following discussion. Laser-induced far-field diffraction was used to reconstruct the microscopic landscape and arrangement of barbules in the vane of the feather. Super-hydrophobicity nature of Nicobar feathers showed a large contact angle of ~ 156°, comparable to those of the duck family [3]. In this recent work, an advanced electrochemical and optical technique for quantitative sensing [4-7] is reported. Interfacial and geometric properties of the naturally structured feathers were exploited for refractive index modulated sensing.

2.2 Methods

2.2.1 Optical Microscopy

Red, blue and green feathers for the male Himalayan Monal were located and obtained from Etsy (Brooklyn, New York City, New York, United States). The feather samples were placed on glass slides and kept in a container when not in use, to protect them from dust and other contaminants. Optical microscopy (Axio Scope Model A1 Zeiss, 5-100 ×) was carried out (as shown in **Figure 2.2a**) mainly on two kinds of feathers, both of which show predominantly two alternating colours: a red-green (RG) and a green-blue (GB) when viewed at different angles. Calami of feathers were placed on glass slides to bring reasonable numbers of barbs

(thereby barbules) in the horizontal plane in order to enhance their simultaneous visibility under the microscope. Dark and bright field microscopy were used to visualize both feathers. Images were captured using a digital camera mounted on top of the microscope and connected to the computer. ZEN imaging software was used to capture the images. The sample was rotated 360° horizontally using the rotation stage setup shown in **Figure 2.2b**.

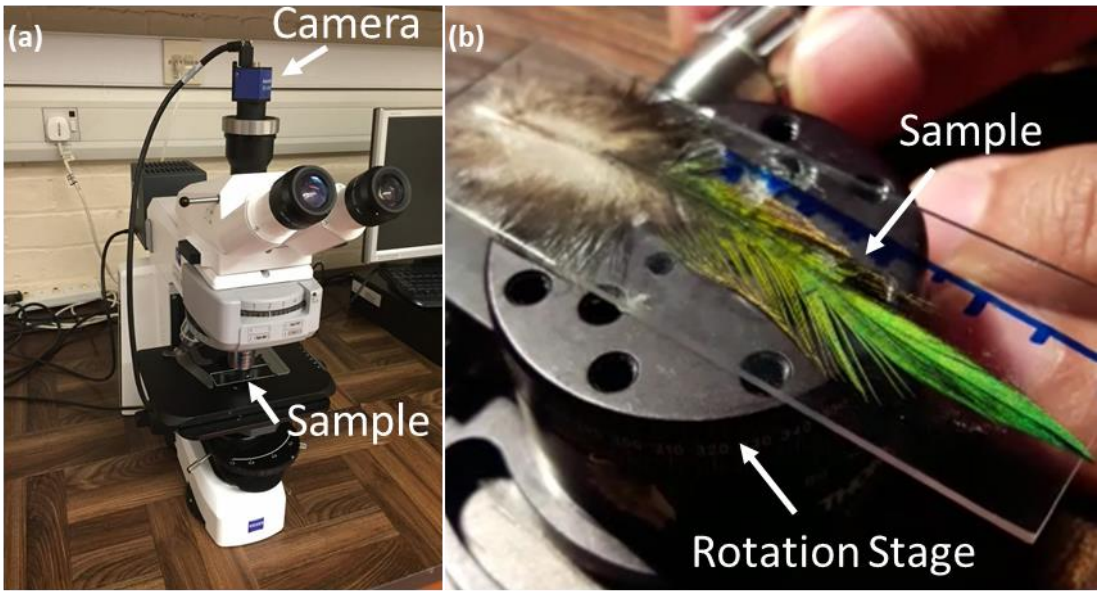

Figure 2.2. Optical Microscopy **(a)** Microscopy setup showing sample and camera **(b)** Rotation stage setup with a sample red-green feather placed on top.

2.2.2 Spectroscopy

Spectroscopic measurements were performed on feathers as shown in **Figure 2.3a-d**. Reflection at different angles was received and characterized using Ocean Optics (DH-2000) spectrometer in standard and in-house developed setups. Feather was mounted on a rotation stage with two optic fibres. One transmitting the broadband light whereas the other receiving the reflected light from the surface.

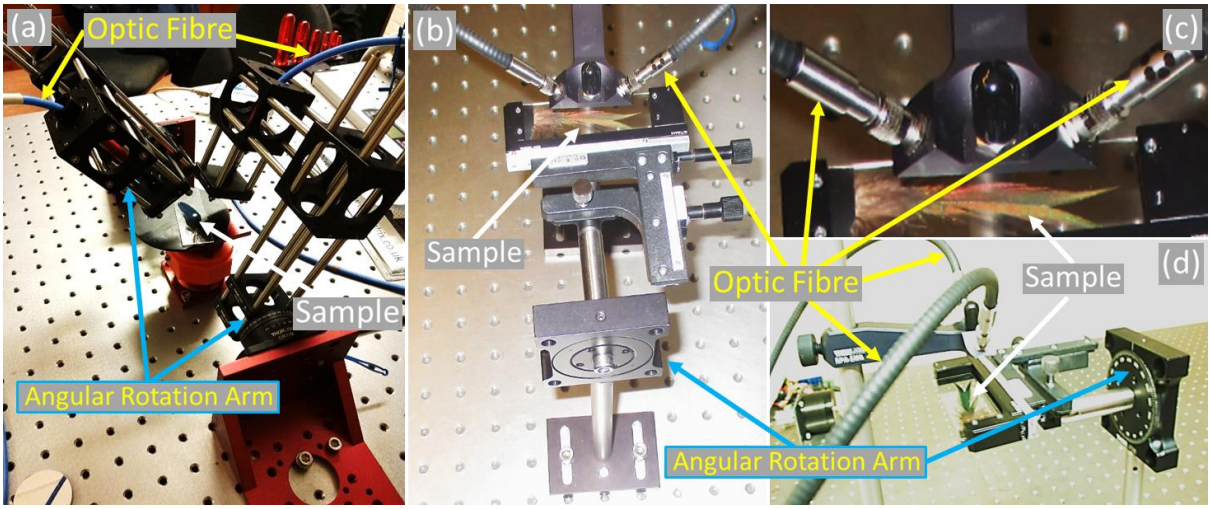

Figure 2.3. (a) Spectroscopy setup with rotating arms and a sample mounted on the stage **(b-d)** Top and side view of zero and 45-degree reflection measurement setup with a special compact cable and sample feather placed underneath.

A compact black cable with seven optic fibres joined together inside was used to measure reflection at 0° and 45°. It consisted of six optic fibres joined in hexagon shape and seventh optic fibre in the middle. The middle fibre was used to transmit light whereas the six around it were receiving the reflected light. The optic fibre was mounted on top for zero-degree reflection measurement. Blue optic fibres were used in combination with the black optic fibre cable for 45° measurements as shown in **Figure 2.3a**.

2.2.3 SEM imaging

SEM was used to visualize the surface of the feathers from different locations. Feathers were cleaned with ethanol and dehydrated. They were coated with Au (thickness ~ 20 nm) and cured to prevent any charging effect during electron microscopy. The samples were mounted on copper grid in CFEI Quanta 3D FEG FIB-SEM system for scanning electron microscopy.

2.2.4 Hydrophobicity

The sessile droplet method was used to measure the contact angle of the liquid on the feather's surface. A drop of size 2 µl was placed on the feather surface using a micropipette

(SP0020-Auto, SciQuip). The feather was rotated and images were captured using a digital camera. **Figure 2.4** shows the illumination lamp, drop placed on sample mounted on a stage and a digital camera capturing the images. Image J (Wayne rasband, USA) was used for analysis and measurements. The shape of droplet with size less than 3 µl is approximately a complete sphere. Contact angle can be simply measured using a tangent line at the curve with surface in contact acting as baseline. Image J uses both sphere and ellipse approximations for more accurate contact angle measurements using the shape of drop captured in the image. It also uses Laplace equation in case of larger drop size (over 5 µl) where gravity effect cannot be ignored in order to determine more accurate contact angle measurement.

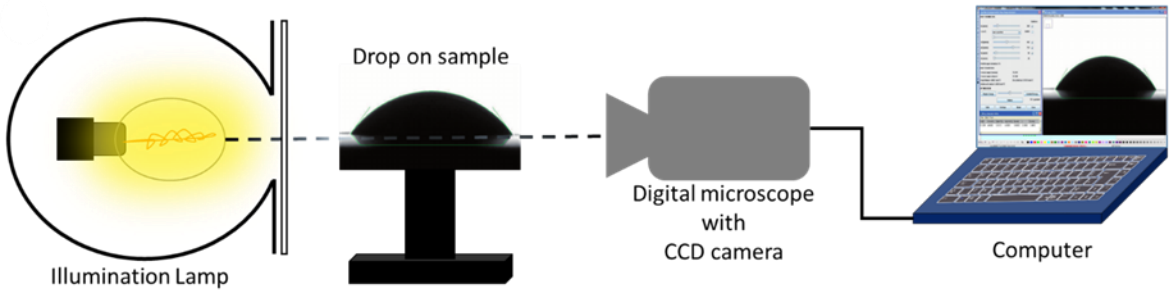

Figure 2.4. Schematic diagram of contact angle measurement setup.

2.2.5 Sensing shift in spectrum wavelength

The sample was first placed under the optical microscope (Axio Scope.A1, ZEISS) and the relevant area was brought into focus. A digital camera was mounted on top of the microscope and connected to the computer. Images were captured using ZEN imaging software. A droplet of size 2 µl was then dropped using the micropipette on the same spot under focus. The barbules surface absorbed the liquid droplet. Images were recorded in wet conditions. High and low concentrations of glucose solutions (0 mM to 200 mM) were used and images were captured in each case. This variation in glucose concentrations was chosen to be able to detect the refractive index modulated changes. Reflection spectra were also recorded in the same manner to observe the peak shifts in wavelength to sense refractive index modulation. An optic fibre was

connected to the microscope in place of digital camera in order to receive the reflection spectrum. Ocean View software and spectrophotometer (USB2000+, Ocean Optics, Oxford) were used to receive and view the optical spectra. The results were then plotted together to observe the peak shifts in wavelengths.

2.3 Results and Discussion

Optical microscopy (Zeiss, 5-100 ×) was carried out mainly on two kinds of feathers, both of which show predominantly two alternating colours: a red-green (RG) and a green-blue (GB) when viewed at different angles. Calami of feathers were placed on glass slides to bring reasonable numbers of barbs (thereby barbules shown in **Figure 2.5c, d**) in the horizontal plane in order to enhance their simultaneous visibility under the microscope. Dark and bright field microscopy were used to visualize both feathers. The difference between both microscopic schemes enabled imaging the feather from the same eyepiece location while they were subject to normal and oblique illumination angles, respectively. **Figure 2.5a, b** shows the microscopy schemes, bright field and dark field, used to investigate the optical effects in the Nicobar pigeon's feathers. Switching from one scheme to another illuminates the feather at a different angle (BF 0° to DF 45° approx.) that results in change in their colour, **Figure 2.5c, d.**

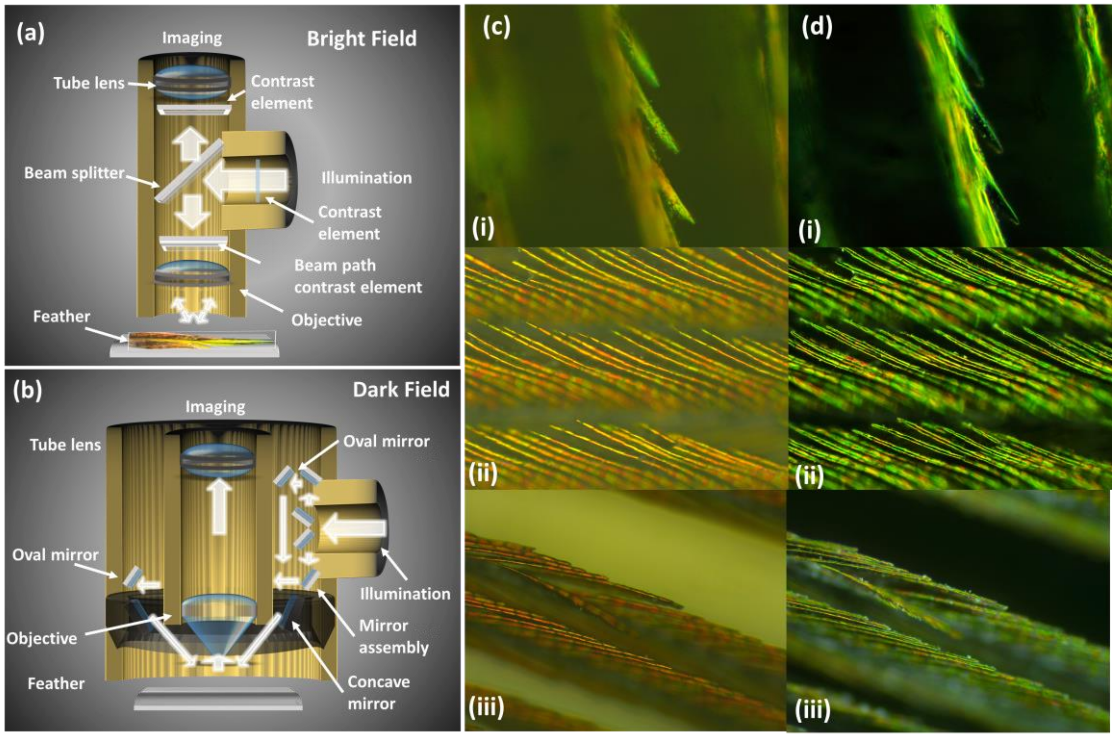

Figure 2.5. Dark and bright field schematics and microscopy images of barbules **(a, b)** Schematics **(c, d)** Bright and dark field microscopic images of a red-green feather.

The bird's feathers exhibit all colours (blue, green, red) across the visible spectrum (**Figure 2.6a**). The vane of the RG (GB) feather exhibited a blue shift from red to green and green to blue when viewing mode was shifted from the bright field to the dark field (**Figure 2.6b, c**). The downy barbs are dark grey whereas after feathers are dark and light brown in colour but both do not exhibit any structural colouration or photonic effect. The downy barbs and after feathers were random and no particular arrangement/order was perceived at these locations for both types of feather. The bottom side of both feathers was also dark and exhibited no colour or change in colour when viewed through either in BF or DF modes (**Figure 2.6f, g**). In the transmission mode, light was highly absorbed by the feather and yielded no patterns or optical effects across the whole length and breadth of the feather. Photographs of whole RG and GB feathers are shown from the top and GB feather from the bottom in **Figure 2.6f**, **g** and **h**, respectively.

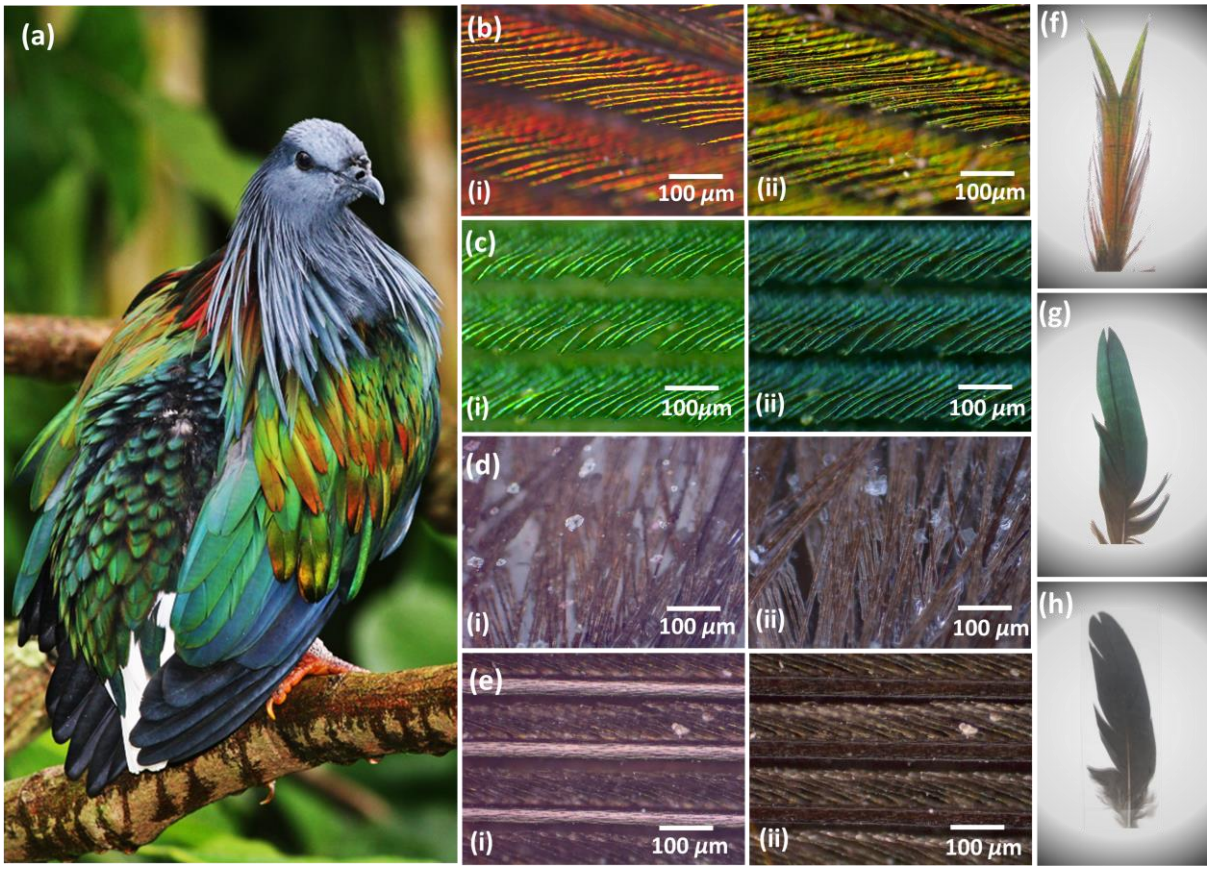

Figure 2.6. Nicobar pigeon, its feathers and microscopic images. **(a)**The Nicobar pigeon. **(b)** The bright and dark-field microscopy images of a red-green (RG) feather reflecting the colour change from (i) red to (ii) green, respectively. **(c)** The DF and BF microscopy images of a green-blue (GB) feather reflecting the colour change from (i) green to(ii) blue, respectively. **(d,e)** DF and BF microscopy images were taken at different locations from the bottom of a GB feather showing no optical effects. No optical effects were observed in all kinds of feathers when viewed from the bottom. **(f, g)** Photographic images taken from the top of an RG and GB feather. **(h)** Photographic images taken from the bottom of a GB feather. All feathers appeared dark grey when viewed from the bottom.

2.3.1 Optical Characterisation

Far-field diffraction characterization of the feathers was carried out in the transmission mode. Red (630 nm), green (532 nm) and blue (420 nm) laser beams were utilized to illuminate from the normal to the barbules' plane, and an image screen was used to record the diffraction

patterns as shown in **Figure 2.7a** schematics diagram. These experiments revealed the placement of adjacent barbules in the vane. The transmitted diffraction intensity had the highest value for the green laser, whereas the red and blue lasers showed comparatively weaker transmissions for all diffraction orders. **Figure 2.7b-d** illustrates intensity versus interspace curves (traversing along two main interference patterns) obtained on the projection screen curves. Snapshots of the diffraction pattern cast on the image screen (right) and diffraction contour (insets) provided a topographic illustration where transmitted intensities of different diffraction orders could be visualized in terms of the brightness of the hue as conceived from the screen (right snapshot) and height of the diffraction profile (inset), respectively. The revealed microscopic landscape, which is the placement of the barbules in the vane, was retraced by taking the inverse Fourier transform (FT) of the diffraction pattern **(Figure 2.7e)**. When viewed through a scanning electron microscope (SEM) **(Figure 2.7f)**, the bottom side of the feather provides the same structure as obtained from the inverse Fourier transform of the diffraction pattern. Further confirmation is presented by the computationally obtained FT using Image J that also results in the identical pattern to that obtained in the diffraction experiment in transmission mode **(Figure 2.7g)**. The transmitted diffraction obtained from such feathers can provide the microscale placement details of the barbules and the surface structure profile. However, internal structure of the feather, which comprises of the multilayer keratin and melanosome rods, was not realized due to strong absorption behaviour of the feather in the transmission mode. SEM imaging was performed with the help of Rayan Ameen who was a third year student in the Metallurgy and Material Science Department at the University of Birmingham. His experience in imaging lead us to quick identifying of the structures and capture images. The surface structure observed is shown in **Figure 2.7f.**

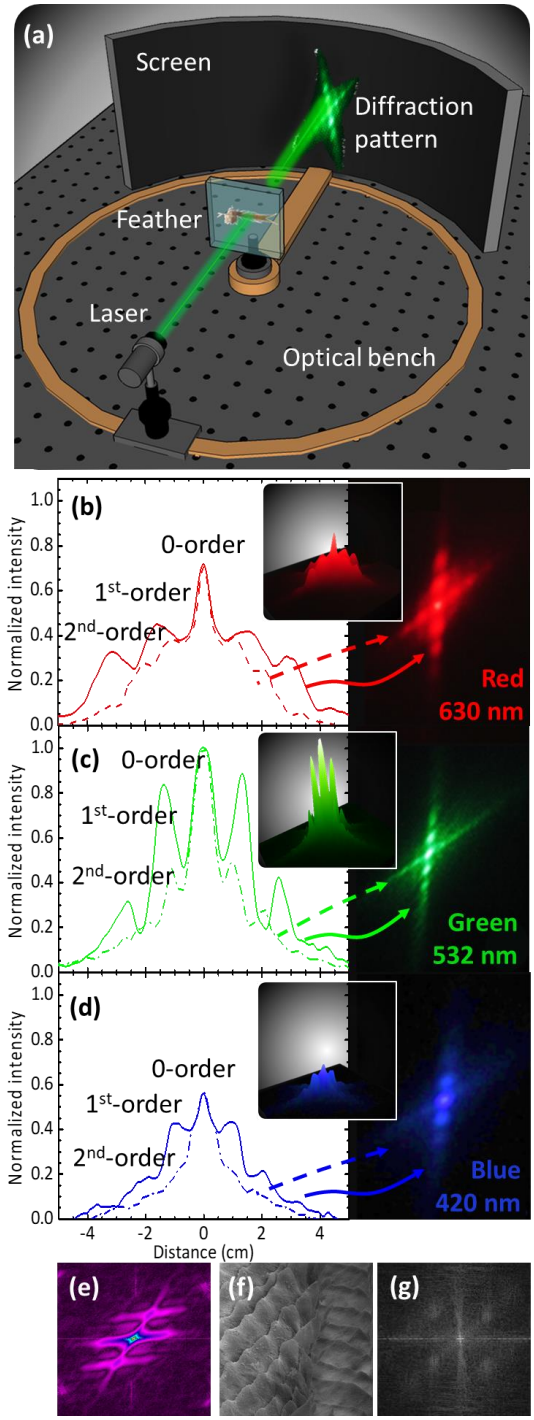

Figure 2.7. Optical characterization of diffraction from the feather barbule. **(a)** Schematic for the diffraction of monochromatic light in transmission mode. **(b-d)** The diffraction orders plotted as normalized intensity as a function of distance curves. The longer the wavelength, the wider the interspace between the subsequent orders. Highest diffraction efficiency was obtained from the green laser. The right panels illustrate the photographs of the diffraction patterns using

monochromatic light. 3D topographic reconstruction of diffraction patterns is shown in the insets. **(e)** The inverse Fourier transform of the diffraction pattern (green beam) revealed the feather's structure. **(f)** The scanning electron image of the back side of the feather. This part of the image was selected to perform the Fourier transform. **(g)** Computed Fourier transform of the image **f**, which resembles the experimentally observed diffraction pattern.

Optical diffraction from different points at RG and GR feathers were observed at normal to the feather surface plane with illumination at 0° and 45° angles. A broadband light source was used for the illumination and feathers were moved horizontally by means of a translational stage. Spectra were recorded with 5 mm increments (**Figure 2.8**). The spectra for RG (GB) feather blue-shifted, from longer wavelengths of red (or green) to shorter wavelengths of green (or blue), as the angle of measurement, increased from 0° to 45°. In both feathers, moving from the point closer to the tip (5 mm) toward the hollow shaft (25 mm) shifted the diffracted light to shorter wavelengths. To perceive the colour, all recorded diffraction curves were plotted according to colour illumination effect (CIE) standards of International Commission on Illumination. The perceived colours and their shift with translation on the RG and GB feathers are highlighted in **Figure 2.8c, d**, respectively.

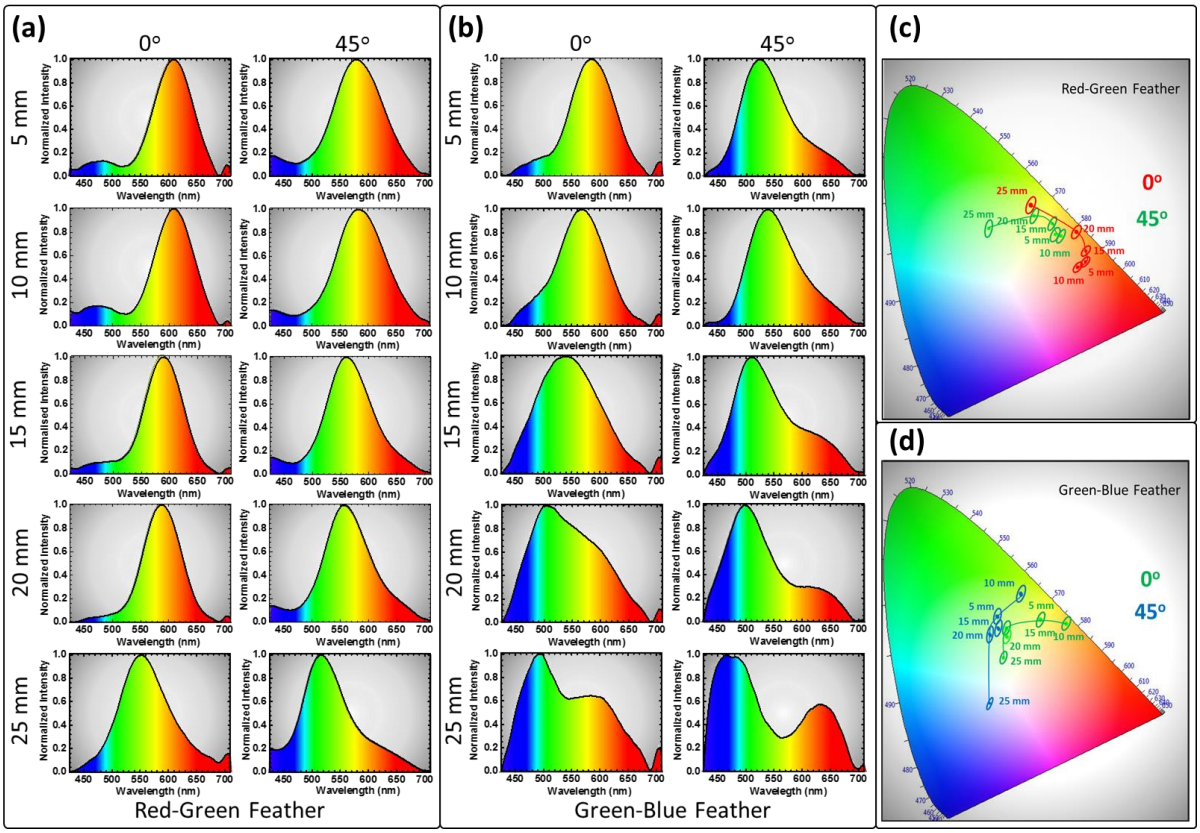

Figure 2.8. Optical spectra of feathers **(a)** RG and **(b)** GB feathers at different locations, while feathers are illuminated at 0° and 45°, respectively. **(c, d)** The illumination angle at 0° and 45° shifted the spectra from red to green and green to blue for RG and GB feather, respectively. CIE images indicating the visible shift of colours upon switching the incidence angle from 0° to 45° at different equidistant locations on RG and GB feathers, respectively.

A change in the viewing elevation angle shifted the overall peak while the broadband light was incident from the normal, whereas, rotation of feathers along vertical-axis (azimuthal angle) showed only the change in overall intensity of particular colour as viewed from certain elevation and, in general, did not shift the colours. In a rotation setup to characterize the feathers, the broadband light was illuminated from the normal (top) and optical spectra were recorded between normal to 45° with an increment of 5°, while feather was rotated between 0° to 90° on a stage (**Figure 2.9a**). Measurements in **Figure 2.9b, c** were taken from the mid-section for both feathers, where the colour was the most brilliant. The spot size of the broadband light was

~ 2 mm. For RG (GB) feather, elevation-dependent recording of colours showed a shift from 600 nm (yellow) to 550 nm (green), while viewing angle was moved from normal 0° to oblique 45°. For the z-axis rotation (azimuthal angle), measurements were carried out at 0° and 45° elevation angles. The azimuthal angle variation was resulted solely in intensity changes between a maximum of ~ 600 nm (550 nm) and a minimum 550 nm (500 nm) for RG (GB) feathers and showed no shift in the peak values of the wavelength (**Figure 2.9**). Therefore, one of the repercussions of the change in the azimuth was that both feathers appeared dark at certain angles and bright at others – no detectable diffraction was observed at certain illumination and viewing settings.

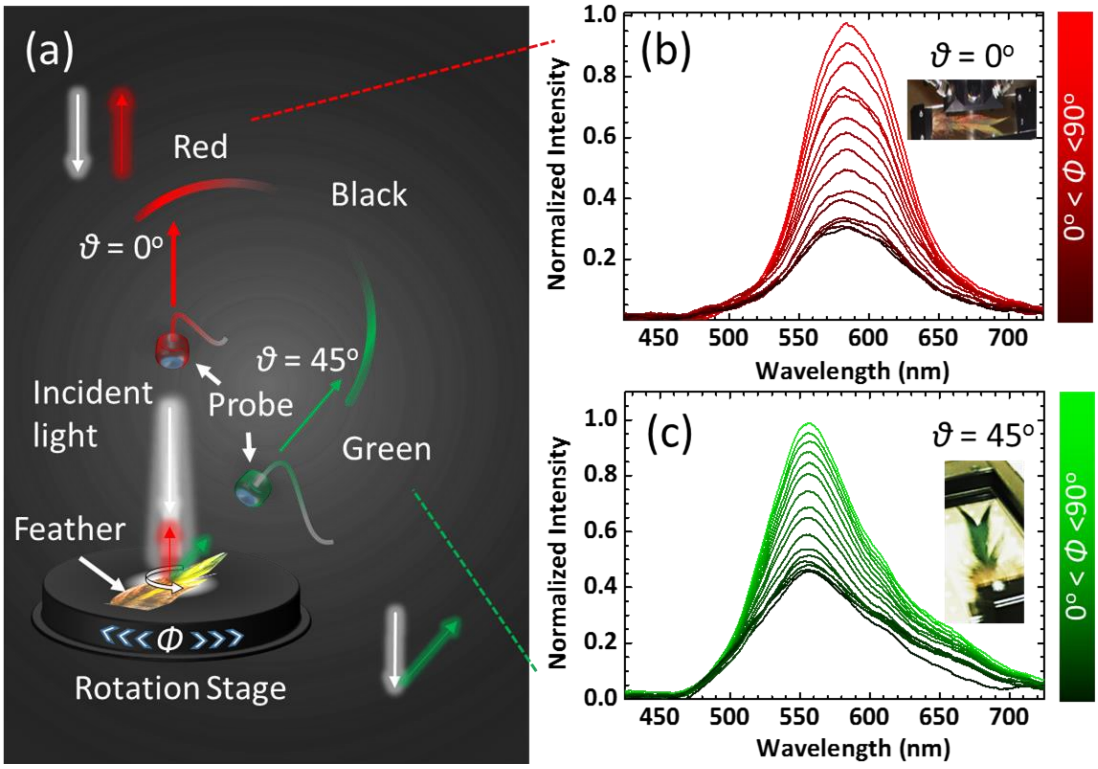

Figure 2.9. Optical characterization of the feathers. **(a)** Schematic diagram of rotation stage setup. (**b, c)** Variation in optical intensities at $\theta = 0°$ and 45°, while Φ was rotated through 0° to 90°.

Observers viewing from different locations perceive colours of Nicobar pigeon differently. Two interchangeable broadband light sources were used to illuminate the samples at 0° and 45°

with respect to the normal defining the illumination plane (**Figure 2.10**). A diffused tungsten light source illuminated the whole feather and, a fiber optic source illuminated the feathers from a small ~ 1 cm circular spot. Photographs were then taken at 0° and 45° in the recording plane. At 0° (45°) of recording for the RG feather, the spot exhibited predominant red (to green) colour, whereas surrounding part of the feather irradiated green (and red) colour. Similarly, 0° (45°) of recording for the GB feather, the spot showed green (to blue) colour, whereas surrounding part reflected blue (to green) colour. Hence, both the illumination angle and different viewing positions define the perceived colour.

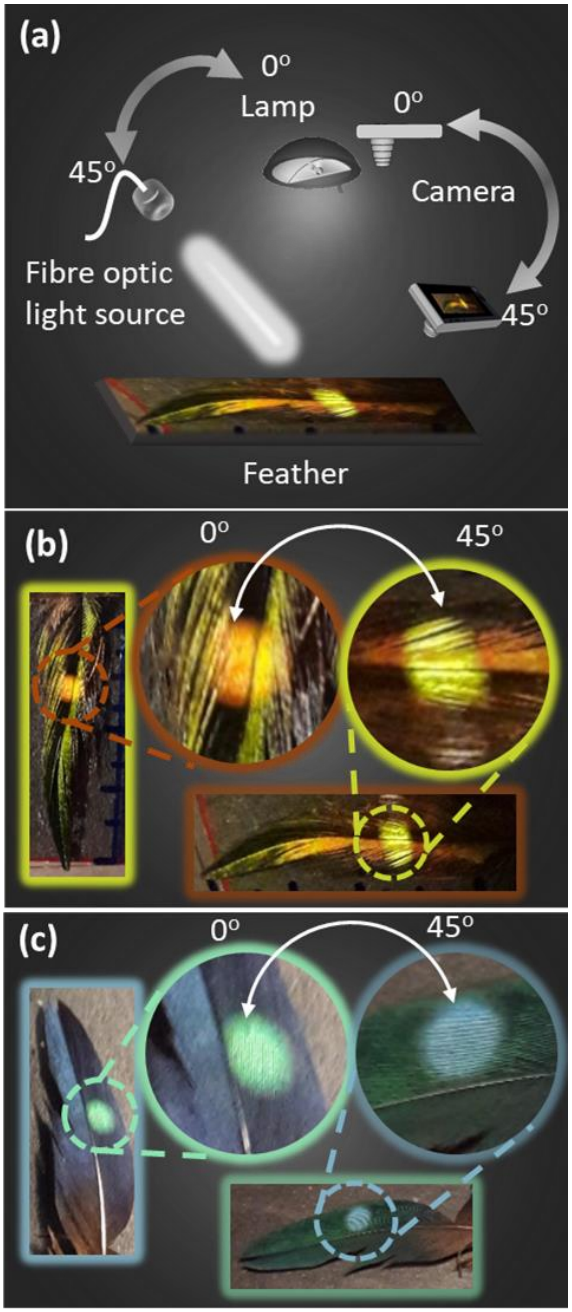

Figure 2.10. Angle-dependent characterization of the feathers. **(a)** Schematic of two-source illumination of the feathers using two interchangeable light sources: a diffused incandescent tungsten lamp and a collimated broadband light to observe two colours at same viewing angle simultaneously. **(b, c)** Photographs of RG and GB feathers taken from two different angles.

There is a distinction between our selected RG and GB feathers in terms of their mechanical and optical properties. The RG feather is a neck (capital) feather which is softer than the BG wing (humeral) feather – a generic feature of all birds. **Figure 2.11a-l** provides magnified

microscopic images of the Nicobar pigeon feathers. Beside optical response to the broadband light, melanosomes might also play a part in colouration. Investigation of the RG feather revealed rich colouration, especially close to the main shaft, and other locations in the vane. Each barbule consisted of several segments that showed a spectacular range of colours in the visible spectrum. Basic colours including red, green and blue were observed. These colours can be observed in one barbule alone, where red, green and blue can be seen in adjacent segments. However, the change in hue within these segments are not merely the pigments that are strictly localized in well-defined segments in the barbule but are coupled with photonic effects at different tilt angles, which are responsible for the vivid show of the range of colours at certain angles **(Figure 2.10)**. The variation in relative structural orientation in adjacent segments of single barbule results in colour change. The selected BG wing feather was hard and almost all barbules along the vane showed identical optical behaviour. When viewed under the microscope, the straight horizontal part of barbules provided a light-blue colour and became green along the curved part, the curve angle being almost 45°. Under high magnification the colour of the barbule on either side of the main shaft was different, the upper being green and the lower being blue, showing the difference in the effective viewing angles **(Figure 2.11i, l)**. The difference in colours was due to curves (change in angle) present in barbules.

The most dominant colouration mechanism in bird feathers is due to multilayer films [8-11]. Similarly, the pigeon and dove family of birds have multilayer structures in their barbules [12-14]. We suggest that barbules of Nicobar pigeon possess a multilayer photonic bandgap structure, in which transparent keratin film encapsulates air-filled multilayered melanosome cavities – the tilt in the illumination or/and observation angle result in the change in the brightness and shift in colours. In the investigation of the Nicobar pigeon feathers, the peaks of the spectra shifted to shorter wavelengths with an increase in the angle of incidence. Additionally, at larger angles of incidence, the diffraction amplitude decreased considerably –

complete blackening below the spectrometer sensitivity was observed at certain angles. The differences in refractive indices of the structured layers and their spatial periodicity, as well as the relative thickness of barbules, play a key role in determining which wavelengths are coherently backscattered. One of the main characteristics of structural iridescent feathers is that the colour varies depending on the angle between illumination and observation as well as between the feather orientation and the plane of examination. The change in the thickness of layers and thereby characteristic of photonic bandgap structures within the layers dictate the incident light to travel shorter or longer distances through the layers with increasing or decreasing angle with the barbule plane, respectively. The backscattered coherent light changes its colour according to the direction of the reflection (**Figure 2.11m**). These observations are consistent with the barb behaving as a set of multilayer Bragg mirrors. See **Figure 2.7** for transmission experiments in the far-field setup carried out to observe the light transmission and diffraction behaviour of the feathers in the transmission mode.

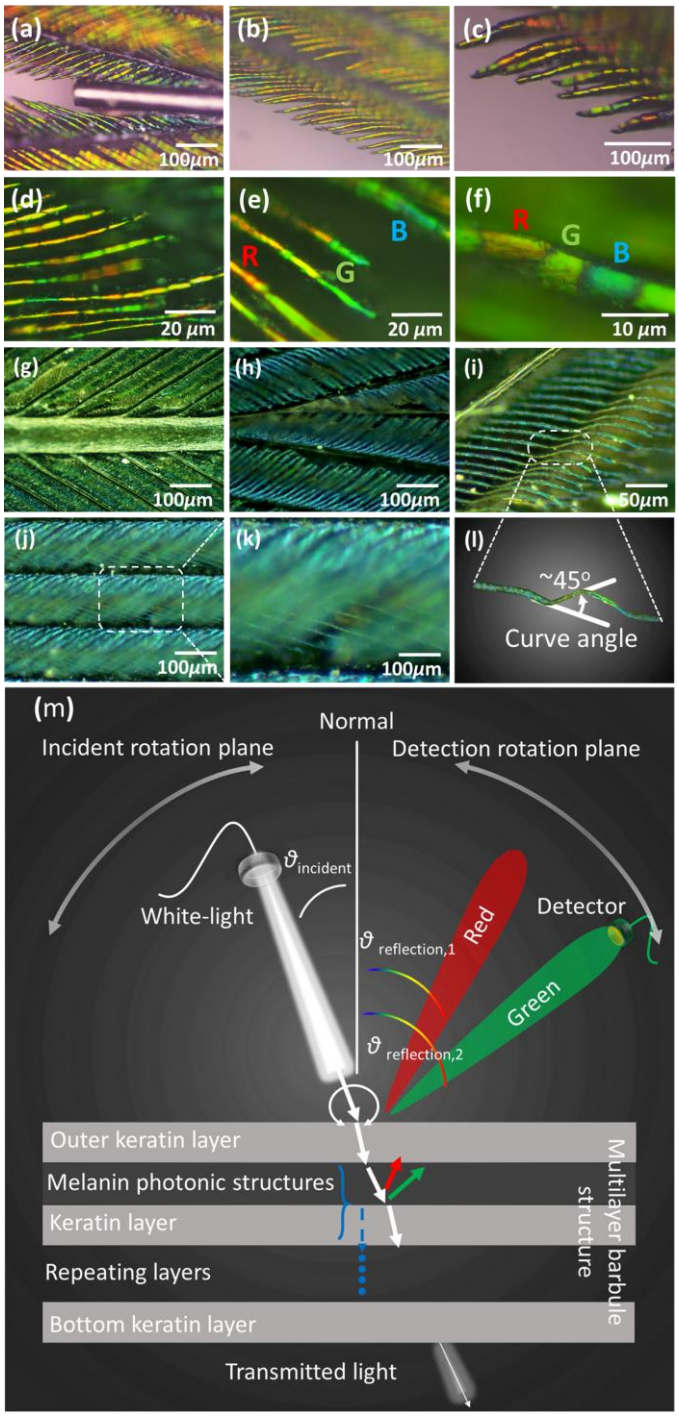

Figure 2.11. Mechanism of structural colouration in Nicobar pigeon feathers. **(a-f)** Microscopic images of predominant RG feather showing a range of colours spanning whole visible spectrum at some selected locations of the feather, where each segment possessed different colours. **(g-l)** Microscopic images of GB feather showing two dominant colours. In a single GB feather, angle resolution was the clearest, where tilt in the feather resulted in two different colours. Internal structural features were assumed to be different in each segment of the RG feather. The internal

structural profile was supposed to be more uniform that persisted almost all along the feather. Therefore, only two colours were visible because of the curve at almost midpoint of the feathers. **(m)** Schematic of the proposed colour-selective diffraction mechanism from a barbule structure of the feather.

2.3.2 Hydrophobicity

Nicobar feathers exhibited super hydrophobic characteristics. A contact angle of 156° was measured at the coloured part of the vane of a GB feather **(Figure 2.12)**. When the angle of elevation was varied from 0° angle to 90°, the droplet (2 μl) stayed clung to the surface. The feather surface was rotated in a way that the gravity pulled the droplet in opposite to the direction of the growth of feather barbules. The schematic diagram of the setup can be seen in **Figure 2.4** in section 2.2.4. **Figure 2.12c** shows different droplet sizes sprinkled over the feather, where super hydrophobic nature of the feather kept all droplets in stationary and spherical shapes. The dark part of the feather, the afterfeather, also exhibited hydrophobicity, where two droplets have been shown to retain a large contact angle at coloured vane and afterfeather regions of the feather of the Nicobar pigeon (**Figure 2.12d**). Notice that in the afterfeather the barbs and barbules have no particular distribution and are placed randomly, their random distribution does not deteriorate the hydrophobic properties. The Nicobar Islands experience heavy rainfall (up to 3800 mm per year), especially in the monsoon season, the super hydrophobic properties of the Nicobar pigeon's feathers explain the natural selection necessary for the bird's survival in such climatic conditions.

Micro- or nanoscale surface texturing has been used to enhance the hydrophobic properties of the range of different materials. Naturally occurring texturing is ubiquitous and present in the animal and plant kingdom. SEM was used to analyse the surface of the barbules **(Figure 2.12e-h)**. As mentioned earlier, the SEM imaging was performed with the help of Rayan Ameen. In the process, the feather was Au coated with a thickness of approximately 10 nm using DC

sputtering, before the sample was loaded for SEM imaging. This procedure was adopted in order to prevent the charging effect. The barbule density in the mid-section of the vane had a value of ~ 170 mm^{-1}; and therefore, the interspacing between the adjacent barbules was ~ 6 µm. SEM images revealed a non-smooth surface with protruded parts of keratin. In magnified SEM images, a long-range 1D periodic structure was also observed. The 1D structure resembled a grating and exhibited a duty cycle of ~ 1000 mm^{-1}, having a feature size of 100 nm, **(Figure 2.12h)**. These structure spanned over the length of the segment within the barbule.

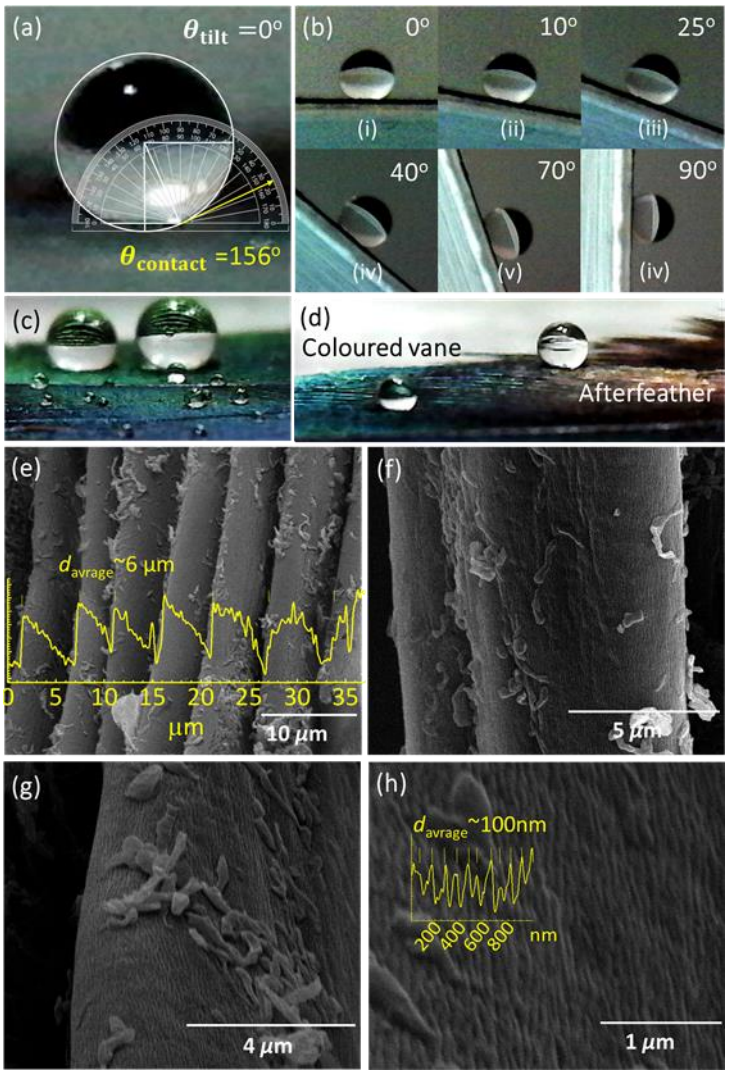

Figure 2.12. Contact angle measurements on a feather of Nicobar pigeon using Image J (protector in image used as an illustration schematic to display the value). **(a)** A water droplet (1 µl) having a contact angle of 156° at the vane of the feather. **(b)** Feather holds the water

droplet when rotated such that gravity pulls the droplet opposite to the direction of growth of the barbules. **(c)** Different sizes of water droplets sprinkled on the feather. **(d)** Two droplets cast on the coloured vane and afterfeather showing the superhydrophobicity of the feathers across its entire length. **(e-h)** SEM images of the top surface of the Nicobar's feather. Feathers feature a periodic having an average interspacing of ~ 6 μm. Nanoscale texturing has a periodicity of ~ 100 nm. Such texturing enhances the hydrophobicity of the feathers.

2.3.3 Refractive index based sensing

A RG feather based sensor is demonstrated in this study that shows a linear response over a large range of refractive index values. Although the feather is superhydrophobic, the interfacial and geometric properties can be exploited to sense the change in the refractive index of the liquid media by pouring it directly on the top of the feather and measuring the colourimetric response. For refractive index modulated sensing experiments, deionized water and different glucose concentrations ranging between 10 to 200 mM were utilized **(Figure 2.13)**. Dark-field optical microscopy with a spectrophotometer fixed at the objective was used to record the spectra for concentration measurements. The feather was placed under the optical microscope and the reference image (and related spectra) were taken in the dark field. The sensing zone was selected close to the end point of the main shaft, where optical effects were the strongest. After selecting the sensing zone, droplets with increasing glucose concentration were carefully poured using a micropipette. For each concentration, optical spectra were recorded and the droplet was removed from the feather using a microsuction syringe. The wavelength initially redshifted with DI water, followed by the positive trend with increasing glucose concentration; and thereby to an increasing refractive index. The underlying mechanism of sensing is due to the focusing properties of the curved droplet poured on the feather. The long wavelength initially diffracting at a large angle without a droplet now bends towards the normal of the feather plane on which it is placed. The increasing refractive index

due to increasing glucose concentration guides the longer wavelengths more towards the objective lens, resulting in the observed redshift. The initial sensor response was large (sensitivity ~ 0.28 nm/mM) and linear for concentrations between 0 to 50 mM, which tends to flatten for higher concentrations. The response (sensitivity ~ 0.03 nm/mM) saturated at 80 to 200 mM glucose concentration. These structures showing promising results with optical changes detected with refractive index modulation can be adopted and integrated in photonic bandgap hydrogel sensors currently used for glucose sensing.

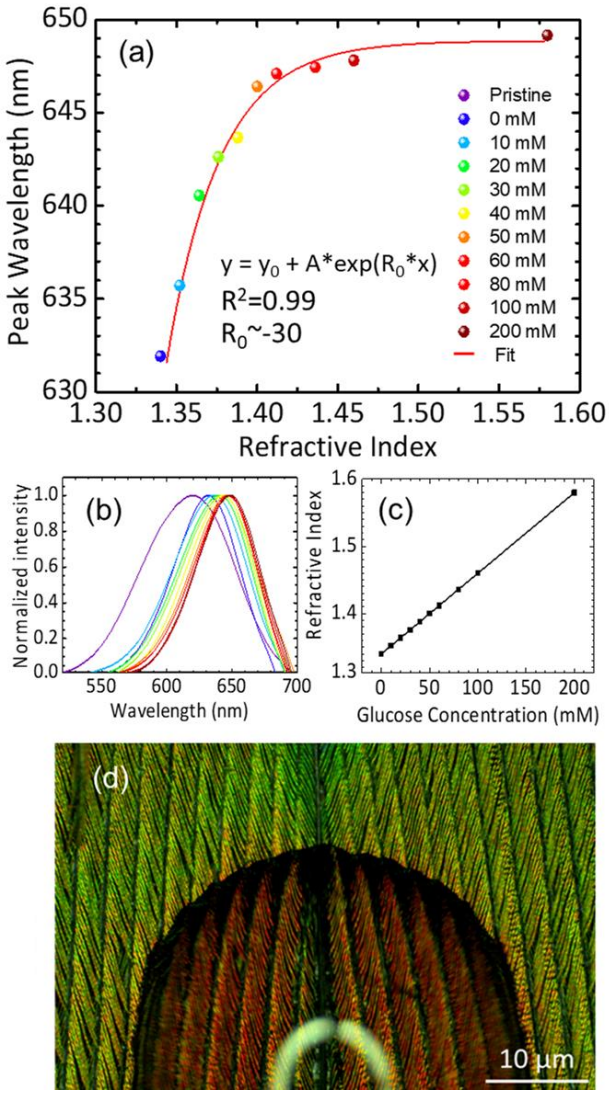

Figure 2.13. Refractive index sensing with Nicobar pigeon's feather. **(a)** Measurement of glucose concentrations from 0 to 200 mM. **(b)** Spectral shift with increasing glucose concentration. (**c)** Variation of the refractive index with increasing glucose concentration. **(d)**

Visual illustration of glucose sensing under an optical microscope. The feather surface undergoes a redshift upon pouring the glucose solution. The pristine region is unchanged.

2.4 Summary

The colour plumage of Nicobar pigeon (*Caloenas Nicobarica*) was studied using spectroscopy and angle-resolved measurements. The iridescence of colours was linked with the photonic bandgap structures coupled with melanosome layered structures in barbules. The feathers exhibited wavelength-selective diffraction of light at certain illumination/observation angles. These feathers also showed different colours when observed and probed at different locations on the feather, resulting in a rainbow-like behaviour. Contact angle experiments were carried out to assess the feathers' response against water. Superhydrophobic properties were measured resulting in a large contact angle of ~ 156°. The optical response of these feathers was also used for refractive index sensing. Due to the interfacial and geometrical properties at the interface between feather surface and solution, a redshift in optical spectra was measured with increasing glucose concentrations. Two linear sensing regions have been defined in low and high concentration regimes. It can be anticipated that these underlying mechanism of light diffraction can provide a deeper understanding of structural colouration in Nicobar pigeon and provide design criteria for engineering applications in wavelength-selective filters, smart sensors, photonic bandgap hydrogel sensors and nano-photonic devices.

Bibliography

1. Steadman, D., *The historic biogeography and community ecology of Polynesian pigeons and doves.* Journal of Biogeography, 1997. 24(6): p. 737-753.
2. Remsen Jr, J., *HBW and BirdLife International Illustrated Checklist of the Birds of the World Volume 1: Non-passerines Josep del Hoyo and Nigel J. Collar 2014. Lynx*

Edicions, Barcelona. 903 pages, hundreds of colour plates. ISBN 9788496553941. $209 (Hardcover). Journal of Field Ornithology, 2015. 86(2): p. 182-187.

3. Liu, Y., X. Chen, and J. Xin, *Hydrophobic duck feathers and their simulation on textile substrates for water repellent treatment.* Bioinspiration & biomimetics, 2008. 3(4): p. 046007.
4. ul Hasan, K., et al., *A miniature graphene-based biosensor for intracellular glucose measurements.* Electrochimica Acta, 2015. 174: p. 574-580.
5. Tsangarides, C.P., et al., *Computational modelling and characterisation of nanoparticle-based tuneable photonic crystal sensors.* Rsc Advances, 2014. 4(21): p. 10454-10461.
6. Yetisen, A.K., et al., *Photonic hydrogel sensors.* Biotechnology Advances, 2016. 34(3): p. 250-271.
7. Farandos, N.M., et al., *Contact lens sensors in ocular diagnostics.* Advanced healthcare materials, 2015. 4(6): p. 792-810.
8. Stavenga, D.G., *Thin film and multilayer optics cause structural colours of many insects and birds.* Materials Today: Proceedings, 2014. 1: p. 109-121.
9. Stavenga, D.G., et al., *Dramatic colour changes in a bird of paradise caused by uniquely structured breast feather barbules.* Proceedings of the Royal Society of London B: Biological Sciences, 2010: p. rspb20102293.
10. Riedler, R., et al., *A review of colour-producing mechanisms in feathers and their influence on preventive conservation strategies.* Journal of the American Institute for Conservation, 2014. 53(1): p. 44-65.
11. Kinoshita, S., S. Yoshioka, and J. Miyazaki, *Physics of structural colours.* Reports on Progress in Physics, 2008. 71(7): p. 076401.
12. Xiao, M., A. Dhinojwala, and M. Shawkey, *Nanostructural basis of rainbow-like iridescence in common bronzewing Phaps chalcoptera feathers.* Optics Express, 2014. 22(12): p. 14625-14636.
13. Leclaire, S., et al., *Feather bacterial load affects plumage condition, iridescent colour, and investment in preening in pigeons.* Behavioral Ecology, 2014. 25(5): p. 1192 - 1198.
14. Yin, H., et al., *Iridescence in the neck feathers of domestic pigeons.* Physical Review E, 2006. 74(5): p. 051916.

Chapter 3: Study on Structural Colouration in Himalayan Monal *(Lophophorus Impejanus)* Pheasants

The research work in this chapter is submitted for review in RSC Nanoscale. I am the main (first) author of this paper. Further details and co-authors contributions are as following:

Ijaz Rashid, Muhammad Umair Hassan, Muhammad Nazim, Qing Dai, Kamran Khattak and Haider Butt*. *"Structural colouration in Himalayan Monal, hydrophobicity and refractive index modulated sensing."* RSC Nanoscale

Ijaz Rashid: is the main (first) author and he observed the angle dependent colour change in the feathers. He modelled the experimental setups and conducted the experiments. He designed optical characterization setups and optical spectra setups. He has written the manuscript that was reviewed by Dr Muhammad Umair Hassan, Dr Qing Dai, Dr Kamran Khattak and lead supervisor Dr Haider Butt (*).

Muhammad Nazim: contributed towards collection of optical spectra, imaging and documenting procedures.

Dr Qing Dai: contributed towards the SEM and TEM imaging.

Chapter 3: Study on Structural Colouration in Himalayan Monal *(Lophophorus Impejanus)* Pheasants

3.1 Introduction

Structural colours in nature rely on the size and arrangement of physical microscopic structures that display selective reflectance of incident light [1]. Angle-dependent colours often termed as iridescent colours are seen in many living species, for example, beetles [2], dragonflies [3], butterflies [4], flies [5], ducks [6], peacock [7], pigeons [8], kingfisher [9], aquatic animals [10] and plants kingdom [10]. The uniqueness of structural colours in these organisms is due to the selection of one or more different types of nanometric architectures such as single or multi-layer thin-films, diffraction gratings, photonic crystals, and also due to other physical parameters, such as size and refractive index [11]. Such colouration is used by these species in order to communicate, show response and signalling purposes [12]. The significant change in colour at particular angles allows these species to signal each other of the intentions while remaining hidden from any predators [12].

Photonic structures are observed in many avian taxa, and vary within bird species that differ in size, behaviour, and ecology [13]. The essential characteristic of a photonic crystal is the periodicity of the dielectric material along one or more axes [14, 15], hence they can be one, two or three-dimensional, which is also the basis for their basic division. The photonic structure of a barbule is mainly derived from melanosome, keratin and air and can be arrayed in one-dimensional laminar nanostructures, two-dimensional crystal nanostructures, which may have square or hexagonal lattices, or even three-dimensional nanostructures [16]. Iridescent feathers of domestic pigeons were found to be composed of a surface keratin layer surrounding a

medullary layer and it was discovered that the structural colour originates from the light interference in this keratin surface layer [17], classed as one-dimensional in the form of multilayers. A study of dabbling ducks' wing patches showed the iridescent colours of the duck specula are formed by two-dimensional hexagonal photonic crystals (PCs) of rod shaped melanosomes set beneath a thin layer of keratin at the surface of the feather barbules [18]. Two-dimensional PCs have also previously been expressed in peacocks [7], which also belong to the pheasant family. These are unlike those observed in ducks because their lattices are square rather than hexagonal and have air between melanosomes rather than keratin [18]. The intensely coloured iridescent feathers of several hummingbird species, for instance, have been discovered to be because of the coherent scattering of light from multiple, interchanging layers of keratin and hollow air-filled, disc-shaped melanin granules [19, 20]. The iridescent colour of the male Peafowl (Pavo cristatus), by contrast, is created by crystal-like arrays of solid, rod-shaped melanin granules [16]. These different types of structures show the wide range of possibilities PCs can be arranged in nature. The aim of this study is to investigate the structural properties and optical effects of the feather barbules of the male Himalayan monal (Lophophorus Impejanus, **Figure 3.1**). The bird's feathers possess a layered internal structure as determined by transmission electron microscopy (TEM) that causes its brilliant metallic colours. A simulation model was used to estimate the outcomes of the profile of layered structure observed through TEM. The dimensions of the structure were measured from the images obtained through TEM and the material properties were integrated in the simulation model. The simulation results were than compared to the actual observations obtained by optical characterisation of feather samples in the lab. This comparison was necessary to get a clear indication of the controllable parameters in modulation of photonic properties of these feathers. These features can than be utilized in modelling and fabrication of optical devices such as colour selective filters, phtonic bandgap hydrogel sensors and colourimetric sensors.

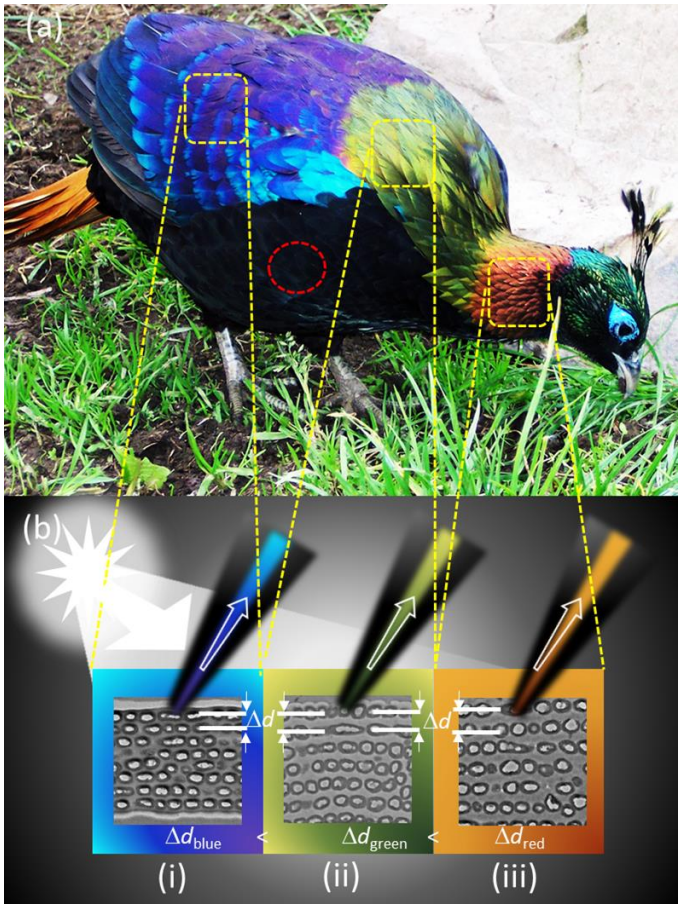

Figure 3.1. Himalayan Monal Pheasant (Lophophorus Impejanus). (**a**) The bird is a pheasant and the national bird of Nepal. Its strong and beautiful angle dependent iridescence (see yellow and red contours) is due to underlying photonic structures in its plumage. The range of colours, from red to blue, is due to the size effect of the photonic structure. (**b**) Illustration of the selective Bragg's reflection by showing the internal structure of feathers taken from different parts of the bird's body. More details and discussion on size and gap of the internal structures is discussed in Figure 3.4 under Section 3.3.

3.2 Methods

3.2.1 Optical Microscopy

Optical microscopy was carried out using microscope (Axio Scope.A1, ZEISS, Jena, Germany) as previously mentioned in Section 2.2.1. BF and DF imaging was performed and spectra were collected using optic fibres. The microscopic images were captured by a camera

placed on top of the microscope connected to the computer using ZEN imaging software (ZEISS, Jena, Germany). The spectra were measured using Ocean View software (Halma PLC, Amersham), with a 2.0 nm resolution spectrophotometer (USB2000+, Ocean Optics, Oxford) that transmits broadband light through an optical fibre connected to the microscope.

3.2.2 Spectroscopy

Spectroscopic measurements were carried out on the feather samples using a spectrophotometer (USB2000+, Ocean Optics, Oxford) along with Ocean View software installed in the computer as explained in Section 2.2.2. A special optic fibre having a combination of seven optic fibres inside was used to transmit and receive the reflected light from the feather. Spectra and images were captured on a spot (diameter = 4 mm) on the feather surface. Photographic images of each feather were then taken using a fixed digital camera.

3.2.3 SEM and TEM imaging

The feathers were first cleaned with ethanol and dehydrated. Feather samples for scanning electron microscopy (CFEI Quanta 3D FEG FIB-SEM) were coated with Au (thickness ~ 20 nm) using DC sputtering and cured to prevent the charging effect during electron microscopy. Samples were than mounted to analyse the surface profile of the barbules. Feather samples for transmission electron microscopy were infiltrated with EMbed 812 resin after the cleaning and dehydrating process. Samples were then placed in block moulds and cured at 60°C overnight. The blocks were then trimmed and sections were cut from different parts. These sections were then mounted on copper grid for TEM imaging.

3.2.4 Computational Modelling

COMSOL (V5.1) was used to simulate the internal alternating layered structure of feathers using respective refractive indices and different periodicities of the layers to show reflection comparable to red, green and blue feathers. A variable mesh element size from 9 nm

to a maximum of 50 nm was used in all simulations. The minimum size was adopted in the near field region and inside the structure in order to have more points for calculations in this region. A maximum mesh size was adopted in far field region where the change between the adjacent points was not significant. This method was adopted to make efficient use of memory and computation time needed for simulations. More detail on finite element method, mesh size selection and equations used by COMSOL (V5.1) is provided in Section 4.2.1.

3.2.4 Hydrophobicity

The sessile drop method was used to evaluate the contact angle between the feather's surface and the water droplet. A droplet of 2 µl was placed on the proximal and distal ends of feather using a micropipette (SP0020-Auto, SciQuip, Shropshire). The feather was rotated in order to change the tilt angle from 0° and 90°. A high-resolution camera was used to capture the images. ImageJ (Wayne Rasband, National Institute of Health, USA) software was used for analysis and measurements. The hydrophobicity measurement setup used was same as previously displayed in **Figure 2.3** detailed in Section 2.2.4.

3.2.5 Sensing Response

The feather was first placed under the optical microscope (Axio Scope.A1, ZEISS, Jena, Germany) and the relevant area was brought into focus. Image was captured using the ZEN imaging software. A droplet of size 2 µl was then dropped using the micropipette on the same spot under focus. The barbules absorbed the liquid droplet. Images were recorded using ZEN imaging software for wet conditions as well as dry state when the feather dried. Various liquids and solutions were used with difference in refractive indices. Images were captured in each case. Reflection spectra received were also recorded in the same manner to observe the peak shift in wavelength. An optic fibre was connected to the microscope in place of camera to receive the reflection spectrum. Ocean View software and spectrophotometer (USB2000+,

Ocean Optics, Oxford) were used to receive and view the optical spectra. Droplets of different liquids and solutions were used to see the effect and the spectra received were recorded. The results were than plotted together to observe the peak shifts in wavelengths.

3.3 Results and Discussion

In order to record a closer in view of the change in colour when varying observation angles on the feather's perceived colour, a camera was used to take pictures at 0 and 45° angles of incidence under a normal ambient illumination (**Figure 3.2a**). The pictures captured were of the microscopic zoom for all the feathers, showing distinct shifts in the intensity of their respective colours between iridescent metallic and dark with the change in illumination angle between 0° to 45°, respectively. Feathers' barbules were vivid in colour and had metallic perception, however, the afterfeathers and downy barbules were observed to be showing no change in colouration (**Figure 3.2c-d**, photographic images).

Optical spectra were recorded at normal to the feather surface with illumination angle of ~ 15°. The feather surface was rotated by mounting it on a rotational stage setup with increments of 10° between 0 to 360° in each step (**Figure 3.2e**). The experiment was conducted to appreciate the drastic appearance and disappearance of the reflected beam in terms of the spectral intensity – to an observer, the feather appears bright metallic at some angle and becomes very dark when there is a slight change in the viewing angle. Measurements were taken on the most iridescent spots (diameter = 4 mm) on the feathers (**Figure 3.2f-h**). To observe the angle dependence of the reflected light intensity, peak maxima obtained from the reflection spectra were also plotted against the rotation angle. The red feather showed the strongest change in the intensity upon rotation through 360°. The feather exhibited two intense peaks (angular span of ~80°) during the complete rotation, beyond which it appeared very dark. The green feather showed a broader angular span of 150° of high reflection intensity having

two overlapping peaks, the feather appeared dark in the regions other than the high reflectivity angles. The blue feather showed multiple peaks through 360°, however it never became completely dark (giving intensities below the lower resolvable limit) during the full 360° rotation. It was noticed that the arrangement of barbules in feathers at the macroscopic scale severely affected the overall reflection behaviour. Feathers at the bird's back had slightly different arrangement compared to the feathers at neck and tail. By the same token, the location on the feather on which measurements were taken also affected the angle dependence of the reflected light, that is, feathers have different arrangement and densities close to the main shaft compared to the distal ends. Nevertheless, all iridescent parts of these feather showed high angular dependence of the reflected intensity. Structural colours show angular dependence by appearing iridescent/metallic at certain angles and dark on others [21]. The internal nanoscopic structures define the characteristics of a structural iridescent feather. The observed angular dependence of Monal's feathers suggested that 2D photonic crystals (multi-layered structure) could be present in these feathers, similar to some other avian species [22, 23] .

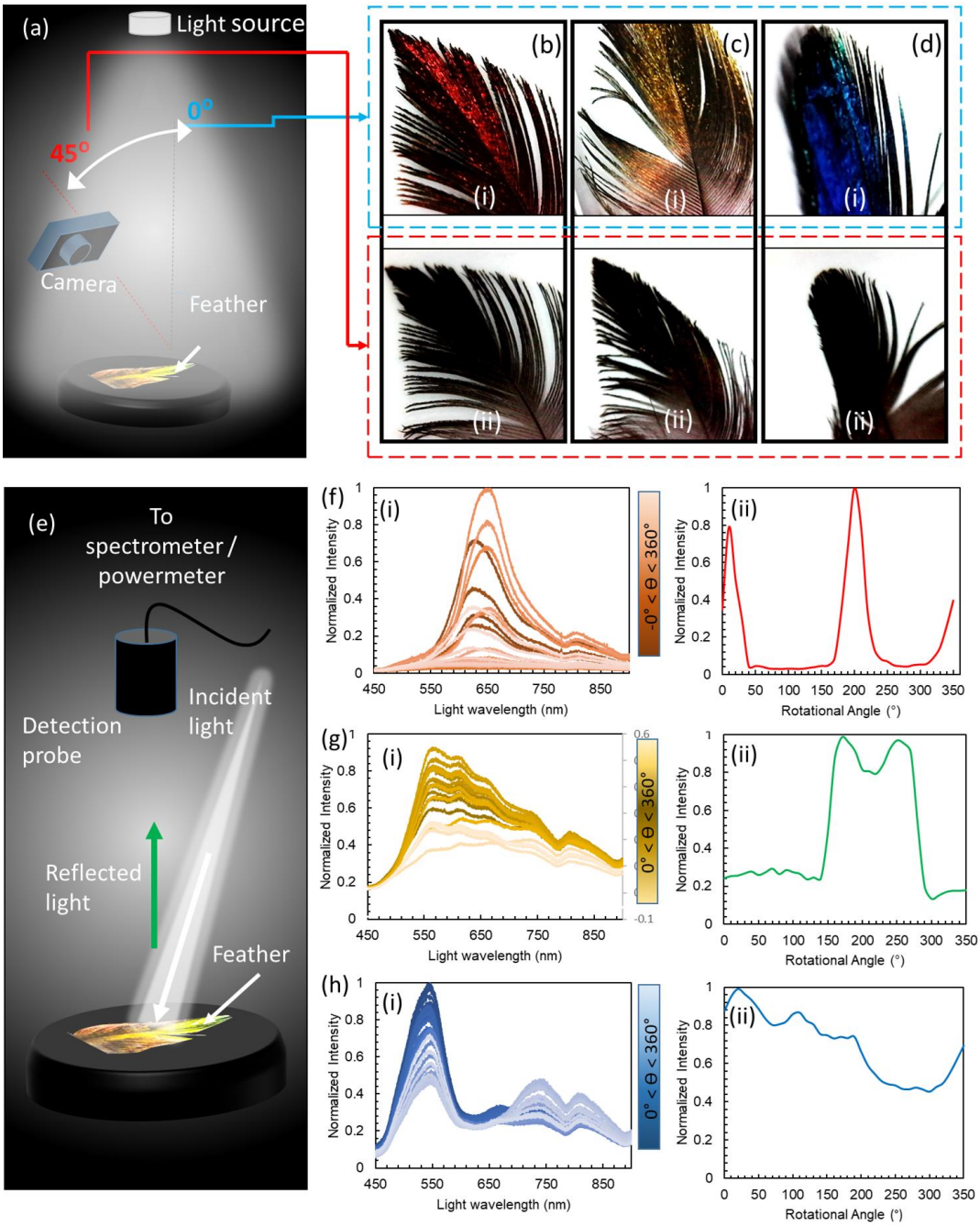

Figure 3.2. Colour perception of the Himalyan Monal's plumage. (**a**) Schematic for varying observer angle in ambient light. (**b-d**) Images of red, green and blue feathers at an angle of observation at i) 0° and, ii) 45°, respectively. (**e**) Schematic for normal observation angle with illumination at angle of 15°, and, feather rotation through 0-360°. (**f-h**) Behaviour of reflected beam with changing rotation angle of red, green and blue feather: i) reflection spectra with varying rotation and, ii) peak intensities with variation in rotation angles, respectively.

Dark and bright field microscopy modes (Ziess, 20x) were used to observe the surface, exterior's structure and colours of red, green and blue feathers of the Himalayan Monal under two illumination settings (**Figure 3.3d-f**). In the bright field (BF) mode, each feather's iridescent barbule appeared elongated, enlarged, flat and twisted at the bottom surface so that the flat surface of the barbules became in parallel with the feather's surface. The flattening barbule stacked up on each other, orienting several reflecting parallel structures at the same angle. Distinct barbule morphology is common among the birds with iridescence that enhances the effectiveness of iridescent colour displays [16, 21]. The increased numbers of stacked reflecting planes (barbules) in Himalayan Monal increased their vividness and made them appear extremely metallic. When in comparison with the less coloured (proximal end) of the Monal feather (**Figure 3.3g**), the negative impact that the reduced available surface plane had on its ability to reflect the incident light was significant. Another important feature of these feather was their geometric truncation of barbules. The barbule ends had sharp rectangular-faced terminations, which may be due to their internal highly order structure/photonic crystals. The underfeather appeared dark grey and did not exhibit any visible colouration (**Figure 3.3h**). Microscopic images of all feathers taken in the BF mode showed red, green and blue colours, while dark field (DF) images appeared dull as if no reflection was reaching to the eyepiece, indicating the angle selectivity of such photonic colouration. Notice that, in the BF, the light is incident from the top, while the imaging is also carried out from the same angle, whereas, in the DF, the illumination occurs at certain angle and scattered light is collected from the objective placed with plane normal to that of the object (feather). The observation is consistent with that generally experienced at the macroscopic scale. It was observed that barbules and hooklets attached with barbs (in the vane section) were responsible for iridescent colours and photonic effects in all feathers. Barbs, rachis, or shaft did not exhibit photonic effects.

The camera at the eyepiece was replaced with a spectrometer (Ocean Optics, USB 2000+) and reflection spectra was measured from the same locations of red, green and blue feathers in the BF and DF modes (**Figure 3.3i-k**). All feathers showed a clear change in the intensity of the colour/wavelength peak, with the barbules appearing bright (high intensity) under BF mode whereas they appeared dark (low intensity) in the DF reflecting mode – no appreciable change in the peak wavelengths was observed. Normalized wavelength intensity graphs were plotted and the peak wavelength for the red, green and blue feathers were found to appear at ~ 620, 520, and 495 nm, respectively. The reflection of the underside of the feather was not within the resolvable limit of the spectrometer, while observed in both, the BF and DF modes. Since, all feather showed a large change in the intensity of the colour with changing illumination angle, it can be deduced that the observed colours were due to the internal structure of the feathers. Such colouration behaviour (selective wavelength reflection and angular dependence) is the characteristic feature of photonic crystals.

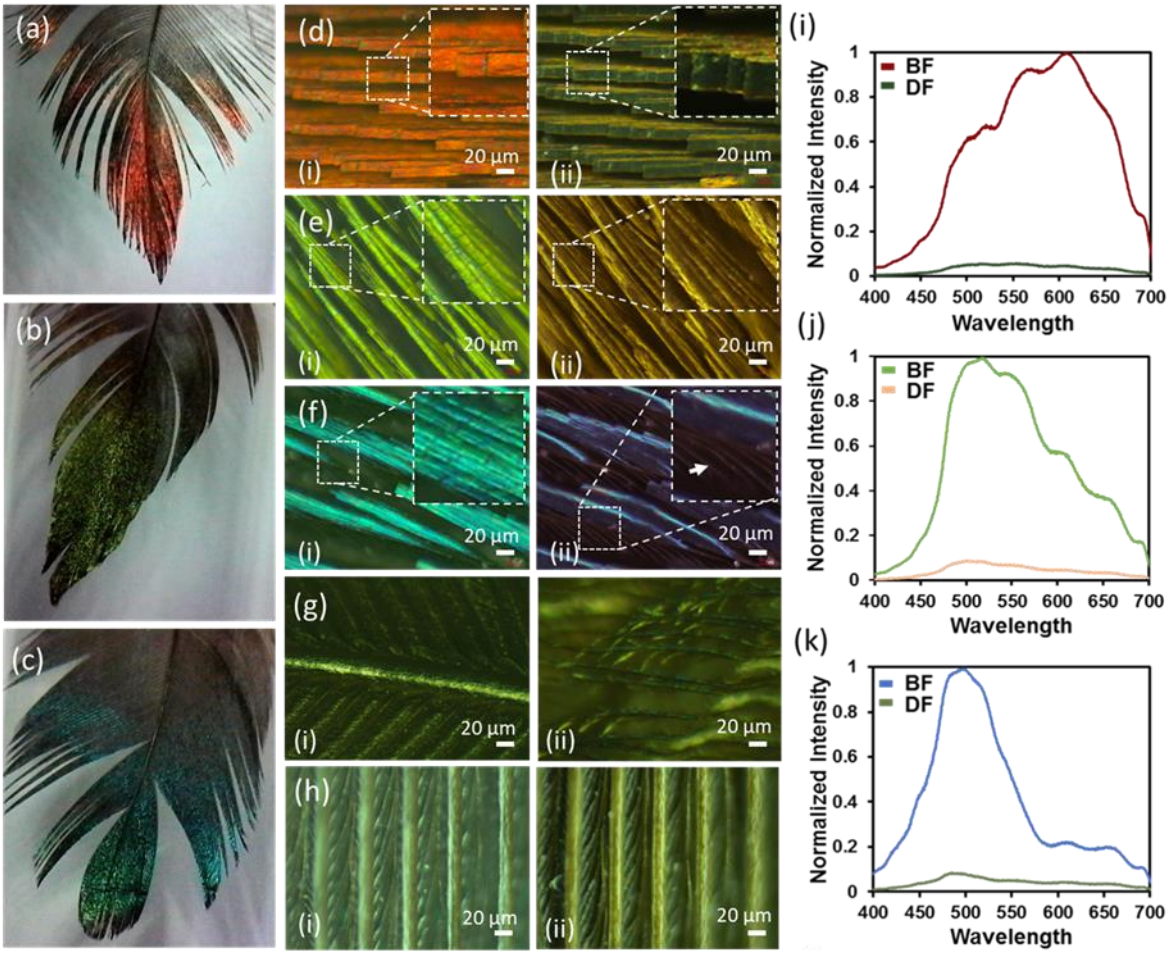

Figure 3.3. Feathers of Himalayan Monal and their colours. (**a-c**) photographic images of red, green and blue feathers, respectively. **(d-f)** Bright-field (i) and dark-field (ii) microscopic images of the red, green and blue feathers taken from the top iridescent to side of feathers. **(g)** Bright field (i) and dark field (ii) microscopic images of the underside of the blue feather, all other feathers (not shown here) appeared the same from the bottom. **(h)** Bright field (i) and dark field (ii) images of the proximal region showing lack of colour in this particular region of the feather. Scale bar: 20 µm unless stated otherwise. **(i-k)** Visible reflected spectra recorded in the bright and dark field modes: strong reflection behaviour was observed in the bright field mode, while feathers the dark field mode were almost completely non-reflecting.

TEM images were obtained to see the details of the internal structure of the red, green and blue feathers (**Figure 3.4a-c**). TEM imaging was performed with the help of Dr. Qing Dai.

His experienced group in imaging at Nanophotonics Research Division, CAS Center for Excellence in Nanoscience, National Center for Nanoscience and Technology, Beijing, China lead us to quick identifying of the structures and capture images. It was observed that the barbules of the Himalayan Monal feather contain oval structured hollow melanin granules, layered parallel to the barbule surface, arrayed in 6-9 layers and perhaps connected by keratin. Oval-shaped hollow melanosomes-like structures were observed that were aligned in the form of layers as in a Bragg reflector. To define the class of the feathers, Himalayan Monal's structure of melanin granules is categorized as R-type (hollow tube), and its arrangements of granules as S-type (multilayer), considering Durrer [15, 23]. Therefore, the generic structure among all feathers was considered as to be the RS-type. A close look revealed that the size of hollow melanin granules did not change significantly for all feathers. The average radii measured along the minor axes of these structures obtained from the images of TEM were noticed to be almost the same, that is, 300 (± 30) nm for red green and blue feathers, respectively. However, it was noticed that the distance between their layers changed significantly – the average distances between the layers were ~ 147 (±20), 110 and 63 nm for red, green and blue feathers, respectively. Keratin and melanin have been reported to have various refractive indexes causing light to be reflected at the boundaries (and at interface with air) and thus the barbules act as optical multilayers, similar to other reports [22]. It has been observed that the contrast of the refractive index between the outer and inner melanin layers could be quite significant, $n_{\text{outer}} \approx 2$ and $n_{\text{inner}} \approx 1$), hence the constructive interference that occurs can easily be observed in the form of colour change [22]. A continuously layered keratin covers the melanin granules. The refractive index of the surface keratin layer and the change in refractive index with the surrounding medium air ($n \approx 1$) can also produce the structural colour. However, the overall barbule refractive index depends on the relative amounts of keratin and melanin density in the feather's body [24].

As mentioned in methods section, finite elemental method (COMSOL V 5.1 software) was used to model the estimated emission profile of the layered structure (**Figure 3.4d-f**). The following approximation made by C J R Sheppard for calculation of reflection coefficient 'R' was used to measure reflectance for two repeating materials with odd number of total layers [25].

$$R = \left[\frac{1 - (n_1/n_2)^{2N}\,(n_1/n_{air})}{1 + (n_1/n_2)^{2N}\,(n_1/n_{air})}\right]^2 \qquad \text{……(Eq. 3.1)}$$

where, n_{air} (=1) is the refractive index of air, n_1 (=1.4) and n_2 (=1.6) are the, refractive indices of the alternating layers, while N is the number of even layers involved in the structural reflection process. For the sake of simplicity, multiple layers of continuous films were used for simulation. The peak intensities for the three different sets of parameters were observed at ~ 610, 540, and 460 nm, which is in agreement with the practical optical characterisation results observed in lab for different feather samples under discussion.

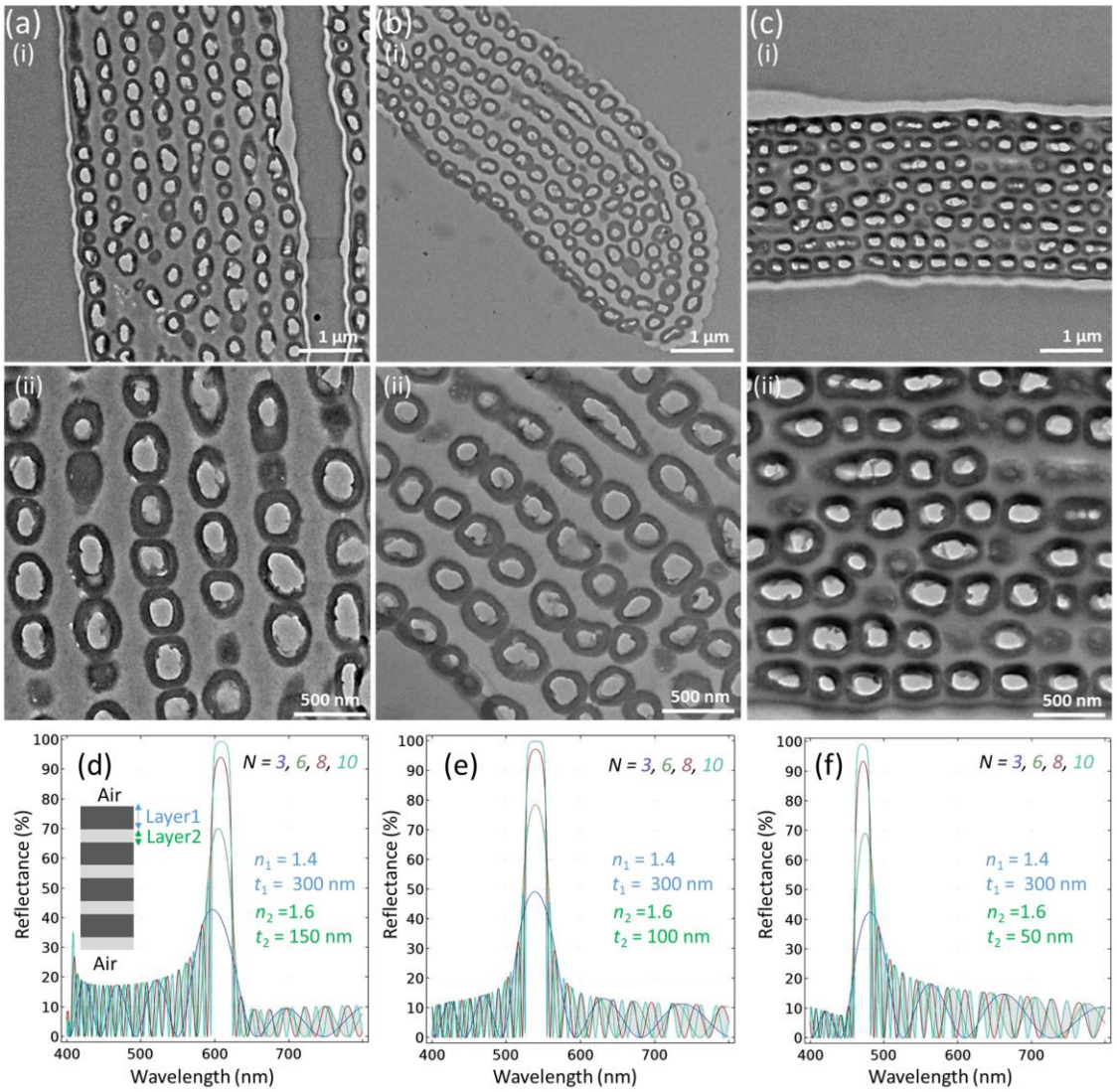

Figure 3.4. Internal structure of Himalayan Monal feather. (**a-c**) TEM images red, green and blue feathers respectively with i) low and ii) high zoom. All feathers had layered internal structure. (**d-f**) Finite element simulation of a layered structures with different periodicities to show different reflection comparable to red, green and blue feathers, respectively.

Wettability properties of the feathers were tested using sessile drop method. A droplet of 2 µl was placed on the proximal and distal ends of the feather in order to see the effect in both areas (**Figure 3.5d**). The results suggested that each end had slightly different wettability. The overall feather surface was hydrophobic as all recorded contact angles were over 90°. The droplet had a contact angle of ~ 120° was observed at 0 minutes between the droplet and the

proximal area of the feather. It decreased to an angle of ~ 115° within 5 minutes. Proximal area is the non-coloured end of the feather that has random or no structures inside. The droplet placed on the distal area (coloured) of the feather exhibited a smaller contact angle of ~ 110°, that within 5 minutes decreased to an angle of ~ 90°. Hydrophobicity in feathers is attributed to the layered structure of barbs and barbules with respect to width and spacing between them as well as the internal structure arrayed in a manner that it reduces the contact between water droplet and the hydrophilic keratin [26]. The decreased (increased) hydrophobicity of the most (least) iridescent distal (proximal) area of the feather could suggested a trade-off between the iridescence and hydrophobicity in these feathers. Droplets poured on distal and proximal parts of the feather did not fall off and remained attached to the surface when the feather was tilted at 90°, which also suggests weaker hydrophobic nature of these feathers. Scanning electron microscopy (SEM) of Au-coated feather revealed pores on the surface of the barbule that can also result in increased water affinity on these feather. As mentioned earlier, SEM imaging was performed with the help of Dr. Qing Dai. Hydrophobic surface of feathers is useful for birds because of their self-cleaning ability – as a result of the water droplets rolling off the surface carry any surface contaminants with them. Nevertheless, it was noticed that the hydrophobic behaviour of these feathers appeared to be weaker as compared to many other avian species, where contact angles could be very large, even with super hydrophobic properties. A decreased hydrophobicity will mean an increase in hydrophilic property of the feather that will reduce the self-cleaning ability of the feather. [27].

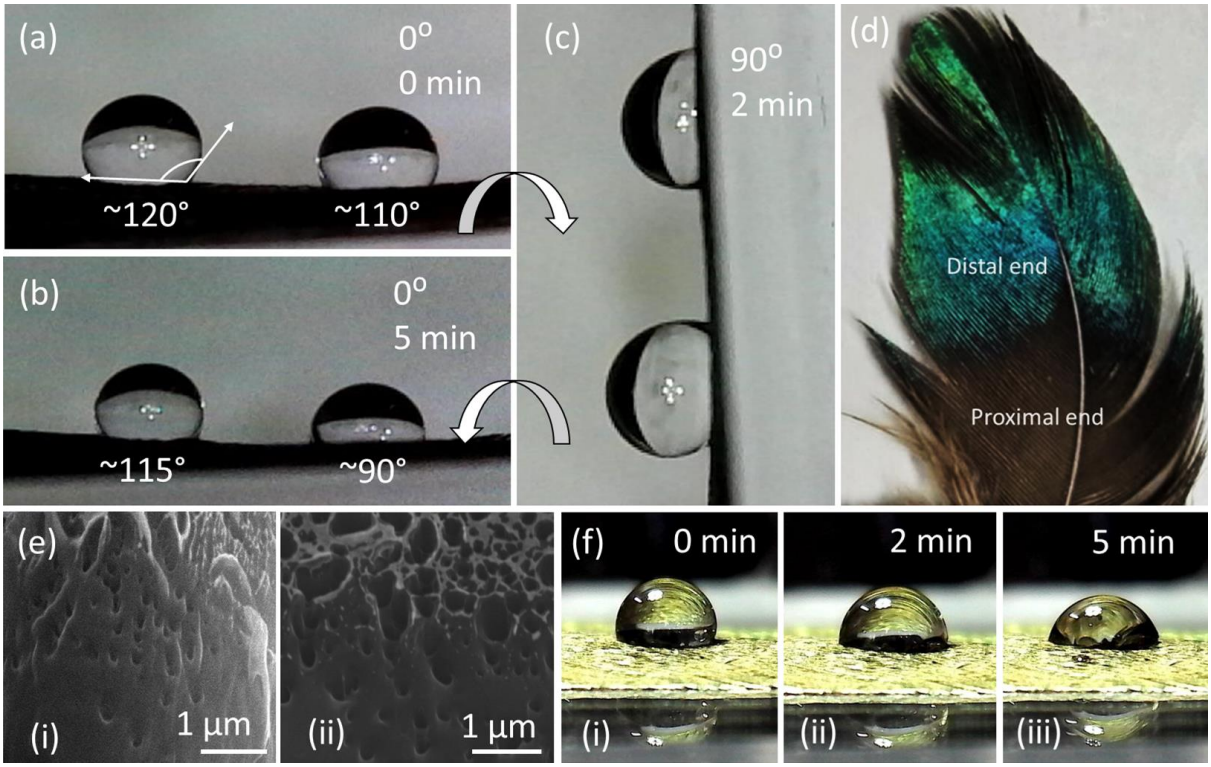

Figure 3.5. Hydrophobicity measurements using Image J and SEM imaging of the feathers. (**a**) Image of the droplets at 0° tilt angle, one placed in the proximal area of the feather and the other in the distal area. (**b**) Image after 5 minutes with a tilt angle of 0°. (**c**) Image captured after 2 minutes at a tilt angle of 90°. (**d**) Image of distal and proximal area on feather. (**e**) SEM images of the feather barbule. (**f**) Images of change in contact angle on the distal end showing absorption with the time lapse.

3.3.1 Water sensitivity

Interesting reversible colour shifts were recorded when the feathers were soaked into water (**Figure 3.6**). Photographs, recorded spectra and microscopic images captured were obtained to observe the difference between wet and dry states. The soaking allowed the feathers to absorb water, which resulted in a colour shift. The red feather showed a strong blue-shift (656 to 496 nm) and turned blue on soaking in water (**Figure 3.6a**i-vi**, c**), whereas, green and blue feathers exhibited red-shifts from 548 to 644 nm (**Figure 3.6b**i-vi**, d**) and 495 to 500 nm

(**Figure 3.6c**i-vi**, f**), respectively after they were soaked in water. As a general trend, the overall spectra broadened significantly in the soaked condition. The change in colour in wet state occurred with 30 s, and had reversed back to its original colour within 5 min (as soon as they became dry).

The observable change in colour, when feather is soaked, could be attributed either to water infiltrating the air spaces in the melanin rods or due to keratin swelling after absorbing water, or a combination of both. A study was conducted by Liu on the colour variation in scales of longhorn beetles in wet condition. The investigation concluded that the internal structure responsible for the change in colour was a multilayer structure , with two alternating layers having different refractive indices [28]. The first layer noticed to be a melano protein layer whilst the second layer contained melano protein nanoparticles and air voids. The study suggested that the colour change was due to two phenomena. Firstly, the absorption of water in the first layer of melano protein and secondly the infiltration of water into the air voids in the second layer. We suggest that a similar process was plausible in our case, where the water was absorbed by the keratin in the surface layer and the water also penetrated the air voids in the hollow melanin granules within the multilayer. Consequently, the refractive index contrast at the interfaces between air and keratin/melanin reduced, resulting in the constructive interference of light at a modified wavelength. It has been noticed that about half of the amino acids in feather keratin structure are hydrophilic and the other half are hydrophobic [29]. The surface profile and properties of the fibre are mainly dependent on the number of hydrophobic amino acids that are in the core or external to the surface of the fibre. The longhorn beetle responded to the wet state with a change in colour in a few minutes [28], whereas the Himalayan Monal feather responded in few seconds because of the porosity in the iridescent distal part of the feather, increasing the surface area available for keratin to absorb the water. Also, the

capillary effect due to the pores cannot be ruled out that quickly incorporated water in the nano/micro-voids within the feathers' body.

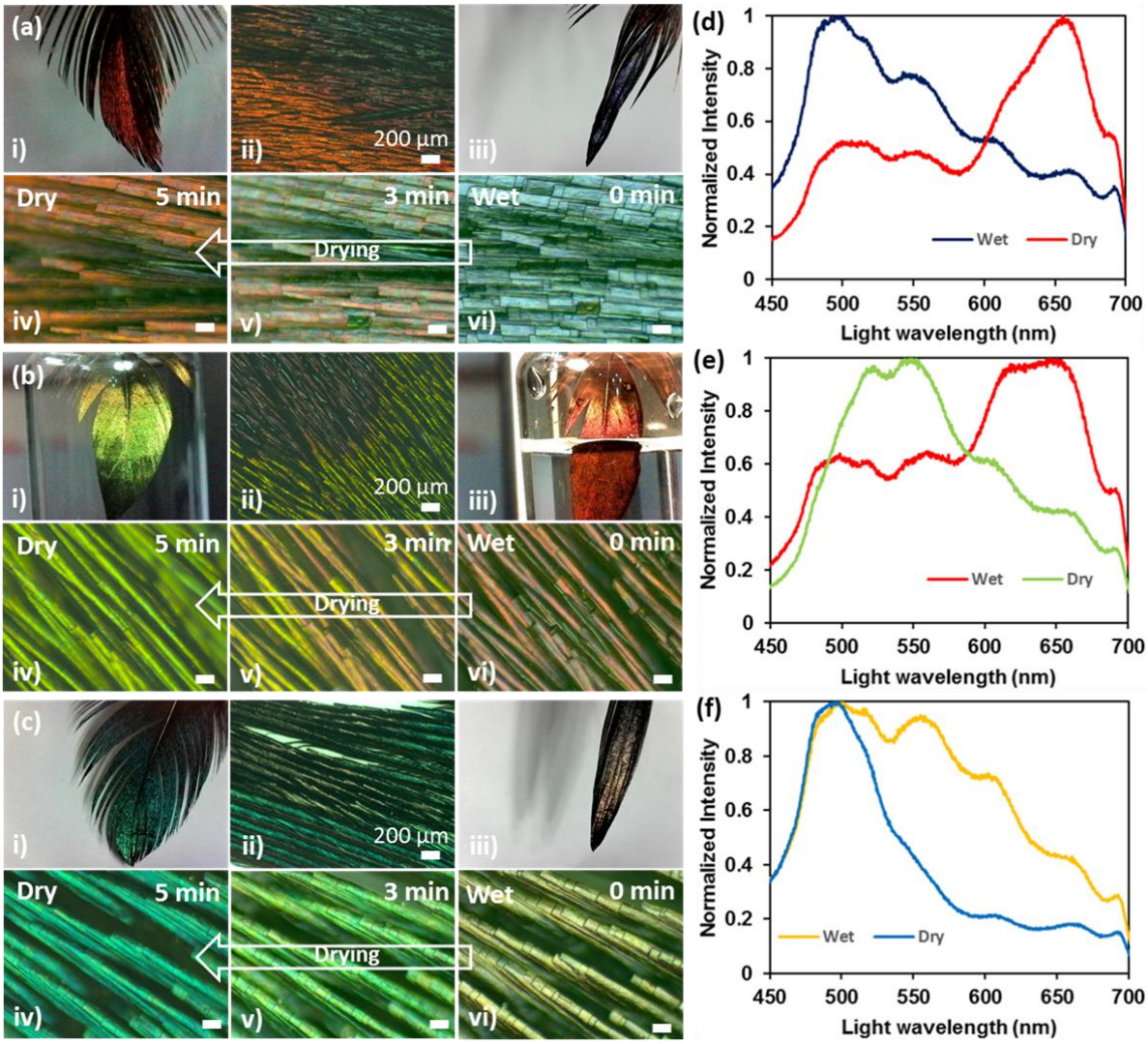

Figure 3.6. Feathers soaked in water. (**a**) Red feather i) dry condition, ii) mixed condition, iii) fully soaked state, iv) returned to dry, v) mixed state, vi) completely soaked, turned blue. (**b**) Green feather i) dry, ii) mixed state, iii) fully soaked, iv) retuned to dry, v) mixed state, vi) completely soaked, turned red. **(c)** Blue feather i) dry, ii) mixed state, iii) fully soaked, iv) dry again, v) mixed state, vi) fully soaked, turned yellow. (**d-f**) Plots of optical spectra recorded showing peak shift in wavelengths in dry and wet conditions for red, green and blue feathers, respectively.

3.3.2 Refractive index based sensing

Different solutions (alcohols: glycerol and ethanol, and glucose: 20 and 200 mM solutions) were used to soak red, green and blue feathers to observe the subsequent colour shifts. The colorimetric measurements were recorded *via* optical microscopy and by taking the spectral data for all immersion solutions (**Figure 3.7**). Ethanol gave a pink appearance to the red feather barbules, whereas glycerol displayed a purple colour, whereas, 20 and 200 mM glucose solutions made the feather dull and less reflective with a peak shift to ~ 495 nm, showing a blue appearance. The reflection spectra for green and blue feather measurements showed similar trends (**Figure 3.6**), with the major changes in colour wavelengths being the glucose and water liquid solutions compared to the alcohols and dry conditions.

The differences in colour change response were recorded for ethanol on the feathers as well as glycerol showing observable changes. A change in colour peaks was recorded for 20 mM and 200 mM glucose concentration solutions showing shift in peak wavelengths. It is noticeable that the overall change was observed to be greater for alcohols than water based solutions, although the difference in refractive indices between ethanol and glycerol (0.11) being half the difference between the refractive indices of 20 mM and 200 mM glucose concentrations (0.22). This phenomenon was observed for all the feathers. The drastic changes to colour and the shift in peak wavelengths can be attributed to swelling of keratin for the water-based solutions having dominant effect on the feather barbule's refractive index with increased swelling of keratin. The swelling of keratin is due to hydrophilic amino acids in the keratin structure causing the keratin layer to swell after water absorption. It is suggested that this absorption does not occur in case of alcohols. However, the colour change seen for alcohols is purely due to melanin rods being filled with these liquids forming multilayers structure with repeated alternating layers having different refractive indices (**Table S1, Appendix A**). First layer being the keratin layer whereas the second layer is formed by the melanin rods filled with

respective liquid. This means that the refractive index contrasts at the interfaces of air, keratin and filled melanin rods is different for each solution based on the difference in refractive index of each solution; thus, a multilayers structure is formed resulting a variety of colours based on the solution in which the feather is soaked.

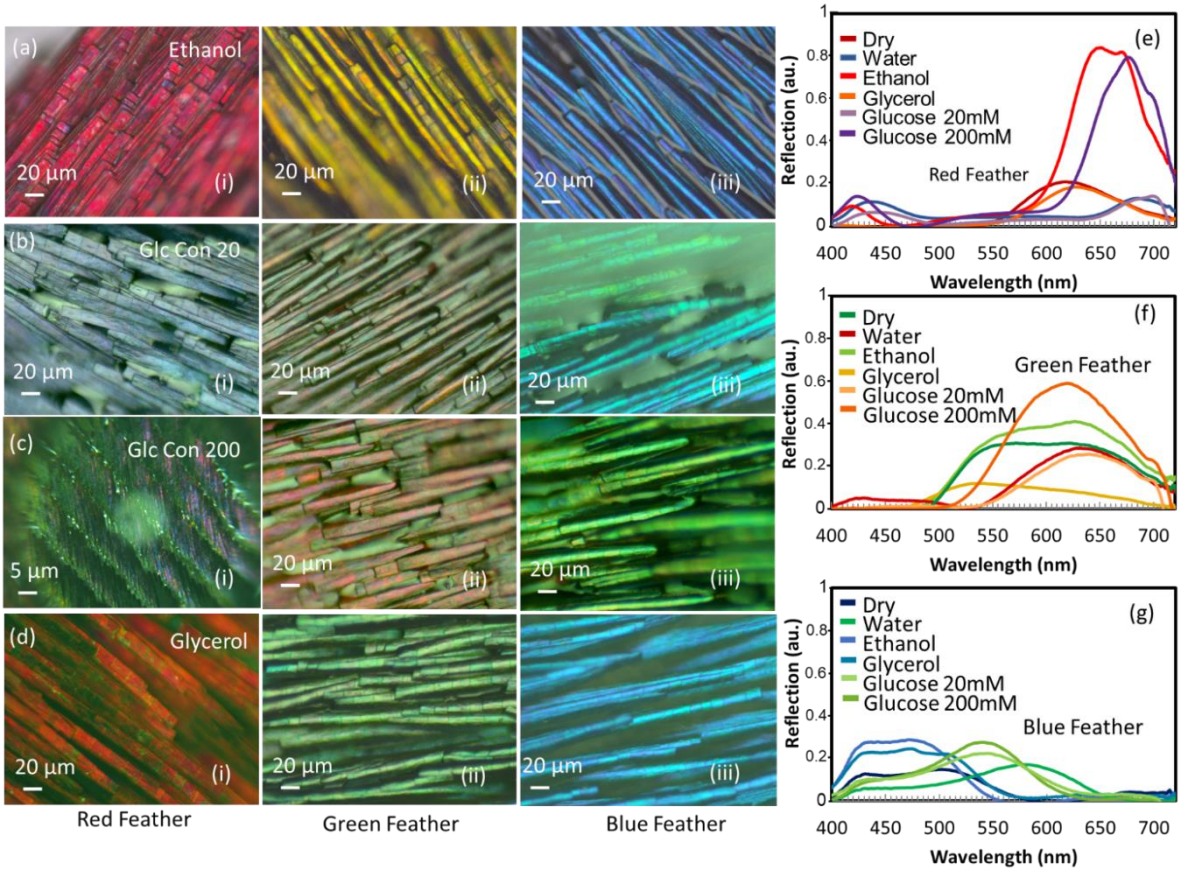

Figure 3.7. Sensing for different solutions. (**a-d**) Microscopic images of red (i), green (ii) and blue (iii) feathers immersed in (**a**) Ethanol, (**b**) 20 mM glucose solution (**c**) 200mM gulcose solution and (**d**) Glycerol. (**e-g**) Reflection spectra recorded for various solutions showing a change in peak wavelengths in dry and soaked conditions for red, green and blue feathers, respectively.

3.4 Summary

The iridescence of Himalayan Monal's feathers was found to be structural iridescence due to 2D photonic crystals present in the body of the its feathers. The TEM images of feathers taken from different parts of the bird's body revealed an RS-type structure present in all feathers

according to Durrer's classification. The bird's feathers show poor hydrophobicity in contrast with many other avian species. When exposed to the liquid, the feathers showed a rapid change in their colours, that reversed within ~ 5 minutes upon drying. The effective refractive index and swelling of the entire (/partial) structure of the feather was responsible for such colour modulation. The property of changing colour was exploited to sense other liquids. The reflection spectra were measured to sense alcohols and other water-based solution, which suggested alcohols can be sensed more effectively as they produced huge spectral shift in the reflected colour. The feather behaved differently to alcohol and water based solutions. Modulation of photonic properties of these feathers can be utilized in photonic bandgap hydrogel sensors, colour selective filters and colourimetric sensors.

Bibliography

1. Parker, A.R., *515 million years of structural colour.* Journal of Optics A: Pure and Applied Optics, 2000. **2**(6): p. R15.
2. Sharma, V., et al., *Structural Origin of Circularly Polarized Iridescence in Jeweled Beetles.* Science, 2009. **325**(5939): p. 449-451.
3. Vukusic, P. and D.G. Stavenga, *Physical methods for investigating structural colours in biological systems.* Journal of The Royal Society Interface, 2009. **6**(Suppl 2): p. S133-S148.
4. Butt, H., et al., *Morpho Butterfly-Inspired Nanostructures.* Advanced Optical Materials, 2016. **4**(4): p. 497-504.
5. Hespenheide, H.A., *A novel mimicry complex: beetles and flies.* Journal of Entomology Series A, General Entomology, 1973. **48**(1): p. 49-55.
6. Eliason Chad, M. and D. Shawkey Matthew, *A photonic heterostructure produces diverse iridescent colours in duck wing patches.* Journal of The Royal Society Interface, 2012. **9**(74): p. 2279-2289.
7. Zi, J., et al., *Coloration strategies in peacock feathers.* Proceedings of the National Academy of Sciences, 2003. **100**(22): p. 12576-12578.

8. Osorio, D. and A.D. Ham, *Spectral reflectance and directional properties of structural coloration in bird plumage.* Journal of Experimental Biology, 2002. **205**(14): p. 2017.
9. Stavenga, D.G., et al., *Kingfisher feathers – colouration by pigments, spongy nanostructures and thin films.* The Journal of experimental biology, 2011. **214**(23): p. 3960.
10. Sun, J., B. Bhushan, and J. Tong, *Structural coloration in nature.* Rsc Advances, 2013. **3**(35): p. 14862-14889.
11. Kinoshita, S. and S. Yoshioka, *Structural colors in nature: the role of regularity and irregularity in the structure.* ChemPhysChem, 2005. **6**(8): p. 1442-1459.
12. Doucet, S.M. and M.G. Meadows, *Iridescence: a functional perspective.* Journal of The Royal Society Interface, 2009. **6**(Suppl 2): p. S115-S132.
13. Prum, R.O. *The anatomy and physics of avian structural colours*.
14. Joannopoulos, J.D., et al., *Photonic crystals: molding the flow of light*. 2011: Princeton university press.
15. Durrer, H., et al., *Biology of the integument, the skin of birds.* 1986.
16. Hill, G.E. and K.J. McGraw, *Bird coloration: mechanisms and measurements*. Vol. 1. 2006: Harvard University Press.
17. Yin, H., et al., *Iridescence in the neck feathers of domestic pigeons.* Physical Review E, 2006. **74**(5): p. 051916.
18. Eliason, C.M. and M.D. Shawkey, *A photonic heterostructure produces diverse iridescent colours in duck wing patches.* Journal of The Royal Society Interface, 2012. **9**(74): p. 2279-2289.
19. Greenewalt, C.H., W. Brandt, and D.D. Friel, *Iridescent colors of hummingbird feathers.* JOSA, 1960. **50**(10): p. 1005-1013.
20. Land, M., *The physics and biology of animal reflectors.* Progress in biophysics and molecular biology, 1972. **24**: p. 75-106.
21. Doucet, S.M., et al., *Iridescent plumage in satin bowerbirds: structure, mechanisms and nanostructural predictors of individual variation in colour.* Journal of Experimental Biology, 2006. **209**(2): p. 380-390.
22. Stavenga, D.G., et al., *Dramatic colour changes in a bird of paradise caused by uniquely structured breast feather barbules.* Proceedings of the Royal Society of London B: Biological Sciences, 2010: p. rspb20102293.
23. Durrer, H., *Schillerfarben der Vogelfeder als Evolutionsproblem: elektronenmikroskopische Untersuchung der Schillerstrukturen, ihrer Morphogenese*

und Analyse von Selektionsmechanismen (speziell dargelegt am Beispiel der Hühnervögel). 1977: Fretz.

24. Stavenga, D.G., et al., *High refractive index of melanin in shiny occipital feathers of a bird of paradise.* Light: Science &Amp; Applications, 2015. **4**: p. e243.
25. Sheppard, C.J.R., *Approximate calculation of the reflection coefficient from a stratified medium.* Pure and Applied Optics: Journal of the European Optical Society Part A, 1995. **4**(5): p. 665-669.
26. Eliason, C. and M. Shawkey, *Decreased hydrophobicity of iridescent feathers: a potential cost of shiny plumage.* The Journal of experimental biology, 2011. **214**(Pt 13): p. 2157.
27. Walther, B.A. and D.H. Clayton, *Elaborate ornaments are costly to maintain: evidence for high maintenance handicaps.* Behavioral Ecology, 2004. **16**(1): p. 89-95.
28. Liu, F., et al., *Structural color change in longhorn beetles Tmesisternus isabellae.* Optics express, 2009. **17**(18): p. 16183-16191.
29. Schmidt, W.F. and S. Jayasundera, *Microcrystalline avian keratin protein fibers*, in *Natural Fibers, Plastics and Composites*. 2004, Springer. p. 51-66.

Chapter 4: Fabrication of Silica Thin-Film Grating Structure

The research work in this chapter is also published in ACS Photonics. I am the main (first) author of this published paper. Further details and co-authors contributions are as following:

Ijaz Rashid, Haider Butt*, Ali K. Yetisen, Bruno Dlubak, James E. Davies, Pierre Seneor, Aymeric Vechhiola, Faycal Bouamrane, and Stephane Xavier. (2017*). "Wavelength-Selective Diffraction from Silica Thin-Film Gratings."* ACS Photonics 4(10): 2402-2409

Ijaz Rashid: is the main (first) author and he simulated the dimension refractive index dependent colour change in the grating structure based on thin film theory and diffraction. He modelled the experimental setups and conducted the experiments. He designed optical characterization setups and optical spectra setups. He has written the manuscript that was reviewed by mainly the lead supervisor Dr Haider Butt (*).

James E. Davies: contributed towards collection of spectra, microscopy imaging and documenting the procedures.

Bruno Dlubak and his team Pierre Seneor, Aymeric Vechhiola, Faycal Bouamrane, and Stephane Xavier: contributed towards the fabrication of grating structures.

Chapter 4: Fabrication of Silica Thin-Film Diffraction Grating Structure

4.1 Introduction

The word “diffraction” was first used by Italian scientist Francesco Maria Grimaldi who recorded the phenomenon in 1660. Later physicist Isaac newton used his work as an evidence that light is a wave and reached his more comprehensive theory of light. Newton rejected the wave theory of light. However, he mentioned its possible implication in explaining colours, Newton rings (or colour of thin plates) and colours of skylight reflected in soap bubbles with the assumption that light is a periodic wave with longest frequencies at red end of spectrum whereas highest at violet end. Robert Hooke in 1665 explained light as periodic sequence of pulses but he did not term them as a frequency for a particular colour whereas Huygens in 1678 termed light waves as individual pulses without any periodicity.

Thomas Young used Newton’s hint of colours and mentioned colours of thin plate as combined effect of front and back reflections which reinforce or cancel each other (interfere constructively or destructively) according to wavelength and thickness of the thin plate. Young also explained the colours of "striated surface" (i.e. gratings) as the wavelength-dependent reinforcement or cancellation of reflections from adjacent lines. He named this reinforcement or cancellation as interference effect. Thomas Young in 1801 performed a double-slit experiment, that showed light interference patterns, and established the wave theory of electromagnetic radiation. In 1818, Fresnel gave the first satisfactory explanation of diffraction by straight edges with wave based rectilinear propagation of light. Fresnel also provided equations with a quantitative analysis of light being reflected or transmitted at an interface of a medium surface using Snell’s Law and Young’s interference principle.

The wave theory of light was later described in detail by Maxwell's electromagnetic theory in 1860s. James Clerk Maxwell gave the proof of the electromagnetic nature of light in 1865. Lord Rayleigh in 1871 made two publications on the colour and polarization of skylight to quantify Tyndall's effect in water droplets in terms of the tiny particulates volumes and refractive indices confirming Snell's law, Fresnel equations and Maxwell's electromagnetic wave nature of light. In 1912, Lawrence Bragg's experiment showed X-ray diffraction from a crystal lattice confirming wave nature of X-rays, Rayleigh scattering and a secondary scattering (Huygens principle) but this secondary scattering was assumed to be negligible. This phenomenon of X-ray diffraction is named as Bragg diffraction in literature.

The principles of diffraction gratings were discovered by James Gregory in 17^{th} century with items such as bird feathers. The first diffraction grating was made around 1785 by David Rittenhouse, who strung hairs between two finely threaded screws and later by Joseph von Fraunhofer who used wire for diffraction grating in 1821. Diffraction grating structures have numerous applications in lasers, holography, optical data storage, light-trapping in solar cells, security holograms, and biosensors [1-5]. They have been utilized for precisely controlling optical beams (*e.g.*, splitting and steering) [6]. Light diffracted from nanostructures can create interference effects and diffract narrow-band light [7, 8]. SiO_2 (silica) and TiO_2 (titania) thin films have been investigated for optical applications due to their low optical propagation losses [8-10]. Conventional single material reflective gratings can be fabricated using micro processes such as preferential etching of monocrystalline Si [11]. While single material gratings, which displayed diffraction efficiencies up to 96%, have been developed,[12] investigation of the optical features of multi-material diffraction gratings has been limited.

In the present work, the optical effects produced by a one-dimensional (1D) reflective diffraction gratings based on silica thin films (Colour chart in **Figure S1**, **Appendix A**) fabricated on Si substrates were studied in detail. A comparison analysis was made between the

optical properties of silica thin film gratings and the optical effects produced with a grating made of Si on Si substrates. Colour-selective properties of thin films were combined with the diffraction effects using a 1D SiO_2 based colour-selective grating. Extensive theoretical work exists in the literature concerning thin films and diffraction grating separately. However, combining both concepts to study the distinct behaviour of diffraction grating formed from a single thin film has not been demonstrated. Computational modelling was used to determine grating parameters such as periodicity, thin film height, and refractive index. These analyses allowed rational design and optimization of the optical parameters and the device geometry. Two samples of diffraction grating with two separate dimensions i.e grating period and height were than fabricated for experimental purposes.

4.2 Methods

4.2.1 Simulations

COMSOL Multiphysics (V5.1), and MATLAB (MathWorks, V8.1) were used for simulations, data processing and plots respectively. COMSOL uses finite element method to perform calculations at each point described by the element's geometry and its size. It is a popular method for solving numerical problems. It uses Maxwell's electromagnetic wave equations with speed of light for calculations at each location dots and edges described by the 'element' geometry. Maxwell's equations are partial derivative equations that are used to describe light propagation at any arbitrary medium in which the light is travelling. The four basic Maxwell's equations are as follows:

Faraday's law, $\nabla \times \overline{E} = \frac{-\partial \overline{B}}{\partial t}$ ……(Eq. 4.1)

Ampere's law, $\nabla \times \overline{H} = \frac{\partial \overline{D}}{\partial t} + \bar{J}$ ……(Eq. 4.2)

Gauss's law for electricity, $\nabla \cdot \overline{D} = \rho$ ……(Eq. 4.3)

Gauss's law for magnetism, $\nabla \cdot \overline{B} = 0$ ……(Eq. 4.4)

where $\bar{D} = \varepsilon\bar{E}$, $\bar{B} = \mu\bar{H}$, $\varepsilon = \varepsilon_r \varepsilon_0$ and $\mu = \mu_r \mu_0$

$\bar{E}$ is Electric field vector (Volt/m), $\bar{H}$ is Magnetic field vector (Amp/m)

$\bar{D}$ is Electric flux density (Coul/m²), $\bar{B}$ is Magnetic flux density (Wb/m²)

$\bar{J}$ is Electric current density (Amp/m²), ρ is Electric charge density (Coul/m³)

ε_0 is the free-space permittivity (8.85x10^{-12} F/m), μ_0 is the free-space permeability (4π x10^{-7} H/m), ε_r is relative permittivity and μ_r is relative permeability

Apply curl operation ($\nabla\times$) on the both side of Faraday's law equation (4.1),

$$\nabla\times(\nabla\times\bar{E}) = \nabla\times\frac{-\partial\bar{B}}{\partial t}$$

$$\Rightarrow \nabla(\nabla.\bar{E}) - \nabla^2\bar{E} = -\mu_0\frac{\partial(\nabla\times\bar{H})}{\partial t} \qquad [\text{Since}, \nabla\times(\nabla\times\bar{E}) = \nabla(\nabla.\bar{E}) - \nabla^2\bar{E}\ ]$$

For free space, $\rho = \bar{J} = 0$, $\varepsilon_r = \mu_r = 1$, and $\nabla(\nabla.\bar{E}) = 0$

$$\Rightarrow \nabla^2\bar{E} = \mu_0\frac{\partial(\frac{\partial\bar{D}}{\partial t} + \bar{J})}{\partial t} \qquad [\text{From Ampere's law equation (4.2)}]$$

$$\Rightarrow \nabla^2\bar{E} = \mu_0\frac{\partial(\varepsilon_0\varepsilon_r\frac{\partial\bar{E}}{\partial t} + 0)}{\partial t}$$

$$\Rightarrow \nabla^2\bar{E} = \mu_0\varepsilon_0\frac{\partial\bar{E}^2}{\partial t^2} \qquad \text{where } [\, c = \frac{1}{\sqrt{\varepsilon_0\mu_0}} \cong 3\times10^8\, m/s^2\,]$$

$$\therefore \nabla^2\bar{E} = \frac{1}{c^2}\frac{\partial\bar{E}^2}{\partial t^2} \qquad \text{..... (Eq. 4.5)}$$

Similarly, from curl operation ($\nabla\times$) on the both side of equation (4.2) we can get,

$$\therefore \nabla^2\bar{H} = \frac{1}{c^2}\frac{\partial\bar{H}^2}{\partial t^2} \qquad \text{..... (Eq. 4.6)}$$

Equations (4.5) and (4.6) are known as wave-equations travelling at the speed of light, c (3.0 x 10^8 m/s^2).

The ‘element’ in finite element method is described as a line segment for 1D, Triangle and Square for 2D and Tetrahedron, Prism and Hexahedron for 3D simulations respectively.

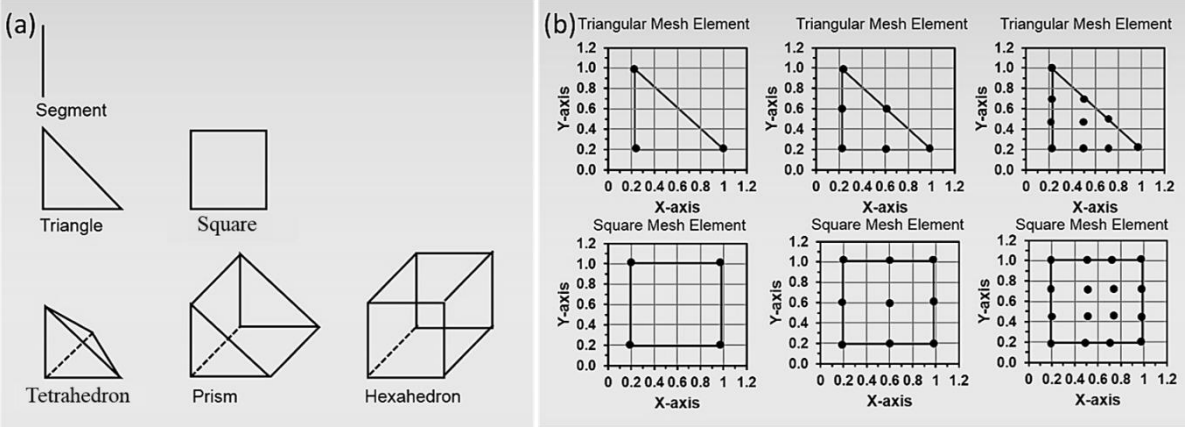

Figure 4.1. Schematics of finite element geometry.

The accuracy of results is dependent on the mesh element size. The smaller the mesh element size, the greater is the accuracy of results as more points are available for calculations to be performed. However, the processing time will become larger and more memory space will be required as well. Mesh analysis was performed for an element size ranging from 50 nm to a size of 200 nm before selecting the final mesh element size. This process was adopted in order to validate the accuracy of the mesh size chosen. Reflectance was measured at zero degrees for two different samples with a varied mesh size as shown in **Figure 4.2**. Both samples were observed to be stable below 60 nm. A maximum mesh element size of 50 nm was chosen to perform all simulations. A minimum mesh element size of 9 nm was chosen for near field region and inside the structure to have more points for calculations in this region. The power outflow change between adjacent points is higher in near field regions whereas this change is less significant for this mesh size in far field region. Therefore, a maximum mesh element size was selected for far field region.

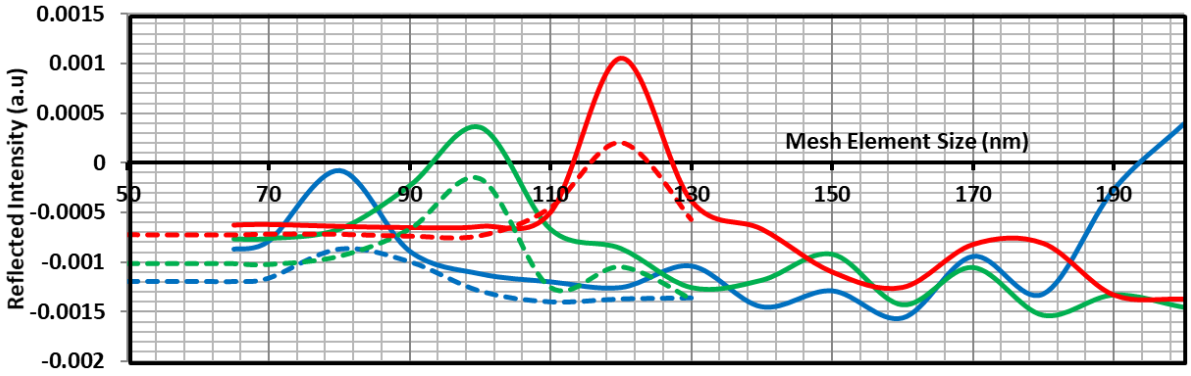

Figure 4.2. Mesh analysis on finite element size

MATLAB code for thin film with equations and COMSOL simulation procedure are provided in **Appendix B and C** respectively.

4.2.2 Optical characterization

The spectrophotometer (Ocean Optics 2000) with an optical resolution of ~0.1-100 nm FWHM was used to measure optical intensity with an integration time of 1 sec to obtain the maximum peak intensity. Optical setup for the characterization of the diffraction grating was constructed using a holder for laser pointer, a sample holder and a semi-transparent semi hemispherical screen to display the phenomenon. Diffraction spots were recorded in reflection mode by shining red, green and blue laser light perpendicular to the surface grating. **Figure 4.3a** and **b** demonstrate the setup schematics and images recorded respectively. Diffraction pattern were also obtained by illuminating the grating with a broadband. Angle-resolved measurements were also recorded by stepwise rotating the receiving fibre end while keeping the light source at the same fixed point. Reflection intensity distribution pattern in response to broadband light was captured in reflection mode.

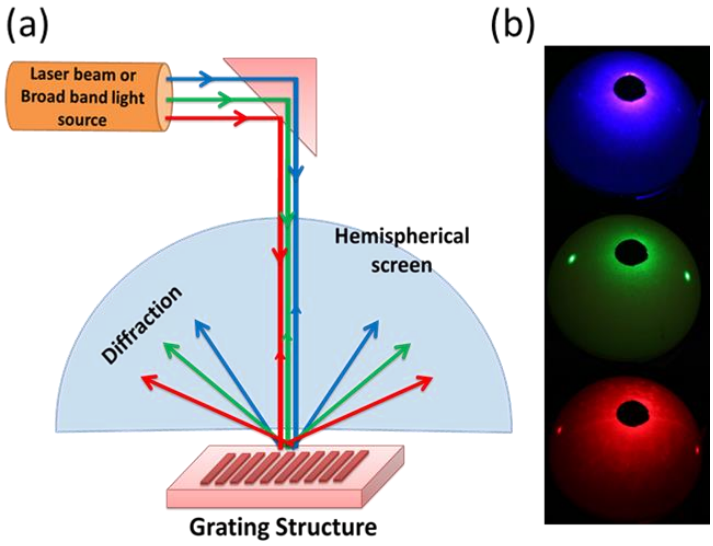

Figure 4.3. (a) Optical Characterization setup and Simulation schematics in reflection mode **(b)** Practical images recorded for blue, green and red laser beams in lab.

4.2.3 Fabrication

Traditional approach was adopted to fabricate the grating. A Si wafer with thermally grown 400 nm (and later 500 nm) thick SiO_2 layer was used. The wafer was spin coated with UVIII resist. This resist allows both optical deep-UV lithography and electron beam lithography. Using a nano-beam, 400 nm (or 500 nm) strips were patterned over the substrate. The resist was developed with CD-26 solution to expose the SiO_2 surfaces which are to be etched. A CHF_3 reactive ion beam etching step is carried out to remove the SiO_2 down to the Si wafer (as checked by atomic force microscopy (AFM) using Alicona G5 Infinite Focus system), while leaving the SiO_2 where it is protected by UVIII. After cleaning the structure in acetone to remove the resist, this process created desired diffraction grating made of a SiO_2 line array (millimetre long) over the Si substrate. **Figure 4.9a-e** demonstrates the optical, AFM and Scanning Electron Microscope (SEM) images of the fabricated gratings, respectively. AFM analysis in **Figure 4.10e** showed sharp edge profiles of the fabricated SiO_2 thin film gratings.

This work was performed with the help of Bruno Dlubak. He is a research associate at Université Paris-Saclay, Palaiseau, France.

4.3 Results and Discussion

Finite element method was used to simulate the reflection and diffraction properties of SiO2 based thin film gratings. **Figure 4.4a** shows the schematics of 400 and 500 nm thick SiO2 thin film parallel gratings on Si substrate. **Figure 4.4b** shows a generic 2D computational geometry used to analyse the diffraction from these thin film gratings. The incident light was normal to the top of the SiO_2 thin film gratings. It was hypothesized that as the SiO_2 gratings became thicker, their diffraction spectrum red shifted according to the thin film theory [13, 14]. **Figure 4.4c-d** demonstrates the computed reflected light intensity and the corresponding spectra for the 400 and 500 nm thick gratings in response to the 445 nm (blue), 532 nm (green) and 650 nm (red) incident light waves.

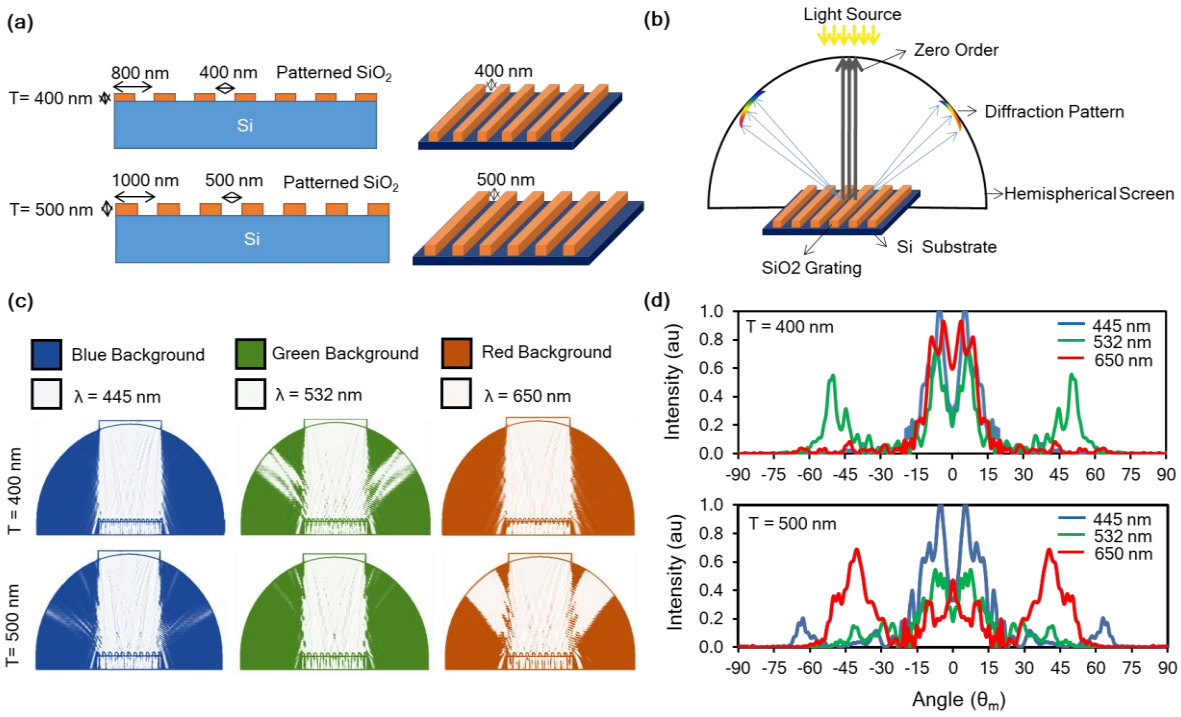

Figure 4.4. Simulations of 1D SiO_2 diffraction gratings. **(a)** SiO_2-based thin film gratings on Si, with 400 and 500 nm thicknesses (T). **(b)** Computational geometry for simulating optical

diffraction. **(c)** Diffraction intensity analysis for 400 and 500 nm thick gratings in response to wavelengths (λ) 445 nm (blue), 532 nm (green) and 650 nm (red). **(d)** Diffraction patterns for 400 and 500 nm thick gratings showing high-intensity peaks for green and red light wavelengths, respectively.

4.3.1 Optical Modelling

The far-field angular intensity profile from -90° to 90° was extracted from the computational domain to determine the zero, first and second order diffraction intensities for each grating (**Figure 4.4d**). For higher diffraction orders, the angles of the maxima peaks and intensity profiles were studied; and for the zero order, diffraction intensities were analysed. The theoretical diffraction angles (θ_m) displayed in **Figure 4.4d** were also calculated using the following grating equation [4]:

$$d(\sin\alpha+\sin\beta) = m\lambda \qquad \text{……..……(Eq. 4.7)}$$

where α is the angle of incidence and $\beta(\theta_m)$ is the angle of reflected or diffracted light from the normal, d is the grating period, m is the diffraction order, and λ is the diffraction wavelength. For the case of normal incidence, α=0. Thus, the equation simplifies to

$$d\sin\theta_m = m\lambda \qquad \text{....……..…… (Eq. 4.8)}$$

where θ_m is the angle of diffracted light from the normal, d is the grating period, m is the diffraction order (zero,1st, 2^{nd} ,3^{rd} ...), and λ is the diffraction wavelength.

The 400 nm thick grating sample showed a diffraction resonance for green light (**Figure 4.4c-d**). While the zero order consisted of high intensities of blue and green colour, the first order diffraction was dominated by the green light. The thicker thin film grating (500 nm) preferentially diffracted red colour as compared to the blue and green light. A pronounce red colour is observed in the first order diffraction spectrum. The peaks observed were broad over the angles. This effect is due to the distance of the receiving boundary from the grating sample which was kept close in the near field to decrease the overall size of the geometry for fine

simulation meshing. However, this broadness effect will not be observed at large distances in the far-field region. These results show that the thicknesses of thin films were vital in controlling the diffraction wavelengths and by controlling the thicknesses wavelength selective diffractive structures can be achieved.

Further simulations were performed to analyse each of the thin-film grating parameters i.e. periodicity, thin film height, refractive index and their effects on the reflection and diffraction properties. **Figure 4.5** displays the zero, first and second order intensity plots for the simulated SiO2 thin-film grating as a function of grating height (thin-film thickness) and period. **Figure 4.5a-c** show the zero order reflected intensity plots against the grating thicknesses, with each line showing the trend for a different grating periodicity. Similarly, **Figure 4.5d-f** and **4.3g-h** show the first and second order diffraction plots, respectively. It can be observed that each trend line on the plot shows a sinusoidal trend resonating at respective thicknesses, similar to that shown by thin films in reflection mode. In **Figure 4.5a**, it can be seen that for blue incident light (445 nm) almost all gratings are showing highest zero order reflection at thicknesses in the range of 450-500 nm. The level of intensity is observed to be decreasing with an increase in the period as this increases the diffraction of light to first and second orders instead of light being reflected back to zero order. Similar effect can be seen in **Figure 4.5b** and **4.3c** (plots for green and red incident light) where the resonating thicknesses are around 400 and 470 nm, respectively. First order diffraction plots in **Figure 4.5d-f** also show the thin film resonance effect at thicknesses around 345, 400 and 500 nm for blue, green and red wavelengths, respectively. The peaks observed in first (**Figure 4.5d-f**) and second (**Figure 4.5g-h**) orders are a result of both thin film and diffraction effect. Light diffraction is usually dependent on the ratio between the height (thickness) and period of the grating for a particular wavelength whereas thin film effect is dependent on thickness (height) and the change in refractive index with respect to the substrate. The grating heights at which the peak intensity peaks occurred for

the first order were analogous to those of the zero order. This behaviour can be observed in **Figure 4.5a** in which the gratings with high zero order blue reflection (thicknesses 450-550 nm) have low blue diffraction in first order (**Figure 4.5d**) whereas the result is opposite for the thicknesses 300-400 nm which preferentially diffract blue colour in the first order and low intensity peaks for the zero order. The zero order reflection is also periodicity dependent, as the grating with lowest period (700 nm) displays the highest zero order intensity peaks.

Another effect can also be analysed by comparing green (532 nm) wavelength plots (**Figure 4.5b and 4.3e**) where zero order peak is observed at thickness of 400 nm for a smaller period of 700 nm, while first order diffraction peak for the same thickness occurs at a larger period of 900 nm. Same behaviour is observed for red (650 nm) wavelength plots in **Figure 4.5c** and **4.3f** where resonance occurs at a thickness of 500 nm for both orders but at periodicities of 700 and 1064 nm, respectively. To summarize, it is observed that the grating periods and the behaviours of the peak maxima are correlated. As the period approached the same dimension as the examined incident wavelength, the original peak diverged into first and second order diffraction peaks showing the diffraction effect. This behaviour is valid for the zero, first and second order diffraction plots for the SiO_2 grating (**Figure 4.5a-h**). The phenomenon of peak splitting in periodic gratings has previously been observed for Bragg diffraction peaks due to the interference of asymmetric diffraction orders [15, 16].

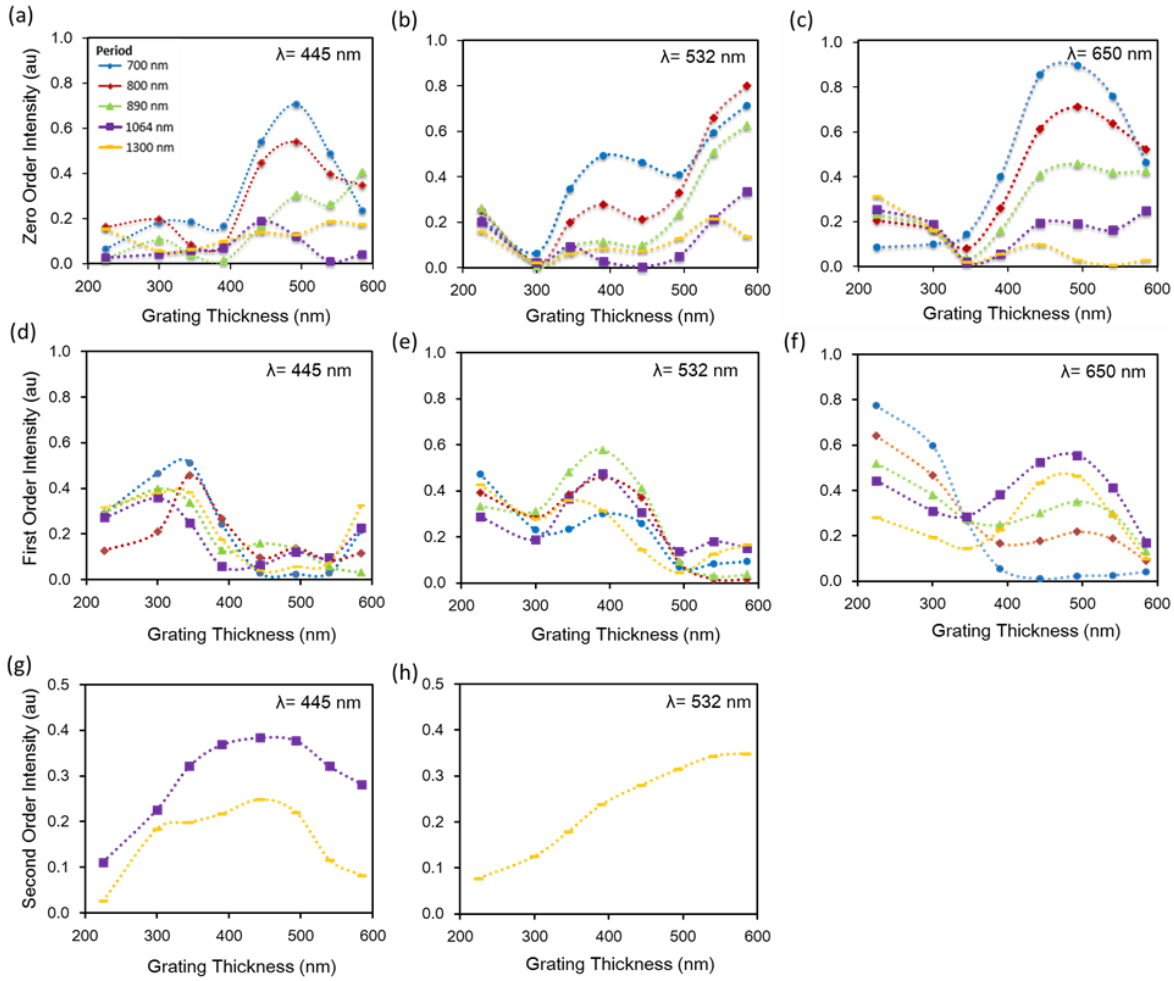

Figure 4.5. Simulations of the SiO_2 grating. **(a-c)** zero, **(d-f)** first and **(g-h)** second order peak intensity plots with incident wavelengths of 445 nm, 532 nm, and 650 nm.

Although diffraction was primarily investigated, zero and higher orders were analysed showing specular reflection from the grating but it was inherent to study the thin film thickness effect as the film thickness being the integral part of the grating feature had a major role in colour selection of the diffracted light. Colour charts for SiO_2 thin films are widely used (**Appendix A, Figure S1**) for thickness based colour selection but to directly match the grating thickness with the corresponding thin-film thickness, the wavelengths being tested (445, 532, and 650 nm) have been simulated in MATLAB (**Figure 4.7**). An approximation made by C J R Sheppard for calculation of reflection coefficient 'R' for three material refractive indices ($n_1 \leq n_2 \leq n_3$) was analysed to measure reflectance [17]. Fresnel equations were used to

calculate reflectance from top and bottom interfaces of the thin film layer and an approximation expression for calculation of reflection coefficient 'R' [18].

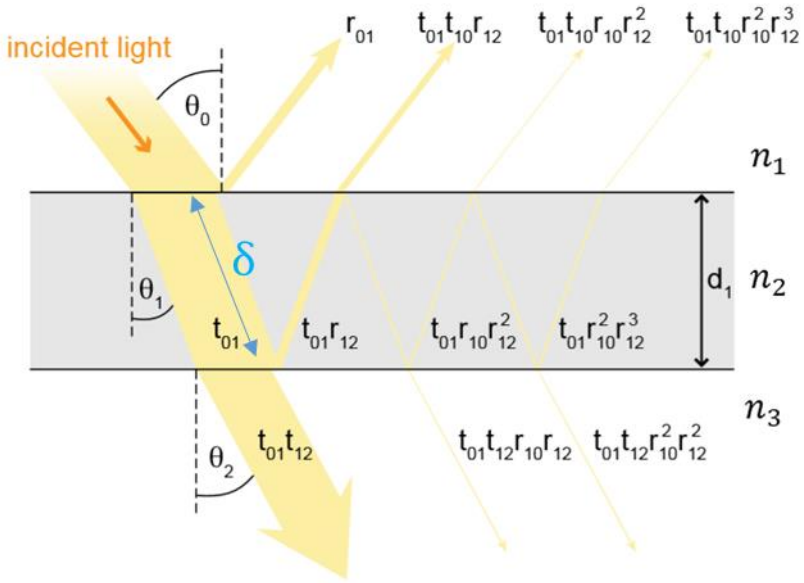

Figure 4.6. Schematic diagram of thin film reflectivity showing reflection and transmission coefficients [18].

The extra length of optical path travelled by the light wave (δ) within the thin layer dictates the shift in phase for interference to happen constructively or destructively. Expression for extra path length travelled is

$$\delta = \frac{2\pi}{\lambda} * n_2 * d_1 \cos\theta_1 \quad \text{.....(Eq. 4.9)}$$

where d_1 is the thickness of the thin film.

As in our case the incident light is at normal incidence where $\theta_0 = 0$, Thus, the expression for calculation of extra path length travelled by light simplifies to

$$\delta = \frac{2\pi}{\lambda} * n_2 * d_1 \quad \text{..... (Eq. 4.10)}$$

Fresnel reflection equation at interface 1 between air (n_1) and SiO_2 (n_2) is simplified to

$$r_{01} = \frac{n_1 - n_2}{n_1 + n_2} \quad \text{..... (Eq. 4.11)}$$

Fresnel reflection equation at interface 2 between SiO_2 (n_2) and Silicon (n_3) simplifies to

$$r_{12} = \frac{n_2 - n_3}{n_2 + n_3} \quad \text{.....(Eq. 4.12)}$$

By summation of all reflection amplitude beams and taking into account their phase shifts, the complex reflected amplitude A_r amounts to

$$A_r = r_{01} + t_{01}t_{10}r_{12}e^{-2i\delta}\sum_{n=0}^{\infty}(-1)^n(r_{01}r_{12})^n e^{-2in\delta}$$

$$A_r = r_{01} + \frac{t_{01}t_{10}r_{12}e^{-2i\delta}}{1 + r_{01}r_{12}e^{-2i\delta}} \quad \text{..... (Eq. 4.13)}$$

Applying the conservation of energy relation *T = 1- R* and Fresnel reflection and transmission coefficients of each of the two interfaces, it follows that $r_{10} = -r_{01}$

$$t_{01}t_{10} = (1 - r_{01})(1 - r_{10}) = 1 - r^2{}_{01}$$

$$A_r = \frac{r_{01} + r_{12}e^{-2i\delta}}{1 + r_{01}r_{12}e^{-2i\delta}} \quad \text{.....} \quad \text{(Eq. 4.14)}$$

The total reflection coefficient 'R' is $R = A_r . A_r{}^*$ ..... (Eq. 4.15)

$$R = \frac{r^2{}_{01} + 2r_{01}r_{12}cos2\delta + r^2{}_{12}}{1 + +2r_{01}r_{12}cos2\delta + r^2{}_{01}r^2{}_{12}} \quad \text{.....} \quad \text{(Eq. 4.16)}$$

Figure 4.7a displays the relative intensity of reflected polychromatic light for seven different thin-films of specific thickness and known reflective resonant colour. MATLAB code for the simulation is provided in **Appendix B**. The zero order peak intensity plots for the SiO_2 thin-film gratings in **Figure 4.5a-c** displayed a sinusoidal wave pattern which is analogous to the thin-film simulation plot in **Figure 4.7b**. For each wavelength simulated with the SiO_2 thin-

film grating, the locations of the intensity peaks and troughs were consistent with the reflection spectra for SiO_2 uniform thin-films. For example, in **Figure 4.7b**, the observable thin-film interference occurred between 400 nm and 500 nm for the blue wavelength (445 nm) which is in accordance with the **Figure 4.5a** where the resonating thickness existed between 400 nm and 500 nm for the same wavelength.

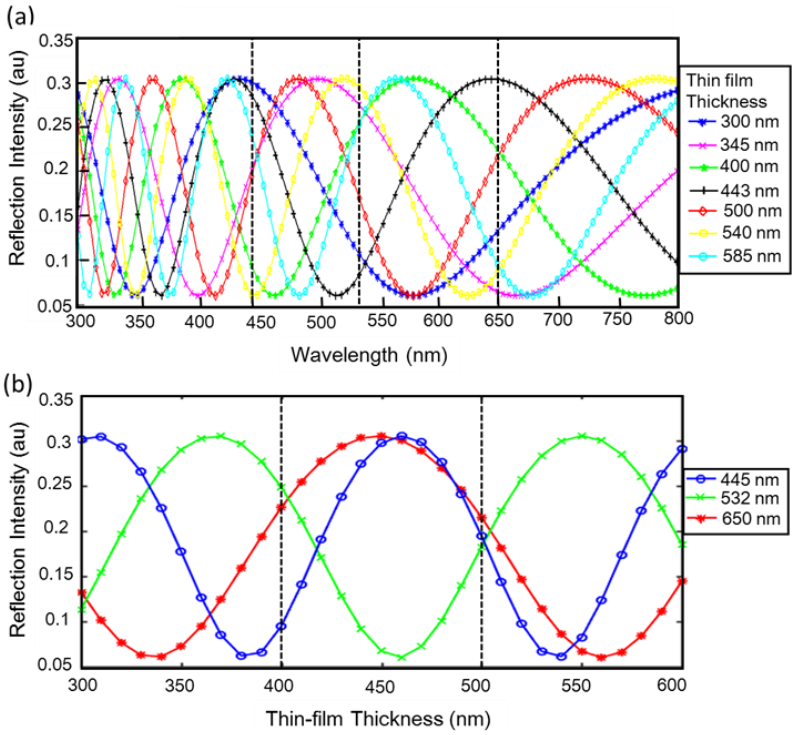

Figure 4.7. Reflection intensities of thin films as a function of **(a)** SiO_2 layer thickness, **(b)** film thickness for 445, 532 and 650 nm wavelengths.

This was reinforced by the results in **Figure 4.8** where the simulations were done purely on Si based gratings on a Si substrate. There is no change in refractive index of the grating and the substrate. The results displayed complex behaviour (**Figure 4.8**) showing no sign of thin film sinusoidal effect in comparison to the SiO_2 grating results in **Figure 4.5**. Zero order intensity plots (**Figure 4.8a-c**) display a complex behaviour for blue, green and red wavelengths as compared to the sinusoidal zero orders seen for the SiO_2 gratings in **Figure 4.5a-c** which were due to the difference in refractive index; and therefore thin-film interference was present within

the SiO_2 features. Similarly, the first order Si grating plots in **Figure 4.8d-f** display peaks which were not correlated with Si layer thickness as compared to the SiO_2 grating plots in **Figure 4.5d-f**. Si grating plots demonstrate complex behaviour for all the orders where peak patterns exist at different locations for each grating period line (**Figure 4.8**) whereas SiO_2 peak intensity plots in **Figure 4.5** follow consistent pattern, with peaks and troughs were predominantly at the same location showing sinusoidal behaviour for each grating period. The grating heights at which the peak intensity peaks occurred for the first order diffraction were analogous to those of the zero order (**Figure 4.5**) while no such behaviour is observed in **Figure 4.8**. For example, in zero order (**Figure 4.8a**), high intensity peaks were visualised around 300 nm thickness for 700 and 900 nm periods whereas the peaks appeared at thickness of 450 nm for 800 nm, 1064 nm and 1300 nm periods for the same blue wavelength. Similarly, in first order diffraction (**Figure 4.8d**), high intensity peaks can be seen around 305, 320, 325, 345 and 450 nm thicknesses for the grating period of 800, 1300, 1064, 900 and 700 nm respectively for blue wavelength.

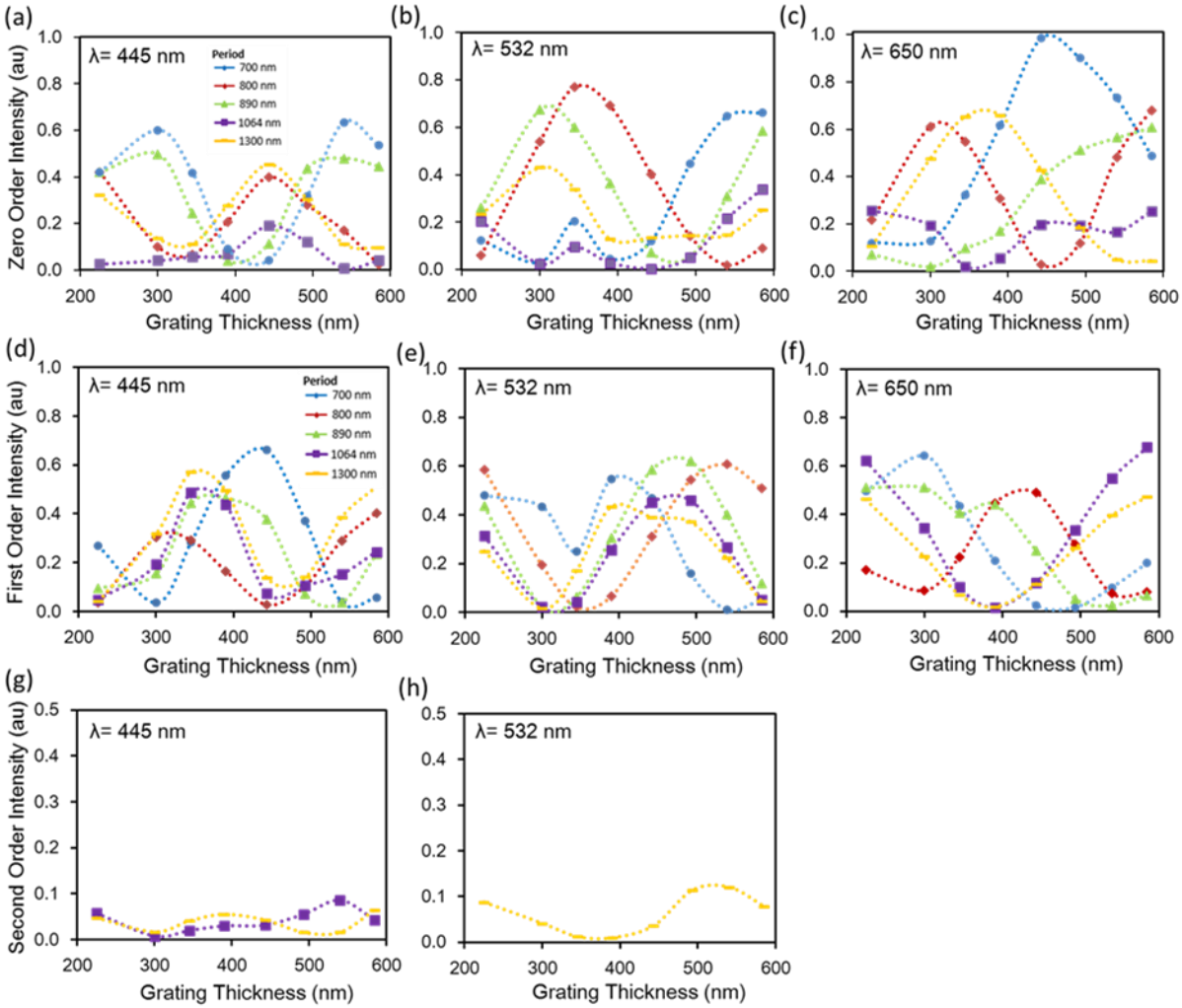

Figure 4.8. Simulations of Si gratings. **(a-c)** Zero, **(d-f)** first and **(g-h)** second-order diffraction peak intensity plots with incident wavelengths of 445 nm, 532 nm, and 650 nm.

A SiO_2-Si grating has the same diffraction efficiency as that of a grating formed in Si-Si material, but has the advantage of having an ordered relationship between the grating feature dimensions and the intensity of reflected and diffracted wavelengths due to thin-film interference. Based on the simulation results, grating thicknesses of 400 and 500 nm with half periods of 400 and 500 nm were chosen to be fabricated. According to the results in **Figure 4.5e-f**, 400 nm grating should show the highest first order diffraction efficiency for green light whereas 500 nm grating should show the highest diffraction efficiency for red light.

4.3.2 Optical Characterisation

Figure 4.9f illustrates the experimental setup for the optical characterization of the grating. The diffraction pattern of the grating is shown in **Figure 4.9g** and **4.9h** using monochromatic and broadband incident beams respectively. Diffracted spots in the reflection mode were visualized in backward direction by normal incident red laser light (**Figure 4.9g**). A well-ordered rainbow was observed by using broadband light, where the red diffraction was at a higher angle and blue was at a lower angle (**Figure 4.9h**). For monochromatic laser incidence, the diffraction patterns were concentrated spots instead of broadband ribbons (**Figure 4.9g**).

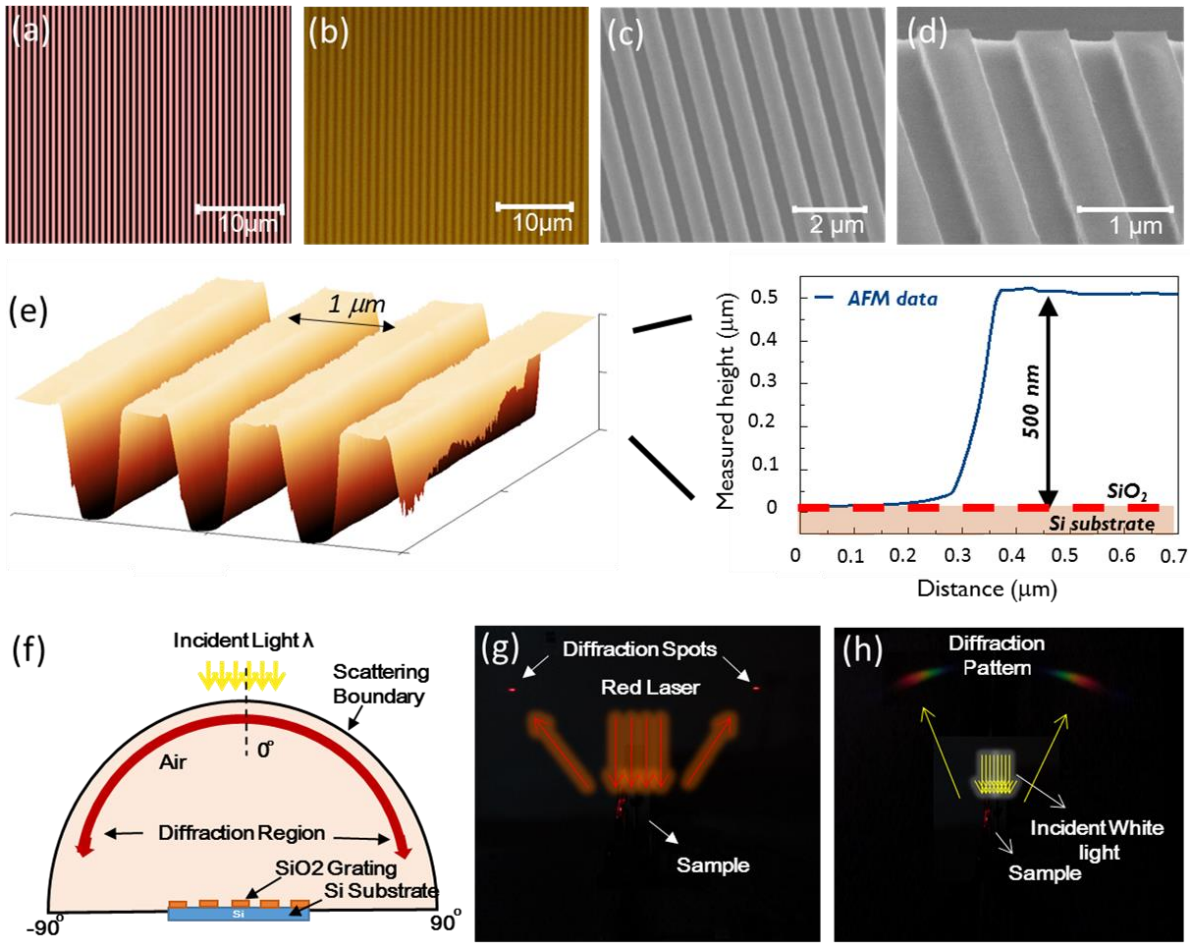

Figure 4.9. Optical characterization on SiO_2 gratings on a Si substrate. **(a)** Computer-Aided Design (CAD) mask of a grating having a periodicity of 500 nm. **(b)** Optical image of a 400

nm grating after e-beam lithography, etching and resist cleaning. **(c-d)** SEM image of a 500 nm grating. **(e)** AFM image of a 500 nm grating. **(f)** Optical setup for the characterization of the diffraction grating. **(g)** Diffraction spots in reflection mode by shining red laser light perpendicular to the surface grating. **(h)** Diffraction pattern obtained by illuminating the grating with a broadband light in a semi-transparent hemispherical screen.

The diffraction angles and efficiencies of the gratings for different monochromatic laser sources were studied by angle-resolved measurements. While standard wavelengths of 445 nm, 532 nm and 650 nm were used in the simulated model, available laser beam wavelengths for the diffraction measurements were 403 nm, 532 nm and 638 nm. The grating sample was illuminated normally on a rotation stage. Light intensity measurements were collected using a spectrophotometer at different angles with an angular resolution of 0.5°. **Figure 4.10a-d** show the diffracted light intensity distribution in zero and first order diffraction for the three monochromatic light wavelengths. It can be observed that blue and red wavelengths returned almost undiffracted to zero order for 400 nm grating **(Figure 4.10a**), whereas for 500 nm grating blue and green wavelengths dominate the zero order (**Figure 4.10b**). High diffraction of green light is observed in the first order diffraction (**Figure 4.10c**) for 400 nm grating, whereas red light is highly diffracted by the 500 nm grating (**Figure 4.10d**). The diffraction spots were visualized in the range of -90° to +90° with blue diffracted at lower angles compared to red. The diffraction angles for blue, green and red light were measured to be 26°, 36° and 44° for the 400 nm grating (**Figure 4.10c**); and 21°, 27° and 34° for the 500 nm grating, respectively (**Figure 4.10d**). The variations in the diffraction angles in **Figure 4.10c-d** are due to the difference in period and thickness of both grating samples. The difference between the simulated theoretical solution and the experimental results can be attributed to the thin film effect where the backscattered light constructively and destructively interferes to influence the location of diffraction spots. The diffraction efficiency for the incident blue, green and red lasers

were experimentally measured to be 10% (blue), 56% (green) and 14% (red) for the 400 nm grating; and 9% (blue), 16% (green) and 52% (red) for the 500 nm grating, respectively. **Figure 4.10e-f** shows the diffracted light intensity distribution for the first order diffraction in response to white broadband light. The broadband peaks (20°-60°) were observed symmetrically from both sides of a central specular reflection spot (zero order), where the diffraction pattern was in agreement with **Figure 4.9h**. However, the diffraction peak angles observed were lower than the grating equation. This effect of reduced angles is due to the thin film effect where light undergoes refraction and reflection. A precise description of the angular position of the resolved peaks was done by using Bragg's law with effective refractive index.

$$\lambda = \frac{d}{m} n_{eff} \sin(\theta) \qquad \text{.....(Eq. 4.17)}$$

It takes into account the reduced angle with respect to the normal at which light travels in the grating structure. Where n_{eff} is the average effective refractive index of the grating structure. For silica grating in air, it can be calculated as:

$$n_{eff} = n_{silica} f_{silica} + n_{air} f_{air} \qquad \text{..... (Eq. 4.18)}$$

Where n_{silica} = 1.45, n_{air} = 1 , f_{silica} and f_{air} are the volume fractions occupied by silica and air in the structure (generally 50% for a grating structure with equal dimensions). Therefore, the theoretical value of $n_{eff} = 1.225$. **Figure 4.10g-h** show the simulated plots for the above Bragg's law equation using MATLAB to see the behaviour of reduced diffraction angles with respect to change in refractive index for the two grating samples (400 and 500 nm). MATLAB code is provided in the **Appendix B**. The measured values tend to be more near to the line representing n_{eff} = 1.15 which gives an error of 6% based on the theoretical value. This error is probably due to setup calibration. The practically measured values show a good agreement with the theoretical plots of reduced diffraction angle lines with respect to change in effective refractive index.

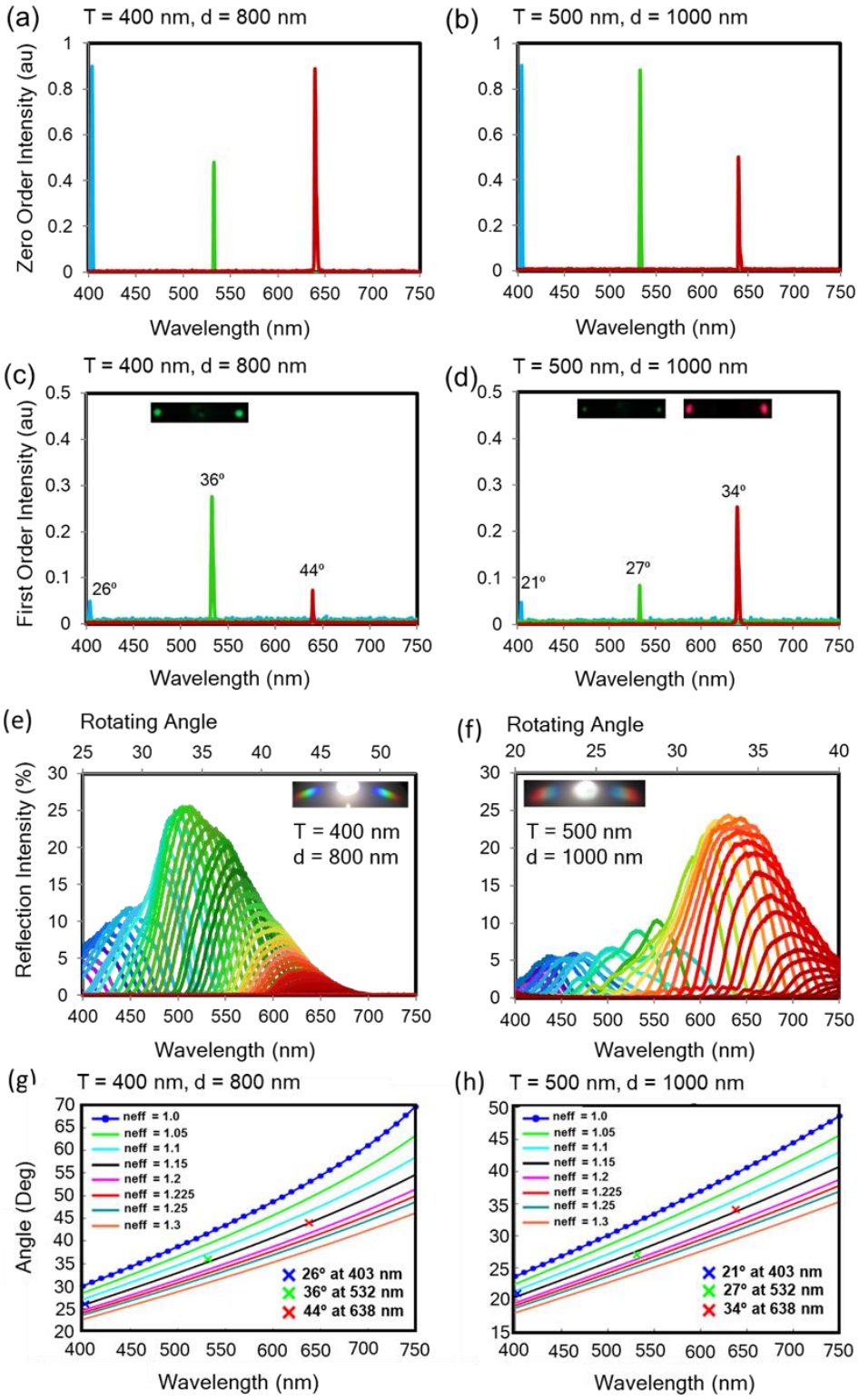

Figure 4.10. Optical characterization of the SiO_2 gratings. Zero order intensity distribution in response to 403, 532, 638 nm wavelengths in reflection mode for **(a)** 400 nm **(b)** 500 nm thicknesses. **(c)** First order diffracted optical intensity distribution for 400 nm, and **(d)** 500 nm

grating. **(e-f)** Angle-resolved measurements of SiO_2 gratings. Specular first order reflection intensity distribution pattern in response to broadband light in reflection mode corresponding to rotational angles from 20° to 60° for 400 nm and 500 nm thick gratings. **(g-h)** Reduced diffraction angle plots with change in effective refractive index for 400 and 500 nm grating samples. Grating periods in **(a,c,e,g)** and **(b,d,f,h)** were 400 and 500 nm, respectively.

4.3.3 Coherent and incoherent scattering

Light in a conventional reflection grating is diffracted from the top surface; however, in a thin film grating, the light is both diffracted (diffraction grating) and backscattered (thin film effect). The backscattered light undergoes coherent constructive and destructive interferences which has an overall effect on the reflection spectrum. The thin film grating of 400 nm periodicity and thickness displayed enhanced green spectrum in first order, ranging from 492-567 nm (**Figure 4.10e**). This is in agreement with the simulation results in **Figure 4.4d** and **Figure 4.5e**. Similarly, as expected the 500 nm thin film grating displayed enhanced first order diffraction peaks in the red regime ranging from 595-725 nm (**Figure 4.10f**), which is in close proximity to the results in **Figure 4.4d** and **Figure 4.5f**. These results were also in close agreement with the simulated results shown in **Figure 4.5d-f** and the thin film resonance plots shown in **Figure 4.7b**. Thus, the utilization of our simulation model allows creating gratings with predictable optical diffraction properties. The result supports the hypothesis that by optimizing the thin film grating features such as thickness, period, and refractive index, the optical properties can be tailored, especially to achieve colour selective diffraction in first order.

4.4 Summary

SiO_2 based thin-film gratings obeyed the grating equation, displaying intensity maxima peaks in consistent locations even if the thin-film had variation in feature height. Due

to thin-film interference, change in grating thickness resulted in the intensity of wavelengths regardless of the grating periodicity. However, the absolute value of diffraction intensity is dictated by the grating periodicity. The observed colour of the grating was controlled separately from the diffraction maxima locations. The zero and first orders primarily displayed the same wavelengths, as the intensity of the zero order increased with increasing grating height, the first order diffraction intensity decreased. These discernible investigations have led to a study of a new type of hierarchical grating that displayed optical properties which could be controlled independently. A grating with unique properties was created with predictable behaviour such as desired optical bandwidth dictated by the grating features. This hierarchical grating can be integrated in hydrogel based photonic bandgap sensors through nanoimprint lithography techniques to enhance fast and facile fabrication with simple detection methods using change in physiological conditions of the photonic bandgap structures based hydrogel. It is also anticipated that the designed grating will find applications in spectroscopy, bio sensing, smart sensors and security applications.

Bibliography

1. Gaylord, T.K. and M. Moharam, *Analysis and applications of optical diffraction by gratings.* Proceedings of the IEEE, 1985. **73**(5): p. 894-937.
2. Vasconcellos, F.d.C., et al., *Printable surface holograms via laser ablation.* ACS Photonics, 2014. **1**(6): p. 489-495.
3. Yetisen, A.K., et al., *Light-Directed Writing of Chemically Tunable Narrow-Band Holographic Sensors.* Advanced Optical Materials, 2014. **2**(3): p. 250-254.
4. Palmer, C.A. and E.G. Loewen, *Diffraction grating handbook*. 2000: Richardson grating laboratory.
5. Montelongo, Y., et al., *Plasmonic nanoparticle scattering for color holograms.* Proceedings of the National Academy of Sciences, 2014. **111**(35): p. 12679.

6. Won, K., et al., *Electrically Switchable Diffraction Grating Using a Hybrid Liquid Crystal and Carbon Nanotube-Based Nanophotonic Device.* Advanced Optical Materials, 2013. **1**(5): p. 368-373.
7. Butt, H., et al., *Morpho Butterfly-Inspired Nanostructures.* Advanced Optical Materials, 2016. **4**(4): p. 497-504.
8. Du, X.M. and R.M. Almeida, *Sintering kinetics of silica-titania sol-gel films on silicon wafers.* Journal of materials research, 1996. **11**(02): p. 353-357.
9. Brusatin, G., et al., *Microstructural and optical properties of sol-gel silica-titania waveguides.* Journal of non-crystalline solids, 1997. **220**(2): p. 202-209.
10. Que, W., et al., *Microstructural and spectroscopic studies of sol-gel derived silica-titania waveguides.* Journal of sol-gel science and technology, 2000. **18**(1): p. 77-83.
11. Tsang, W.T. and S. Wang, *Preferentially etched diffraction gratings in silicon.* Journal of Applied Physics, 1975. **46**(5): p. 2163-2166.
12. Perry, M., et al., *High-efficiency multilayer dielectric diffraction gratings: erratum.* Optics letters, 1995. **20**(13): p. 1513.
13. Heavens, O.S., *Optical properties of thin solid films*. 1991: Courier Corporation.
14. Pleil, M.W., *Plug and Play Microsystems (MEMS) Technology into an Engineering and Technology Program.*
15. Tarnowski, K. and W. Urbanczyk, *Origin of Bragg reflection peaks splitting in gratings fabricated using a multiple order phase mask.* Optics express, 2013. **21**(19): p. 21800-21810.
16. Guemes, J. and J. Menendez, *Response of Bragg grating fiber-optic sensors when embedded in composite laminates.* Composites science and technology, 2002. **62**(7): p. 959-966.
17. Sheppard, C.J.R., *Approximate calculation of the reflection coefficient from a stratified medium.* Pure and Applied Optics: Journal of the European Optical Society Part A, 1995. **4**(5): p. 665-669.
18. Gibbons, N., et al. *Stretch-tuneable Dielectric Mirrors and Microcavities*. in *Conference on Lasers and Electro-Optics 2010*. 2010. San Jose, California: Optical Society of America.

Chapter 5: Fabrication of Nanostructures on Titanium surfaces

Research work in this chapter is also submitted in RCS Advances for review. I am the main (first) author of this paper. Further details and co-authors contributions are as following:

Ijaz Rashid, Muhammad Umair Hassan, Affar S. Karimullah, Badar Alqattan and Haider Butt. *"Nanopatterned Surfaces for Modulating Hydrophobic Properties of Titanium."*

Ijaz Rashid: is the main (first) author. He modelled the experimental setups and conducted the experiments. He designed optical characterization setups and optical spectra setups. He has written the manuscript that was mainly reviewed by Dr Muhammad Umair Hassan and the lead supervisor Dr Haider Butt (*).

Badar Alqattan: contributed towards fabrication of nanostructures using DLIP method.

Affar S. Karimullah: contributed towards titanium thin film deposition.

Chapter 5: Fabrication of Nanostructures on Titanium surfaces

5.1 Introduction

The interaction of a liquid droplet with nano-patterned surfaces has been an interesting topic for the last few years [1-6]. Previous studies inspired from surfaces existing in nature such as rose petals [7-9], butterfly wings [10, 11] and sacred lotus leaves [12, 13]. However, previously adopted methods for fabrication such as stochastic patterning and roughness of surfaces [14-16], electrochemical etching [17-19], cold nanoparticle compaction [20], soft lithography [21, 22], photolithography [23], nanoimprint lithography [24], focused ion beam (FIB) and electron beam lithography (EBL) [25], colloidal lithography [26] , sol-gel [27-30] etc. have limitations in size, shape and efficiency; are expensive, time consuming, complex in nature and may have the long term effect of toxicity due to the use of dangerous chemicals on the surface of the material. Nanoscale patterning can be a powerful tool for modulating hydrophobicity for specific devices [31-35]. Patterning has previously been performed on surfaces using laser engraving methods with controlling parameters such as laser energy, scanning speed and distance of the sample from the focus point of the beam but due to the large size of the beam spot, the structures fabricated were in microscale [28, 36-39]. In order to pattern surfaces in the nanoscale range, a direct laser interference patterning technique is adopted in this study. Through direct laser writing by interference, material surfaces can be patterned in nanoscale within seconds of time with more controllable parameters in terms of shape, size and roughness of nanostructures [11, 40, 41]. Nano size patterns were fabricated with variation in features and hydrophobicity measured. A high wettability surface prevents the absorption on the surface by excessive flow and availability of the liquid whereas no wettability results in a lack of accessibility with no liquid drop able to hold the surface. In order to

practically test both extremes, sample surfaces of titanium were patterned in nanoscale range with change in parameters such as shape, groove spacing, and thickness to control the dimensions of the nanostructure whereas laser energy was also varied to control the roughness of the nanostructures fabricated. Titanium was chosen due to its conductive metal nature to form structures through laser ablation process and its biocompatibility with vast use in medical applications such as orthopaedics [42, 43], implants [44-46] and metal based antimicrobial coatings [47-49] that made it a perfect choice for this study of patterning nanostructures on surface and controlling the features for the desired hydrophilic and hydrophobic properties.

5.2 Methods

5.2.1 Fabrication

Direct laser interference patterning (DLIP) method was used to fabricate nanostructures. This mask free laser interference lithography is a novel technique which meets the requirement of fabricating sophisticated devices with low cost and fast fabrication process. Laser ablation based fabrication techniques have been extensively utilized in the field of optical devices, including diffraction gratings, lens, diffuser, and optical data storage devices [11, 50].

In this work, PECVD method was used to prepare titanium samples with different thicknesses with an accuracy of 0.1 nm. A neodymium-doped yttrium aluminium garnet (Nd:YAG) laser (λ=1064 nm, 3.5 ns pulse, 1 kHz) was used for laser ablation. The setup consisted of a plane or concave reflecting mirror, sample holder and a beam reflector to divert the beam toward the reflecting mirror placed just after the sample. A detailed analysis on surface fabrication process is made in Section 5.3.

5.2.2 Optical Characterization

A halogen light source (HL-2000, Ocean Optics), Red, Green and Blue Laser beams were used for illumination purposes. Diffraction pattern images were captured using a digital

camera. The setup consisted of a pointer beam holder, sample holder and display screen placed at measured distances as shown in **Figure 5.1**. Image J (Wayne Rasband, USA) was used to measure the peak intensities of diffraction spots and variation in their locations for different samples.

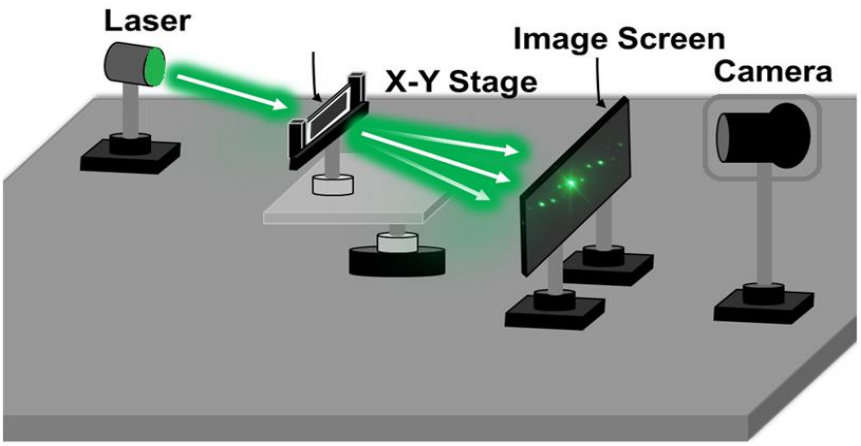

Figure 5.1. Optical Characterization Setup Schematics [51]

5.2.3 Hydrophobicity

In wettability measurement protocol, 2 µl size droplets were gently placed at the surface using a micro syringe. Images were captured using the camera with 1000x optical zoom and static angle measurements were performed using fundamental angle measurement protocols. Contact angle measurements were confirmed using Image J (Wayne Rasband, USA). The same hydrophobicity setup was used for contact angle measurements as mentioned in previous Sections 2.2.4 and 3.2.4.

5.3 Surface fabrication

A complete overview of the fabrication process is shown in **Figure 5.2**. An Nd: YAG laser beam (λ=1064 nm, 3.5 ns pulse, 1 kHz) with spot size of 1 cm in diameter was used to fabricate structures on the titanium surface. Plasma enhanced chemical vapour decomposition (PECVD) method was used to deposit titanium on the glass slides with precise thicknesses at

the nanoscale. This deposition work was carried out at University of Glasgow with the help of Dr. Affar Karimullah. He is a research associate in the department of Chemistry. Samples of 15 nm, 30 nm, 50 nm, 150 nm and 225 nm thicknesses were fabricated for nanopatterning and experimental purposes. The samples were then cleaned with standard procedures using DI water to clear any dust particles away and drying with N2 gas. The samples were placed on the holding stand above the reflecting mirror as shown in **Figure 5.2a**. This fabrication method is based on the Denisyuk reflection method. The surface of the material was exposed to the laser beam for the same time period as the duration of the ablating pulse. Two coherent beams (incident beam and reflected beam from mirror shown in **Figure 5.2a**) travelling in opposite direction caused interference phenomena resulting in surface pattering [41, 51, 52]. The expressions for incident beam y_1 and reflected beam y_2 are as

$$y_1 = A\cos 2\pi\left(vt + \frac{x}{\lambda}\right);\;\; y_2 = A\cos 2\pi\left(vt - \frac{x}{\lambda}\right) \quad \text{..... (Eq. 5.1)}$$

where *A* is the amplitude of the wave and *x* is the co-ordinate along the propagation path. Hence, the expression for equation of interference standing wave is

$$y = y_1 + y_2 = A\cos 2\pi\left(vt + \frac{x}{\lambda}\right) + A\cos 2\pi\left(vt - \frac{x}{\lambda}\right)$$

$$y = \left|2A\cos 2\pi\left(\frac{x}{\lambda}\right)\right|\cos 2\pi(vt) \quad \text{..... (Eq. 5.2)}$$

Where the absolute part represents the distribution of the resultant wave along the *x* direction along the propagation path. Regions of constructive interference ablated the material and the regions with destructive interference remained non-ablated. Hence, a periodic grating structure is formed on the surface covering a circular area of ~0.8 cm in diameter. The interference pattern based surface grating period (Λ) is dependent on the incident laser beam wave length λ and tilt angle θ with reference to horizontal plane.

$$\Lambda = \frac{\lambda}{\sin\theta} \quad \text{..... (Eq. 5.3)}$$

The diffraction grating period also has dependency on laser energy (E), thickness of layer (h) and distance (d) from the reflecting mirror. These dependencies have been discussed further through experiments performed in this work. The ablated material was sucked by a vacuum pump into the filter. It was placed very near to the sample in order to clear the surface of the sample as well as the air in the chamber. **Figure 5.2b** shows the grating structure formed on the titanium surface. A flat reflecting mirror was used in this case. The sample thickness was 150 nm and the tilt angle was kept 10°. The energy used was 120 mJ/cm². The largest grating period achieved was calculated to be ~1.68 μm which is in microscale. However, increase in the tilt angle resulted a grating period as small as 300 nm.

Similarly, **Figure 5.2c** and **d** show the circular Fresnel ring structures fabricated using the same procedure. In this case, the flat reflecting mirror was replaced with a concave mirror with focal length of 6 cm which focused the reflected beam towards the focal point. The constructive interference ablated the material whereas the destructive regions remained non-ablated resulting ring structures as the reflecting surface was a concave mirror[51, 52]. The structures were fabricated at two different height locations from the reflecting mirror within the focal length range. Different spacing was seen in the circular rings. Change in height of the sample from the mirror changed the size of the central fringes. Two different energy levels (120 mJ/cm² and 210 mJ/cm²) were used to see the difference in the smoothness of the structures. Higher energy fabricated the structure with more precise and smooth effect. **Figure 5.2e-h** show the grating structures fabricated on different thicknesses varying from 5 nm to 50 nm keeping the tilt angle constant at 10° and the energy constant at 120 mJ/cm². The periodicity of the structures fabricated ranged from ~1.66 μm to ~1.68 μm.

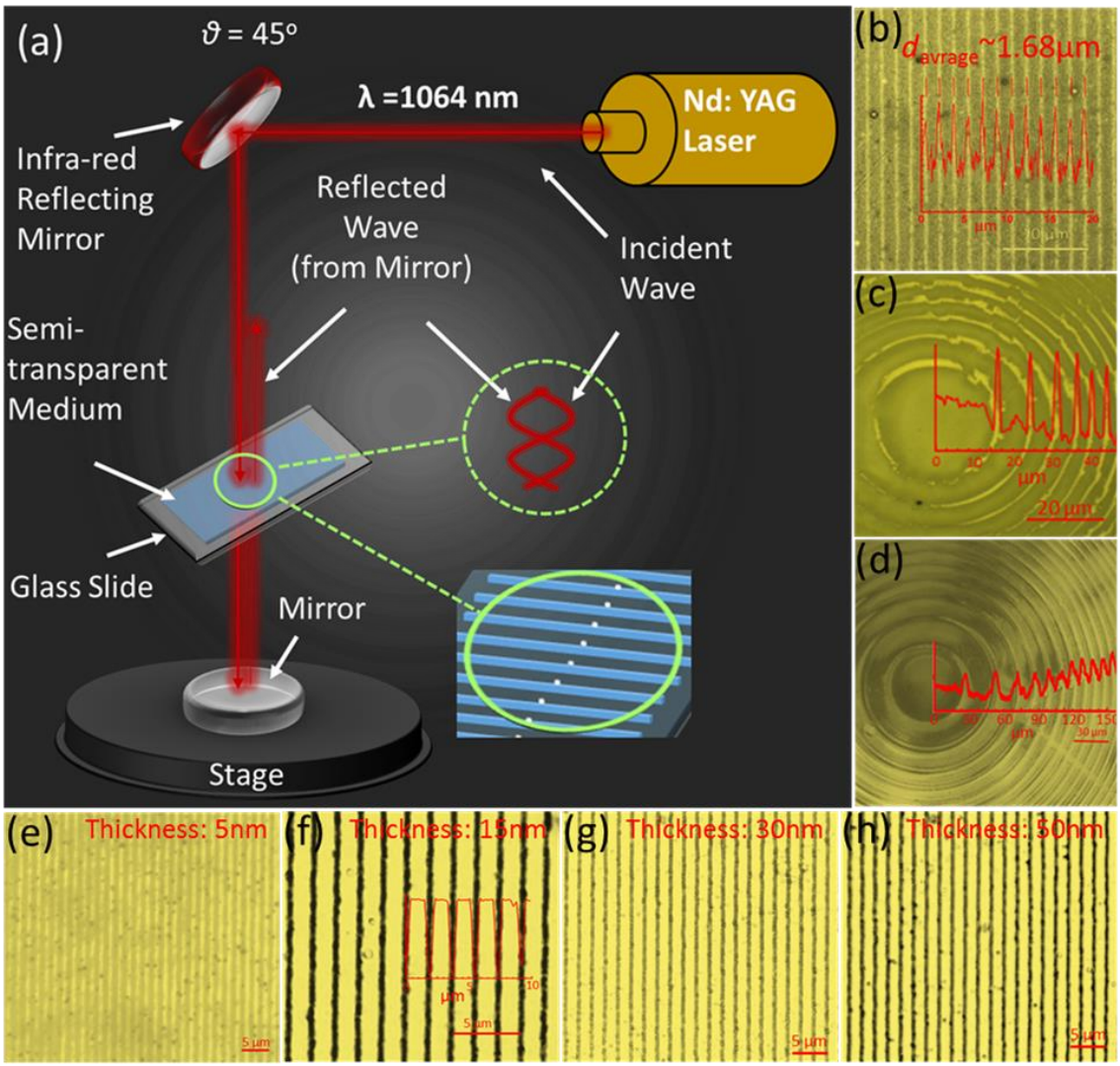

Figure 5.2. Fabrication by Direct Laser Interference patterning in Denisyuk reflection mode. **(a)** Nd:YAG Laser beam passing through a set of mirror and sample **(b)** 1D grating pattern with period 1.68 µm and thickness 150 nm **(c)** Fresnel Rings Structure with size varying from 0.3 µm to 10 µm **(d)** Fresnel Rings Structure with size varying from 0.3 µm to 30 µm **(e)** 1D grating pattern with period 1.66 µm and thickness 5 nm **(f)** 1D grating pattern with period 1.68 µm and thickness 15 nm **(g)** 1D grating pattern with period 1.67 µm and thickness 30 nm **(h)** 1D grating pattern with period 1.68 µm and thickness 50 nm.

5.4 Surface characterisation

Patterned surfaces were analysed using illumination by three different monochromatic laser beam lights i.e. blue (450 nm), green (532 nm) and red (635 nm) as well as broadband light. Results were plotted for diffraction intensity versus angle. The location of the diffracted spots varied confirming the change in dimensions of the structure and its uniformity. Some space on the sample was left unpatterned for reference purposes. Imaging was performed using an optical microscope to see the structure and its roughness. Far field diffraction patterns were observed on a screen and were captured using a digital camera at a fix position on the setup stage. **Figure 5.3a** and **5.2b** show the images of the grating structures fabricated. **Figure 5.3a(i – iv)** and **5.2b(i – iv)** show the respective images of patterns captured after illuminating with white broadband light, red, green and blue wavelength laser beams respectively. Diffused spots confirm more roughness of the surface and the spacing of the structure whereas clear and intense spots verify more precise ablation has taken place. The spacing and the surface of the edges of the structure are more clear and smooth hence diffusing less light. Two dimensional gratings were also fabricated for experimental purposes. The procedure for fabrication was same as for 1D grating but this time the sample was exposed twice to the laser beam. The sample was rotated horizontally keeping the location of the centre of axes constant. The horizontal rotation in angle was pre-calculated before exposing it to a laser beam for the second time. Horizontal rotation of 90 degrees will allow us to fabricate squares whereas calculations can be made to fabricate shapes like rectangles, rhombus, parallelograms etc by rotating the sample at angles such as 60, 30 15 or 10 degrees. The periodicity of the structures fabricated ranged from ~1.66 μm to ~1.68 μm for a tilt angle of 10º. Optical characterisation was done using the same protocols as for 1D grating with red, green and blue laser beams as well as broadband light. **Figure 5.3c (i – iv)** shows the image of the fabricated structure and illumination results showing diffraction spots at two different axis confirming the 2D effect.

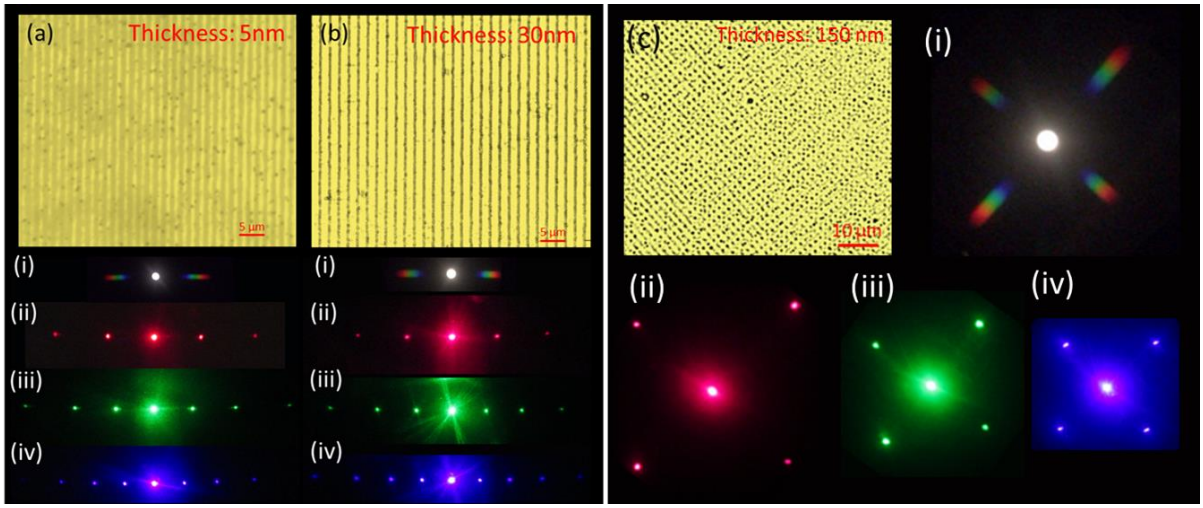

Figure 5.3. Grating and diffraction patterns of **(a)** 1D grating with thickness 5 nm **(b)** 1D grating with thickness 30 nm **(c)** 2D grating with thickness 150 nm. Diffraction patterns for 1D and 2D gratings illuminated by **(i)** white broadband light **(ii)** Red **(iii)** Green **(iv)** Blue laser beams respectively.

The grating dimensions were varied to see the effect on the diffraction spots. Gratings were fabricated with different dimensions by changing the tilt angle whereas keeping the energy level and distance from reflecting mirror constant. The tilt angle as varied from 10º to 45º which resulted in fabrication of 1D gratings in the range of 0.3 µm to 3 µm respectively. A tilt angle of 10° resulted a period of 0.3 µm whereas the size increased with an increase in angle with a step of 5°. The maximum period size achieved was 3 µm for the tilt angle 45°. These gratings were then illuminated with a red laser beam. As the groove size increased, the distance between the diffraction spots increased and vice versa. **Figure 5.4(i-vi)** show the results confirming the fact that as the grating dimension increased, the dots moved apart and vice versa.

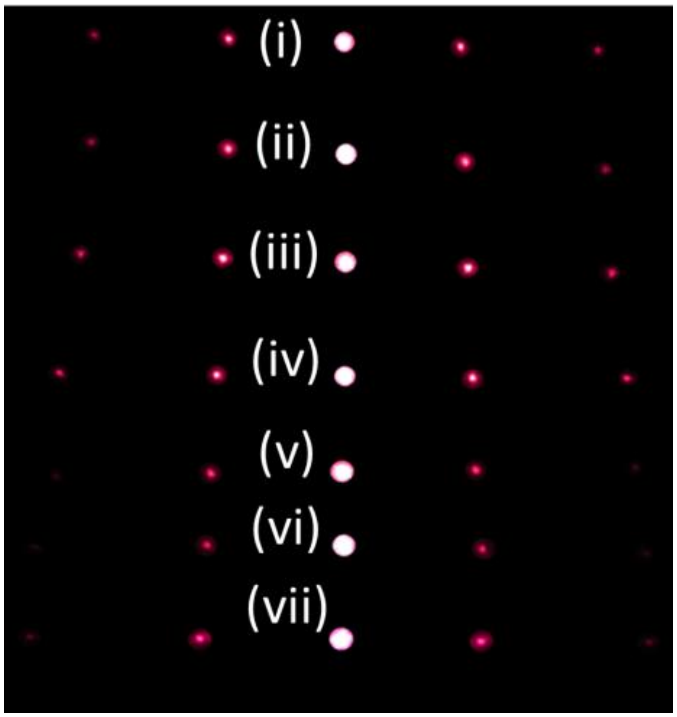

Figure 5.4. Diffraction analysis **(i-vii)** Practically achieved diffraction patterns showing change in location of diffraction spots with varied grating dimensions.

Laser energy was varied from 30 mJ/cm² to 210 mJ/cm². The tilt angle was kept at 10 degrees for both samples with thicknesses 150 nm and 225 nm respectively. The diffraction peaks were plotted as shown in **Figure 5.5a** and **5.5b**. The results show that higher energy resulted in more precise ablation. The diffraction peaks of higher intensity were observed for higher energy ablated structures whereas low peak intensities were seen for the lower energy case. This indicates that more light was diffused the lower energy case and the surface was rough and the spacing was not clear. More perfection was achieved in ablation with an increase in energy. Grating became clearer, sharper and smooth whereas it was rough, porous and wider area was ablated with lesser energy.

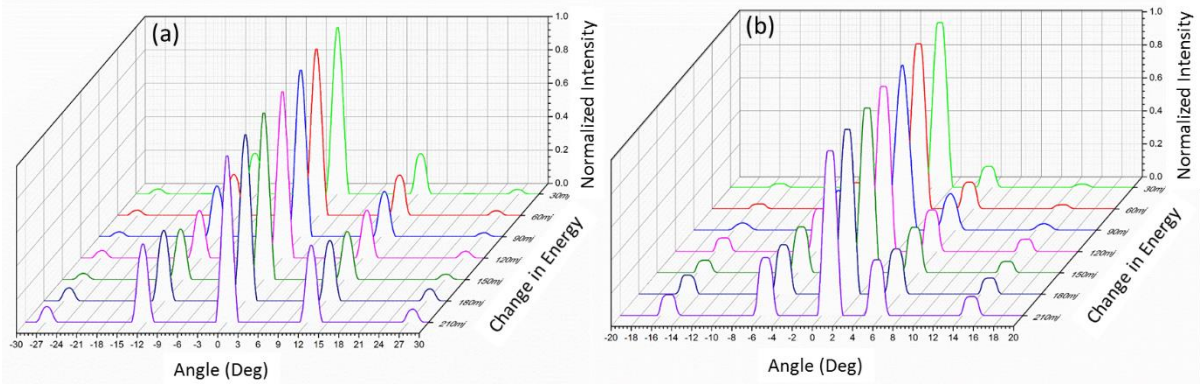

Figure 5.5. Diffraction peak intensity analysis with change in ablation energy keeping tilt angle constant at 10º **(a)** Sample thickness 150 nm **(b)** Sample thickness 225 nm

The flat reflecting mirror shown in setup (**Figure 5.2a**) was replaced with a concave mirror with a focal length of 6 cm. The sample was then placed within the focal length region of the mirror. The laser pulse when reflected, converged towards the focal point hence two beams ablating the material in the shape of concentric rings like structures also known as Fresnel ring structures or Fresnel zone plate. The size of the central and side fringes depends on the location of the sample. Sample if placed very close to the focal point will have narrow central and side fringes whereas these fringes are further apart when the sample is half way towards the concave mirror from the point of focus. Ring structures were fabricated with variation in the location of the sample which allowed us to fabricate ring structures with slight variations in size. The variation in the periodicity of the structures fabricated ranged from ~0.3 μm to ~30 μm. **Figure 5.6** shows images of the structures fabricated with variation in size observed.

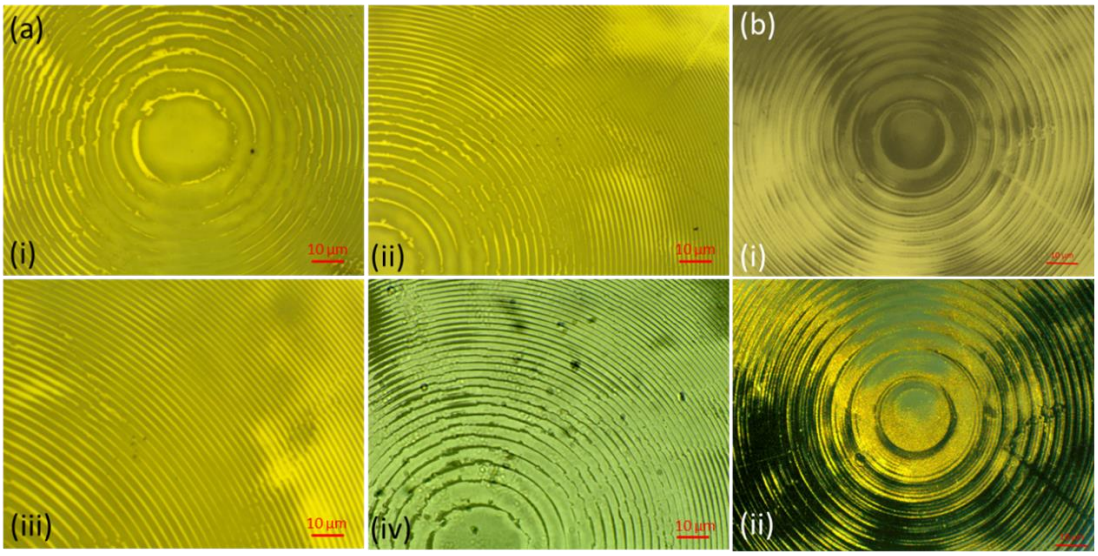

Figure 5.6. Fabricated Fresnel ring structures **(a)(i-iv)** Size varying from 0.3 to 10 µm. **(b)(i-ii)** Size varying from 0.3 to 30 µm.

Correlations between Wavelength (λ), Thickness(h), Laser Energy(mJ), the Tilt angle (θ), Grating period (Λ) and distance of the sample from reflecting mirror (d) were plotted as shown in **Figure 5.7**. **Figure 5.7a** and **b** show the images of the structures fabricated. Plot in **Figure 5.7c** compares the experimental and bragg model results. More increase in the tilt angle, the lower the grating period and vice versa. **Figure 5.7d-f** show the effect on grating period with change in parameters such as laser energy, distance from laser and height of the sample from the reflecting mirror.

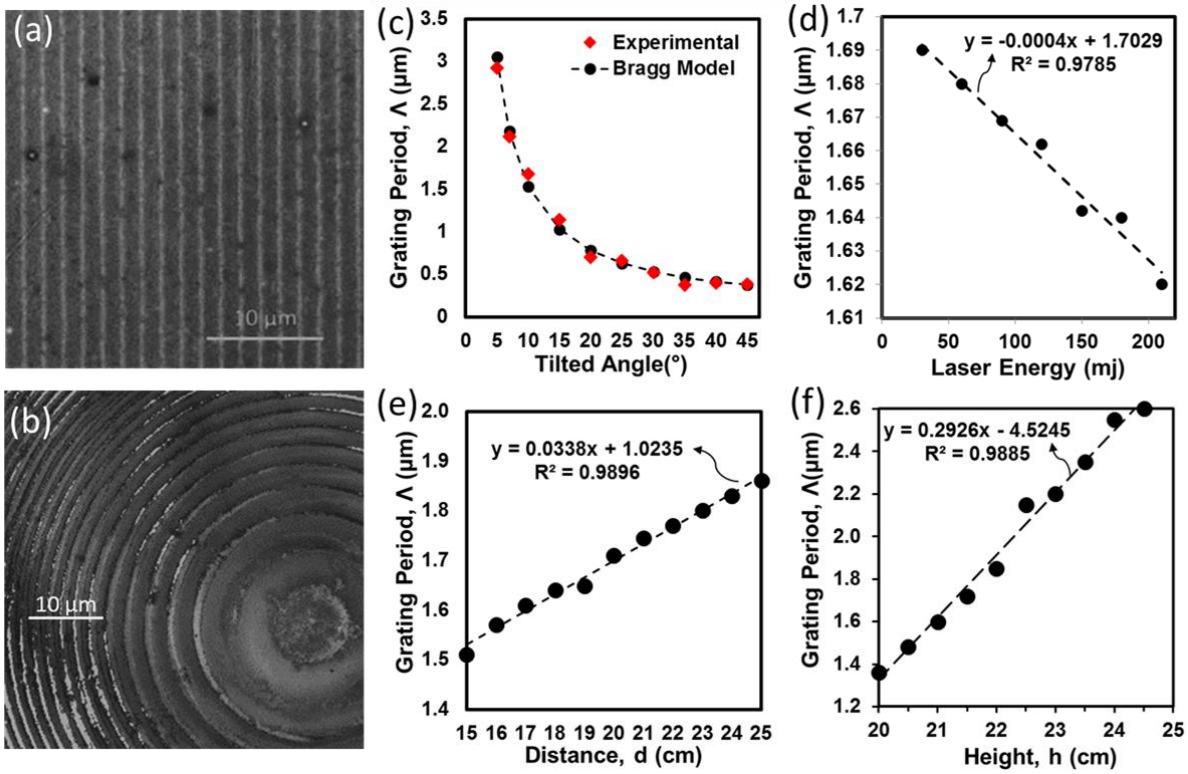

Figure 5.7. Experimental measurements of fabricated structures **(a)** 1D grating image **(b)** Fresnel Ring Structure Image. Plots showing grating period verses **(c**) tilt angle **(d)** laser energy **(e)** distance of the sample from laser **(f)** change in height of the sample from the reflecting mirror.

5.5 Hydrophobicity Results and Discussion

To start with, the contact angle was measured on the polished titanium surface first as reference using the protocols explained earlier in Section 5.2.3. **Figure 5.8a** below shows a contact angle of 93º observed on a polished surface for a drop size of 2 µl. Measurements were made on two different samples with thicknesses 150 nm and 225 nm respectively. Images were taken by placing the optical camera in parallel to the grating line structures. 1D grating structures were patterned on both samples in order to measure the variation in the contact angles achieved. The tilt angle of both samples was varied from 10º to 35º to fabricate patterns of different grating periods ranging from 0.3 µm to 3 µm. The droplets were placed on the patterned surfaces and the images were captured to carry out the measurements. **Figure 5.8a**

shows the contact angle with plane surface for reference. A contact angle variation from 30º to 48º was seen for the first sample with thickness 150 nm (**Figure 5.8b**) whereas a variation from 30º to 60º in contact angle was observed for the second sample with a thickness of 225 nm as shown in **Figure 5.8c**. These angles were measured from images captured by the optical camera positioned in parallel to the lines of grating structure. The second sample showed a higher contact angle as compared to the first. This effect is due to the increase in thickness of the sample resulting more height in the patterned grooves. Measurements were made for the 2D patterns fabricated on the sample with thickness 225 nm. The contact angle variation observed ranged from 21º to 57º (**Figure 5.8d**) showing a decrease in the contact angle variation with respect to the 1D grating pattern. This is due to more accessibility in 2D patterns where the droplet can spread over a larger area in two dimensions resulting in a decrease in the contact angle as compared to the 1D grating structure.

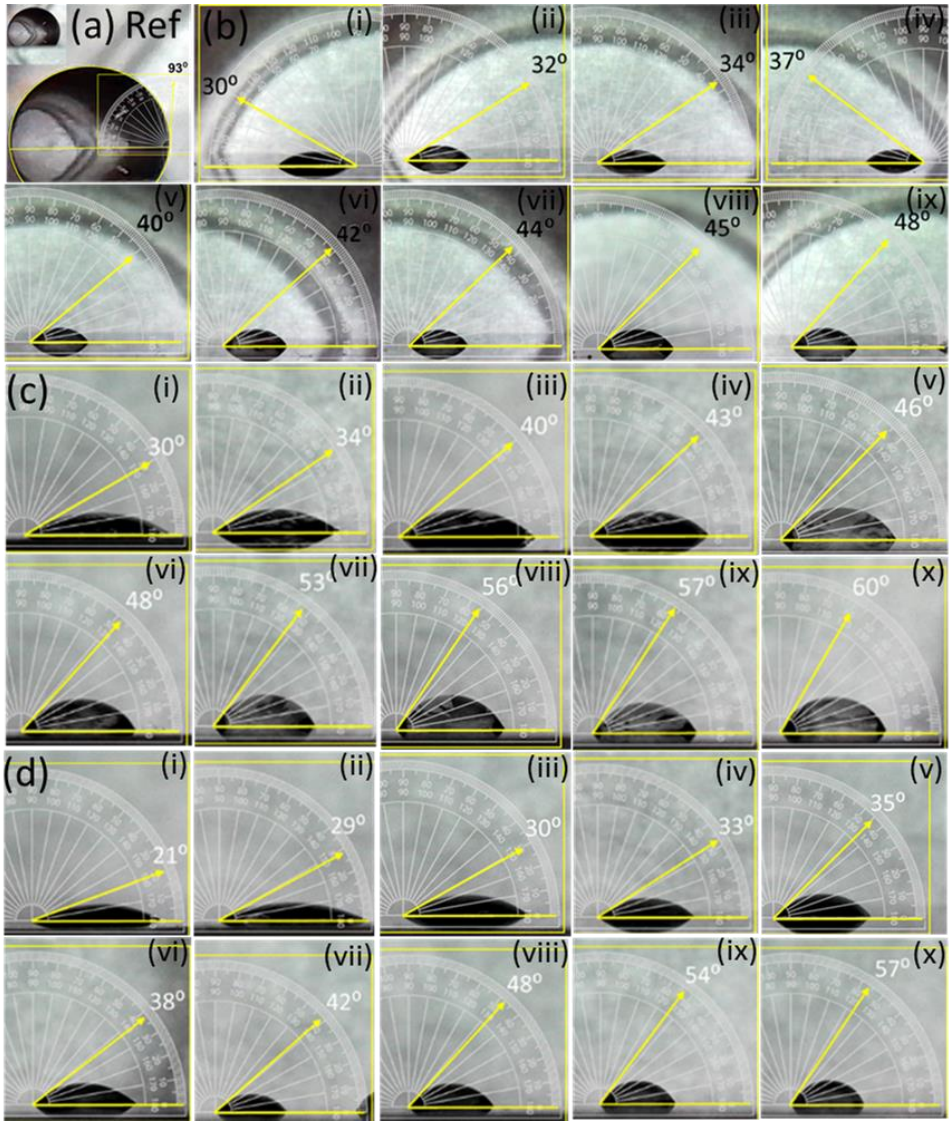

Figure 5.8. Hydrophobicity analysis performed using image J (protector in images used as an illustration schematic to display values) **(a)** Reference from polished titanium surface **(b**) Sample with thickness 150 nm **(c)** Sample with thickness 225 nm **(d)** sample with thickness 225 nm - 2D gratings.

Hydrophobicity measurements were also recorded on Fresnel patterned surfaces with different sample thicknesses. The gap in the Fresnel rings was varied from 0.3 µm to 3 µm. A variation in contact angle was observed from 43º to 64º (**Figure 5.9a**) for ring patterns fabricated on the sample with thickness 15 nm.

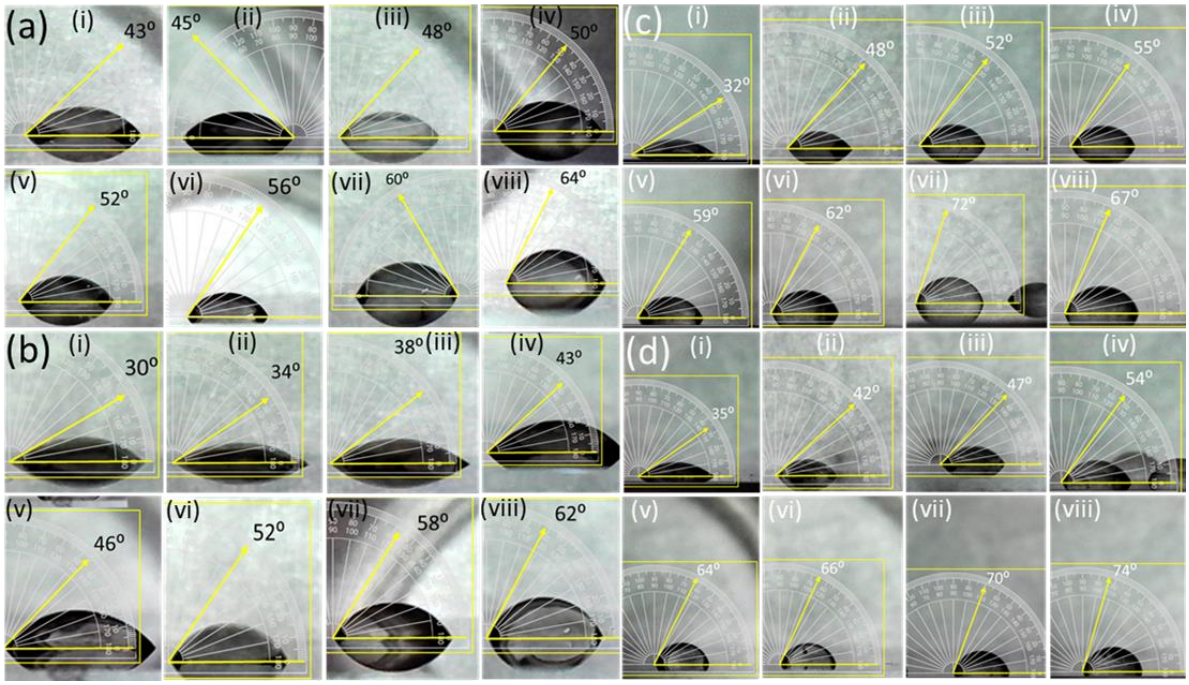

Figure 5.9. Circular ring structures and variation in contact angles obtained by image J (protector in image used as an illustration schematic to display values) **(a)** 15 nm thickness **(b)** 30 nm thickness **(c)** 150 nm thickness **(d)** 225 nm thickness.

A similar trend was observed for the sample with thickness 30 nm. A variation of 30º to 62º (**Figure 5.9b**) in contact angle was observed for the ring patterns fabricated on this sample. A lower contact angle was seen as compared to the previous sample.

Further analysis was made for patterns fabricated on samples with thicknesses 150 nm and 225 nm in order to clarify the role of thickness with respect to change in contact angle. A variation of 32º to 72º (**Figure 5.9c**) was observed for the sample with thickness 150 nm. It can be seen that the increase in the thickness of the structure increased the contact angle boundaries although the spacing variations were kept the same as of other samples. The lower boundary of the contact angle variation had a slight increase to 32º whereas the higher boundary showed 72º. Observations were made for the sample with thickness 225 nm. A variation from 35º to 74º was observed as shown in **Figure 5.9d**. The boundaries have shown a slight increase in contact angle level as compared to the previous samples. This effect is due to the increase in the thickness of the structures. Results were plotted in order to draw some conclusions based on

the experiments conducted. **Figure 5.10a** shows the trend between the grating period and the contact angle. A decrease in the grating period increased the contact angle and vice versa. This effect is due to the decrease in surface energy and higher interfacial tension whereas increase in the grating period increased the surface energy and lowered the interfacial tension resulting low contact angle. A similar trend is seen in **Figure 5.10b** where the decrease in gap size of ring structure increased the contact angle and vice versa. An increase in thickness of the ring structures from 15 nm to 225 nm resulted in an increase in the contact angle. A trend between thickness and contact angle is plotted in **Figure 5.10c** where the energy level was kept constant at 150 mJ/cm² for fabricating the structures through ablation. An increase in thickness resulted in an increase in the contact angle and vice versa. Increasing the thickness lowered the surface energy and higher interfacial tension resulting a higher contact angle and vice versa. A correlation between the energy used for material ablation and the contact angle of the structure is plotted in **Figure 5.10d**. An increase in energy showed a deeper and smoother ablation of grooves in the material resulting in an increase in the thickness of the fabricated structure. As a result, increased height of the structure demonstrated lower surface energy and high interfacial tension consequently resulting an increase in the contact angle.

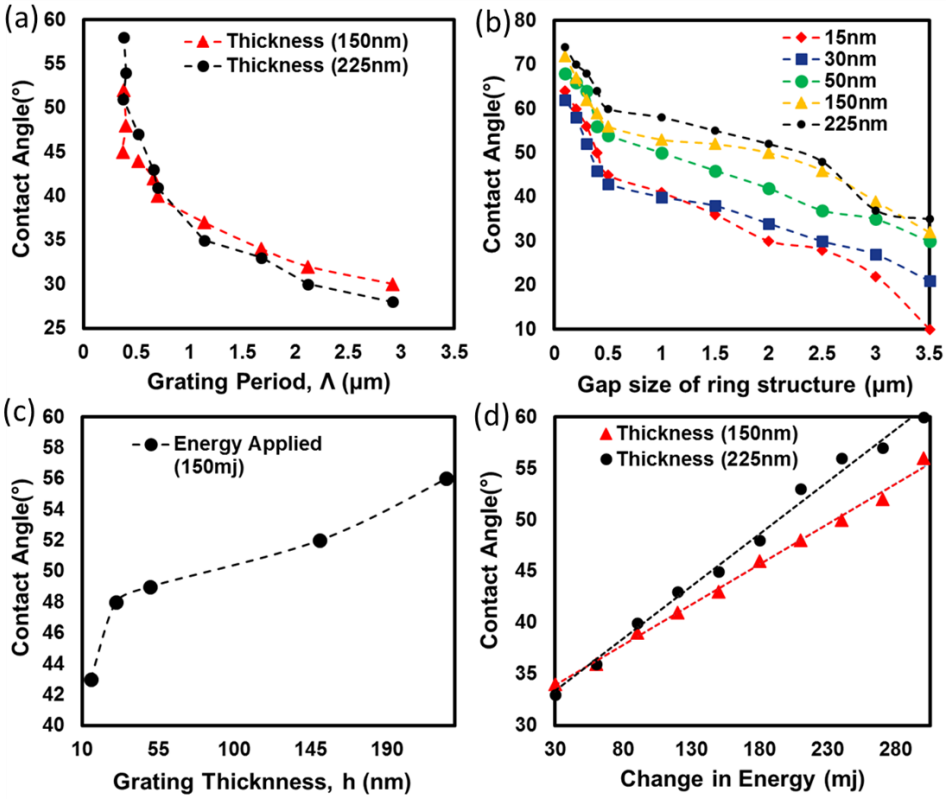

Figure 5.10. Contact angle trend lines observed for **(a)** two different sample thicknesses with variation in contact angle versus grating period **(b)** five different sample thicknesses with variation in contact angle versus gap size **(c)** contact angle versus grating thickness for five samples keeping energy constant at 150 mJ/cm² **(d)** two different sample thicknesses with variation in contact angle versus energy.

5.6 Summary

We have practically demonstrated patterning of nanostructures through direct laser interference ablation technique. We patterned 1D, 2D and Fresnel ring structures with variable dimensions through this fast fabrication method in order to study and achieve optimization of hydrophobic properties of titanium surfaces. We have observed that by controlling the dimensions as well as the smoothness of the fabricated nanostructures, a required level of hydrophobicity can be achieved. A decrease in the structure size increased the contact angle and vice versa. This effect was due to the decrease in surface energy and higher interfacial

tension whereas increase in the grating period size increased the surface energy and lowered the interfacial tension resulting low contact angles. These nano grooves acted as nano channels allowing the accessibility and flow of the liquid controlling the wettability features. The overall contact angles achieved for these structures were in the range of 20° to 74° which show a promising variation. These precise structures can be used in biomedical applications such as metal based antimicrobial coatings, implants and biosensors where controllability of the desired hydrophobic and hydrophilic properties is an essential for cell attachment and cell growth and it is not currently being achieved with conventional methods. Patterning titanium surface with nanostructures may possibly enhance the cell attachment and cell growth mechanism faced by most implant failures.

Bibliography

1. Jamil, M.I., et al., *Icephobic Strategies and Materials with Superwettability: Design Principles and Mechanism.* Langmuir, 2018. **34**(50): p. 15425-15444.
2. Hasan, J., S. Jain, and K. Chatterjee, *Nanoscale Topography on Black Titanium Imparts Multi-biofunctional Properties for Orthopedic Applications.* Scientific Reports, 2017. **7**: p. 41118.
3. Tang, X., et al., *Bioinspired Nanostructured Surfaces for On-Demand Bubble Transportation.* ACS Applied Materials & Interfaces, 2018. **10**(3): p. 3029-3038.
4. Farshchian, B., et al., *Droplet impinging behavior on surfaces with wettability contrasts.* Microelectronic Engineering, 2018. **195**: p. 50-56.
5. Sharma, V., et al., *Gladiolus dalenii Based Bioinspired Structured Surface via Soft Lithography and Its Application in Water Vapor Condensation and Fog Harvesting.* ACS Sustainable Chemistry & Engineering, 2018. **6**(5): p. 6981-6993.
6. Flynn Bolte, K.T., et al., *Probing Liquid–Solid and Vapor–Liquid–Solid Interfaces of Hierarchical Surfaces Using High-Resolution Microscopy.* Langmuir, 2018. **34**(12): p. 3720-3730.

7. Bhushan, B. and E.K. Her, *Fabrication of Superhydrophobic Surfaces with High and Low Adhesion Inspired from Rose Petal.* Langmuir, 2010. **26**(11): p. 8207-8217.
8. Feng, L., et al., *Petal Effect: A Superhydrophobic State with High Adhesive Force.* Langmuir, 2008. **24**(8): p. 4114-4119.
9. Yuan, C., et al., *A simple approach to fabricate the rose petal-like hierarchical surfaces for droplet transportation.* Applied Surface Science, 2016. **385**: p. 562-568.
10. Zheng, Y., X. Gao, and L. Jiang, *Directional adhesion of superhydrophobic butterfly wings.* Soft Matter, 2007. **3**(2): p. 178-182.
11. AlQattan, B., et al., *Holographic direct pulsed laser writing of two-dimensional nanostructures.* RSC Advances, 2016. **6**(112): p. 111269-111275.
12. Barthlott, W. and C. Neinhuis, *Purity of the sacred lotus, or escape from contamination in biological surfaces.* Planta, 1997. **202**(1): p. 1-8.
13. Gou, X. and Z. Guo, *Superhydrophobic Plant Leaves: The Variation in Surface Morphologies and Wettability during the Vegetation Period.* Langmuir, 2019.
14. Monroe, J.I. and M.S. Shell, *Computational discovery of chemically patterned surfaces that effect unique hydration water dynamics.* Proceedings of the National Academy of Sciences, 2018. **115**(32): p. 8093.
15. Borri, C. and M. Paggi, *Topological characterization of antireflective and hydrophobic rough surfaces: are random process theory and fractal modeling applicable?* Journal of Physics D: Applied Physics, 2015. **48**(4): p. 045301.
16. Moreira, D., et al., *Dynamic superhydrophobic behavior in scalable random textured polymeric surfaces.* Journal of Applied Physics, 2016. **119**(12): p. 125302.
17. Luu, T.U., et al., *Micro- and Nanopatterned Topographical Cues for Regulating Macrophage Cell Shape and Phenotype.* ACS Applied Materials & Interfaces, 2015. **7**(51): p. 28665-28672.
18. Lu, Y., et al., *Preparation of superhydrophobic titanium surfaces via electrochemical etching and fluorosilane modification.* Applied Surface Science, 2012. **263**: p. 297-301.
19. Hwang, B.J. and S.H. Lee, *Study on micro fabricated stainless steel surface to anti-biofouling using electrochemical fabrication.* Micro and Nano Systems Letters, 2017. **5**(1): p. 16.
20. Wang, Z., et al., *Superhydrophobic nanocoatings prepared by a novel vacuum cold spray process.* Surface and Coatings Technology, 2017. **325**: p. 52-57.
21. Jung, Y.C. and B. Bhushan, *Dynamic Effects Induced Transition of Droplets on Biomimetic Superhydrophobic Surfaces.* Langmuir, 2009. **25**(16): p. 9208-9218.

22. Reyssat, M. and D. Quéré, *Contact Angle Hysteresis Generated by Strong Dilute Defects.* The Journal of Physical Chemistry B, 2009. **113**(12): p. 3906-3909.
23. Kwon, Y., et al., *Design of Surface Hierarchy for Extreme Hydrophobicity.* Langmuir, 2009. **25**(11): p. 6129-6136.
24. Hashimoto, Y. and T. Yamamoto, *Fabrication of an Anti-Reflective and Super-Hydrophobic Structure by Vacuum Ultraviolet Light-Assisted Bonding and Nanoscale Pattern Transfer.* Micromachines, 2018. **9**(4).
25. Wong, T.-S., A.P.-H. Huang, and C.-M. Ho, *Wetting Behaviors of Individual Nanostructures.* Langmuir, 2009. **25**(12): p. 6599-6603.
26. Zhang, X., et al., *Morphology and Wettability Control of Silicon Cone Arrays Using Colloidal Lithography.* Langmuir, 2009. **25**(13): p. 7375-7382.
27. Zhou, B., et al., *A facile and cost-effective approach to engineer surface roughness for preparation of large-scale superhydrophobic substrate with high adhesive force.* Applied Surface Science, 2016. **389**: p. 679-687.
28. Li, G., et al., *One-step facile fabrication of controllable microcone and micromolar silicon arrays with tunable wettability by liquid-assisted femtosecond laser irradiation.* RSC Advances, 2016. **6**(44): p. 37463-37471.
29. Dou, W., et al., *An efficient way to prepare hydrophobic antireflective SiO2 film by sol–gel method.* Materials Letters, 2016. **167**: p. 69-72.
30. Kumar, D., et al., *Hydrophobic sol–gel coatings based on polydimethylsiloxane for self-cleaning applications.* Materials & Design, 2015. **86**: p. 855-862.
31. Biggs, M.J.P., R.G. Richards, and M.J. Dalby, *Nanotopographical modification: a regulator of cellular function through focal adhesions.* Nanomedicine: Nanotechnology, Biology and Medicine, 2010. **6**(5): p. 619-633.
32. Dvir, T., et al., *Nanotechnological strategies for engineering complex tissues.* Nature Nanotechnology, 2010. **6**: p. 13.
33. Tay, C.Y., et al., *Micro-/Nano-engineered Cellular Responses for Soft Tissue Engineering and Biomedical Applications.* Small, 2011. **7**(10): p. 1361-1378.
34. Variola, F., et al., *Nanoscale surface modifications of medically relevant metals: state-of-the art and perspectives.* Nanoscale, 2011. **3**(2): p. 335-353.
35. Ventre, M., F. Causa, and A. Netti Paolo, *Determinants of cell–material crosstalk at the interface: towards engineering of cell instructive materials.* Journal of The Royal Society Interface, 2012. **9**(74): p. 2017-2032.

36. Ta, V.D., et al., *Laser textured superhydrophobic surfaces and their applications for homogeneous spot deposition.* Applied Surface Science, 2016. **365**: p. 153-159.
37. Song, Y., et al., *Controllable superhydrophobic aluminum surfaces with tunable adhesion fabricated by femtosecond laser.* Optics & Laser Technology, 2018. **102**: p. 25-31.
38. Yong, J., et al., *Femtosecond laser ablated durable superhydrophobic PTFE films with micro-through-holes for oil/water separation: Separating oil from water and corrosive solutions.* Applied Surface Science, 2016. **389**: p. 1148-1155.
39. Alqurashi, T., et al., *Femtosecond laser ablation of transparent microphotonic devices and computer-generated holograms.* Nanoscale, 2017. **9**(36): p. 13808-13819.
40. AlQattan, B., A.K. Yetisen, and H. Butt, *Direct Laser Writing of Nanophotonic Structures on Contact Lenses.* ACS Nano, 2018. **12**(6): p. 5130-5140.
41. AlQattan, B., et al., *Laser Nanopatterning of Colored Ink Thin Films for Photonic Devices.* ACS Applied Materials & Interfaces, 2017. **9**(45): p. 39641-39649.
42. Hasan, J., S. Jain, and K. Chatterjee, *Nanoscale Topography on Black Titanium Imparts Multi-biofunctional Properties for Orthopedic Applications.* Scientific Reports, 2017. **7**(1): p. 41118.
43. Bahl, S., et al., *Surface nanostructuring of titanium imparts multifunctional properties for orthopedic and cardiovascular applications.* Materials & Design, 2018. **144**: p. 169-181.
44. Ganjian, M., et al., *Reactive ion etching for fabrication of biofunctional titanium nanostructures.* Scientific Reports, 2019. **9**(1): p. 18815.
45. Medvedev, A.E., et al., *Effect of bulk microstructure of commercially pure titanium on surface characteristics and fatigue properties after surface modification by sand blasting and acid-etching.* Journal of the Mechanical Behavior of Biomedical Materials, 2016. **57**: p. 55-68.
46. Ferraris, S., et al., *Antibacterial and bioactive nanostructured titanium surfaces for bone integration.* Applied Surface Science, 2014. **311**: p. 279-291.
47. Janković, A., et al., *Graphene-based antibacterial composite coatings electrodeposited on titanium for biomedical applications.* Progress in Organic Coatings, 2015. **83**: p. 1-10.
48. Hatton, B.D., *13 - Antimicrobial coatings for metallic biomaterials*, in *Surface Coating and Modification of Metallic Biomaterials*, C. Wen, Editor. 2015, Woodhead Publishing. p. 379-391.

49. Sengstock, C., et al., *Structure-related antibacterial activity of a titanium nanostructured surface fabricated by glancing angle sputter deposition.* Nanotechnology, 2014. **25**(19): p. 195101.
50. Ahmed, R., et al., *Printable ink lenses, diffusers, and 2D gratings.* Nanoscale, 2017. **9**(1): p. 266-276.
51. Ahmed, R. and H. Butt, *Diffractive Surface Patterns through Single-Shot Nanosecond-Pulsed Laser Ablation.* ACS Photonics, 2019. **6**(7): p. 1572-1580.
52. AlQattan, B., et al., *Conformable Holographic Photonic Ink Sensors Based on Adhesive Tapes for Strain Measurements.* ACS Applied Materials & Interfaces, 2019. **11**(32): p. 29147-29157.

Chapter 6: Conclusion and Future work

6.1 Introduction

This thesis is aimed at developing optical devices inspired by nature. The research covered investigation of unique samples in nature, modelling of optical devices, optical characterisation and fabrication. It also involved studies made on hydrophobicity and interaction of liquids with unique samples from nature.

6.2 Contributions

Significant contributions made can be summarized as follows:

1. A novel study was conducted on structural colouration in Nicobar Pigeon bird species and have not been reported before. The inspiration was to learn from nature and contribute towards manufacturing artificial nature inspired photonic bandgap sensors devices and systems with less complexity but better performance.

2. Another novel study was conducted on structural colouration in Himalayan Monal Pheasant bird species that exist in nature and have not been reported before. TEM was performed and internal structure was studied. Hydrophobicity and interaction of different liquids with these samples was studied and concluded.

3. A novel sample device was successfully modelled and fabricated using materials such as Si and SiO_2 to understand the colour selective mechanism of nanostructures with their interaction with light and factors affecting the optical properties such as refractive index of the material, dimensions and periodicity of the nanostructure. These investigations have led to a study of a new type of hierarchical grating that displayed optical properties which could be controlled independently.

4. Another novel sample device was fabricated using fast direct laser interference patterning method on the surface of titanium. Unique structures in size of nano scale were fabricated. There optical properties and hydrophobicity were studied and concluded. These precise structures can be used in biomedical applications and biosensors where controllability of the desired hydrophobic and hydrophilic properties is an essential and it is not currently being achieved with conventional methods.

6.3 Conclusions

The following conclusions can be drawn from the research undertaken:

1. Nicobar pigeon (*Caloenas Nicobarica*) is a unique bird that has a range of colour shades recorded with changing viewing and illumination angles at different locations of the feathers. This spectacular variation in colours is generated by internal photonic structures; red, green and blue and their blends.

2. Nicobar pigeon feather showed a contact angle of ~ 156° demonstrating it to be super hydrophobic.

3. Nicobar pigeon feather showed an optical response with a redshift in optical spectra with increasing refractive index of the solution, which was correlated with concentration values. It is anticipated that the structural coloration in Nicobar pigeon can be adopted for many practical applications such as colour selective filters, non-reflecting coatings, photonic bandgap hydrogel sensors and refractive index based sensing.

4. Himalayan Monal feathers exhibit poor hydrophobic properties in contrast to that generally attributed to the avian species - the proximal end showed a contact angle between 93° to 110°, whereas a contact angle between 113° to 120° was observed on the distal end of a feather. The iridescent distal end of the feather had decreased hydrophobicity when compared

to the proximal end with no colour. This phenomenon can be attributed to the internal change in the photonic structure of the feather where a change in dimensions of the structure or structured and non-structured areas has an effect on the hydrophobicity of the feather.

5. Himalayan Monal feather showed an instant colour change on addition of a water droplet of size 2 μl, as well as reversing to its original colour within five minutes of drying period. This is suggested to be due to swelling of the keratin layer of barbules, with the absorption of liquid.

6. Refractive index sensing spectra recorded from Himalayan Monal feather showed that the structure could sense changes in refractive index of alcohols more effectively than water-based solutions, suggesting swelling of keratin by water-based solutions having a more prominent effect on the structure. The structural coloration in Himalayan Monal can possibly be adopted for many practical applications such as colour selective filters, thin film capacitive sensors, hydrogel photonic bandgap sensors and other nano-photonic devices.

7. The novel optical device based on grating period of 700-1300 nm modelled was compared for both silicon (Si) and silicon dioxide (SiO2) materials to determine the behaviour of light interaction with the structures. A conclusion is made that a multimaterial grating has the same diffraction efficiency as that of a grating formed in a single material, but had the advantage of having an ordered relationship between the grating dimensions (thickness and period) and the intensity of reflected and diffracted optical wavelengths.

8. The modelled optical device based on SiO2 grating structure demonstrated a colour-selective feature with grating periods of 800 nm and 1000 nm, respectively. A high diffraction efficiency was measured for the green wavelength region as compared to other colours in the spectrum for 800 nm grating periodicity; whereas wavelengths within the red region of spectrum interfered constructively for the grating with 1000 nm periodicity resulting a higher

efficiency for red colour bandwidth. The results show that diffraction effects can be enhanced by the thin-film interference phenomenon to produce colour selective optical devices.

9. Nanostructures with different shape and dimensions such as circular ring structures, 1D and 2D grating with different periods fabricated on titanium surface using a fast direct laser interference patterning method demonstrated changes in their hydrophobicity. The size, shape and surface roughness of these nanostructures are the parameters to control the wettability and hydrophobicity properties required for any specific application.

10. 1D grating structures allowed the flow of water droplet through the spacing acting like nanochannels: the observed contact angle was within the range of ~ 30° to 64°. Similar behavior was noticed in the case of 2D square and rectangular structures but they showed more hydrophilic properties as compared to 1D grating patterns, giving the lowest contact angle of ~ 20°, and the highest value of ~ 62°.

11. The circular ring Fresnel structures showed less hydrophilic properties and more hydrophobic properties with contact angles ranging from ~ 35° to a maximum of ~ 74°.

12. An increase in the height of the structures increased the contact angles whereas an increase in spacing decreased the contact angles allowing more hydrophilic properties.

13. An increase in energy used for ablation increased the contact angle at the surface. Lower energy of 30 mJ, when used for ablation, showed the same effect as if the surface was just porous whereas higher energy of 210 mJ ablated the material with more precision, higher depths and smoother surface profile which resulted in increase in the contact angles of the fabricated structures.

14. A desirable level of hydrophobicity can be achieved by controlling these parameters. These titanium surfaces have possible use in bio medical applications and biosensors where

controllability of the desired hydrophobic and hydrophilic properties is an essential and it is not currently being achieved with conventional methods.

6.4 Limitations

1. There are limitations in simulation modelling of these optical nanostructures. Finite element method (FEM) can handle complex geometries but it can give only approximate solutions. It has inherent errors. The input errors from users can be fatal. Complex mesh and numerical integrations require extra time and memory. The accuracy in measurements strongly depend on the mesh size and orientation. Lowering the mesh size can give inaccurate solutions.

2. There are limitations in fabrication of optical nanostructures for the proposed use in hydrogel photonic bandgap sensors. The nanosecond laser ablation fabrication can produce melted zone. It is less suitable for precise or direct laser cutting, mass production and commercialization.

3. There are limitations in existing hydrogel sensors such as mechanical strength, response time, saturation and efficiency of the sensor. The proposed optical nanostructure integrated hydrogel photonic bandgap sensor will have all those limitations. However, there will be huge improvements in response time and efficiency due to the integrated photonic bandgap structure. Hydrogel sensors and contact lenses can also easily get damaged with repeated usage. This can cause irreversible deformation and lead to low performance.

6.5 Future Work

For future work, several interesting directions can be carried based on works in this thesis, especially simulating and fabricating the 3D volumetric nanostructures with their respective material properties is still a challenge. Fibre like structures need to be simulated and fabricated to adopt the behaviour as of Himalayan Monal feathers to test changes with a visual colour change. Highly sophisticated and modern techniques are needed for fabrication and creating

materials with such properties to show the change. Hydrogel methods such as hydrogel based photonic bandgap sensors and contact lenses can be adopted for fabricating patch sensors but achieving the optical visual change is a challenge. Fabricating optical micro and nano cavities with such precision is a challenge. Filling them with dyes or with materials with high contrast in refractive indices is a challenge. Dyes that show change in colour with change in pH such as phenol red or red cabbage dye are biocompatible. They can be trapped in these nanostructures cavities to show visual optical changes. These type of sensors can be used in food and cosmetics or any applications where pH change takes place. So far, time and temperature dependant non reversible materials are being used in this industry where measurements are not very accurate and lot of food products are thrown away and wasted without knowing the real time measurements.

Another possible direction is to fabricate these 3D volumetric nanostructures into contact lenses with very precise material properties and dyes trapped which are biologically compatible. These special contact lenses will be able to detect and show a visual change in colour if any pH changes take place in the eye. They are physically in contact with the eye for long period of time and can be used as continuous biomarkers or indicators. Smart contact lenses for continuous glucose monitoring can be developed and tested using eye tear solution under the physiological conditions. Smart phone apps can be adopted to record the optical outputs for monitoring purposes. More research work is needed to be done to fabricate such contact lenses.

Related Publications

- Ijaz Rashid, Muhammad Umair Hassan, Abbas Khandwalla, Rayan Mohammed Ameen, Ali Kemal Yetisen, Qing Dai, Haider Butt. (2018). *"Structural Coloration in Caloenas Nicobarica Pigeons and Refractive Index Modulated Sensing."* Advanced Optical Materials 6(9): 1701218.

- Ijaz Rashid, Muhammad Umair Hassan, Muhammad Nazim, Qing Dai, Kamran Khattak and Haider Butt*. *"Structural colouration in Himalayan Monal, hydrophobicity and refractive index modulated sensing."* (In process)

- Ijaz Rashid, Haider Butt*, Ali K. Yetisen, Bruno Dlubak, James E. Davies, Pierre Seneor, Aymeric Vechhiola, Faycal Bouamrane, and Stephane Xavier. (2017*). "Wavelength-Selective Diffraction from Silica Thin-Film Gratings."* ACS Photonics 4(10): 2402-2409

- Ijaz Rashid, Muhammad Umair Hassan, Affar S. Karimullah, Badar Alqattan Haider Butt. *"Nanopatterned Surfaces for Modulating Hydrophobic Properties of Titanium."* (In process)

Appendix A

1. Refractive index table

Liquid	Refractive index
Isopropanol	1.38
Ethanol	1.36
Glycerol	1.47
20 mM Glucose	1.36
200 mM Glucose	1.58
Water	1.33

Table S1. *Refractive indices of liquids*

2. Silica Thin-Film Colour Chart

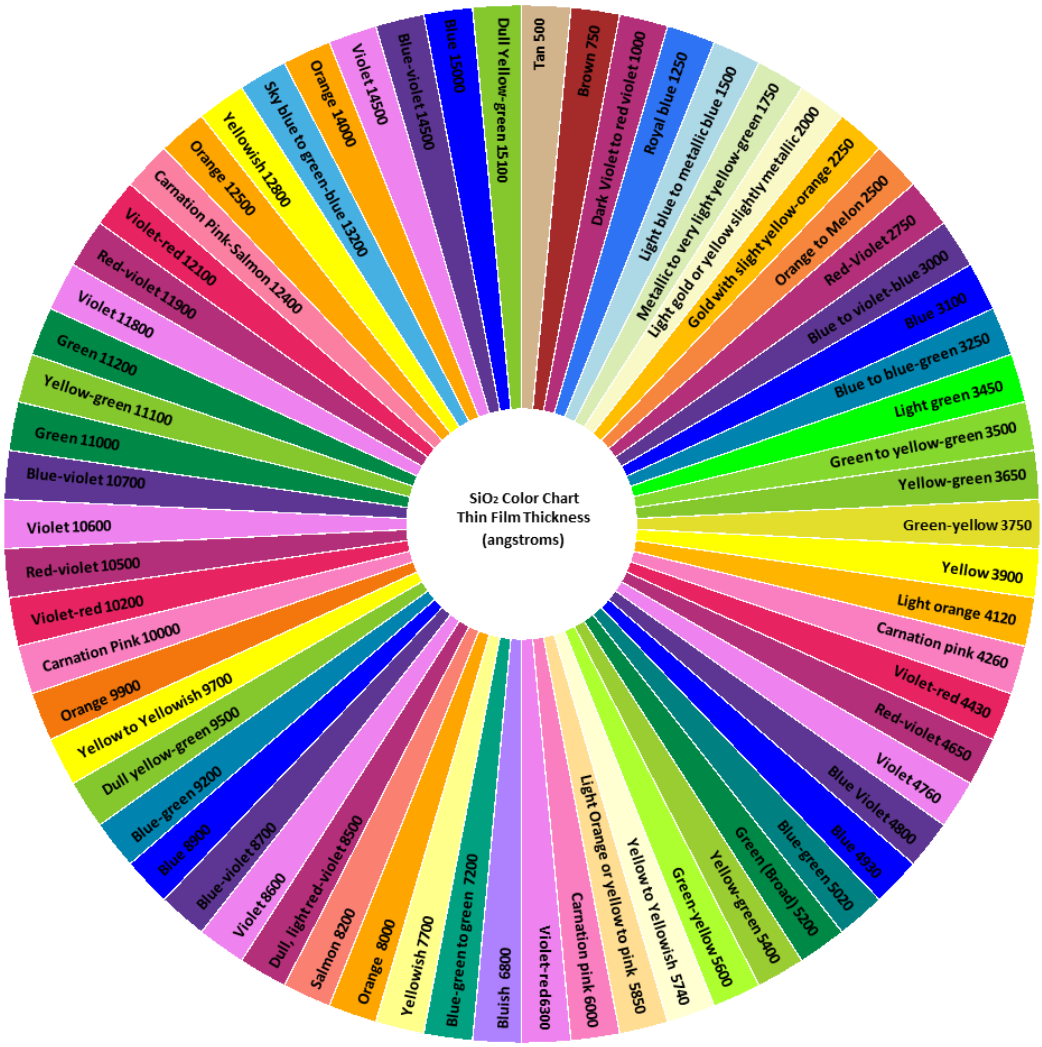

Figure S1. Silicon dioxide thin film colour chart. (Ref. 1)

Reference

1. Pleil, M.W., *Plug and Play Microsystems (MEMS) Technology into an Engineering and Technology Program.*

Appendix B

1. MATLAB Code for thin films

Equations used for coding:

For change in path length. Extra path length travelled. $\delta = \frac{2\pi}{\lambda} * n * t$

Fresnel reflection at interface 1 $r_1 = \frac{n_1 - n_2}{n_1 + n_2}$

Fresnel reflection at interface 2 $r_2 = \frac{n_2 - n_3}{n_2 + n_3}$

Sum of reflection amplitude $A_r = \frac{r_1 + r_2 e^{-2i\delta}}{1 + r_1 r_2 e^{-2i\delta}}$

Total reflection coefficient 'R' $R = A_r . A_r^*$

```
clear
t = 300;                          % thin film thickness
lambda = (300:5:600);
n1 = 1;
n2 = 1.45+0*1i;
n3 = 3.47;
del = (2*pi./lambda)*n2*t;        % del is change in path length
r1 = (n1-n2)/(n1+n2);             % reflection at interface 1
r2 = (n2-n3)/(n2+n3);             % reflection at interface 2
r =  (r1+r2.*exp(-2*1i.*del))./(1+r1*r2.*exp(-2*1i.*del));
% reflection amplitude and phase in 'i' direction
R = r.*conj(r);                   % total reflection 'R'
figure(1);
hold on;
plot(lambda,R,'b-*') ;
xlabel('Wavelength (nm)');
title(['Thickness= 300, 345,400,443,500, 540, 585',', n1=',num2str(n1)',', n2=',
num2str(n2),', n3=', num2str(n3)]);
ylabel('R');
t = 345;                  % thin film thickness value changed
lambda = (300:5:600);
n1 = 1;
n2 = 1.45+0*1i;
n3 = 3.47;
del = (2*pi./lambda)*n2*t;
r1 = (n1-n2)/(n1+n2);
r2 = (n2-n3)/(n2+n3);
r =  (r1+r2.*exp(-2*1i.*del))./(1+r1*r2.*exp(-2*1i.*del));
R = r.*conj(r);
figure(1);
```

```
hold on;
plot(lambda,R,'m-x') ;
xlabel('Wavelength (nm)');
title(['Thickness= 300, 345,400,443,500, 540, 585',', n1=',num2str(n1)',', n2=',
num2str(n2),', n3=', num2str(n3)]);
ylabel('R');
t = 400;
lambda = (300:5:600);
n1 = 1;
n2 = 1.45+0*1i;
n3 = 3.47;
del = (2*pi./lambda)*n2*t;
r1 = (n1-n2)/(n1+n2);
r2 = (n2-n3)/(n2+n3);
r =  (r1+r2.*exp(-2*1i.*del))./(1+r1*r2.*exp(-2*1i.*del));
R = r.*conj(r);
figure(1);
hold on;
plot(lambda,R,'g-p') ;
xlabel('Wavelength (nm)');
title(['Thickness= 300, 345,400,443,500, 540, 585',', n1=',num2str(n1)',', n2=',
num2str(n2),', n3=', num2str(n3)]);
ylabel('R');
t = 445;
lambda = (300:5:600);
n1 = 1;
n2 = 1.45+0*1i;
n3 = 3.47;
del = (2*pi./lambda)*n2*t;
r1 = (n1-n2)/(n1+n2);
r2 = (n2-n3)/(n2+n3);
r =  (r1+r2.*exp(-2*1i.*del))./(1+r1*r2.*exp(-2*1i.*del));
R = r.*conj(r);
figure(1);
hold on;
plot(lambda,R,'k-+') ;
xlabel('Wavelength (nm)');
title(['Thickness= 300, 345,400,443,500, 540, 585',', n1=',num2str(n1)',', n2=',
num2str(n2),', n3=', num2str(n3)]);
ylabel('R');
t = 500;
lambda = (300:5:600);
n1 = 1;
n2 = 1.45+0*1i;
n3 = 3.47;
del = (2*pi./lambda)*n2*t;
r1 = (n1-n2)/(n1+n2);
r2 = (n2-n3)/(n2+n3);
```

```
r =  (r1+r2.*exp(-2*1i.*del))./(1+r1*r2.*exp(-2*1i.*del));
R = r.*conj(r);
figure(1);
hold on;
plot(lambda,R,'r-d') ;
xlabel('Wavelength (nm)');
title(['Thickness= 300, 345,400,443,500, 540, 585',', n1=',num2str(n1)',', n2=',
num2str(n2),', n3=', num2str(n3)]);
ylabel('R');
t = 540;
lambda = (300:5:600);
n1 = 1;
n2 = 1.45+0*1i;
n3 = 3.47;
del = (2*pi./lambda)*n2*t;
r1 = (n1-n2)/(n1+n2);
r2 = (n2-n3)/(n2+n3);
r =  (r1+r2.*exp(-2*1i.*del))./(1+r1*r2.*exp(-2*1i.*del));
R = r.*conj(r);
figure(1);
hold on;
plot(lambda,R,'y-s') ;
xlabel('Wavelength (nm)');
title(['Thickness= 300, 345,400,443,500, 540, 585',', n1=',num2str(n1)',', n2=',
num2str(n2),', n3=', num2str(n3)]);
ylabel('R');
t = 585;
lambda = (300:5:600);
n1 = 1;
n2 = 1.45+0*1i;
n3 = 3.47;
del = (2*pi./lambda)*n2*t;
r1 = (n1-n2)/(n1+n2);
r2 = (n2-n3)/(n2+n3);
r =  (r1+r2.*exp(-2*1i.*del))./(1+r1*r2.*exp(-2*1i.*del));
R = r.*conj(r);
figure(1);
hold on;
plot(lambda,R,'c-o') ;
xlabel('Wavelength (nm)');
title(['Thickness= 300, 345,400,443,500, 540, 585',', n1=',num2str(n1)',', n2=',
num2str(n2),', n3=', num2str(n3)]);
ylabel('R');
```

2. MATLAB Code for diffraction equation with variation in refractive index.

Equation used for coding:

Diffraction equation $dn_{eff}sin(\theta) = m\lambda$

Re-arranged to calculate theta $\theta = \sin^{-1}\left(\frac{m\lambda}{n_{eff*d}}\right)$

```
clear
d = 800;                        % grating period
lamda = (400:5:750);
Neff = 1.0;                     % effective refractive index
m = 1;
x = (m*lamda)./(d*Neff);        % diffraction equation
theta = asind(x);             % calculating diffraction angle
figure(1);
hold on;
plot(lamda,theta,'b-*');
xlabel('Wavelength (nm)');
ylabel('Angle');

d = 800;
lamda = (400:5:750);
Neff = 1.05;                  % Change in value of effective refractive index
m = 1;
x = (m*lamda)./(d*Neff);
theta = asind(x);
figure(1);
hold on;
plot(lamda,theta,'m-x');
xlabel('Wavelength (nm)');
ylabel('Angle');

d = 800;
lamda = (400:5:750);
Neff = 1.15;
m = 1;
x = (m*lamda)./(d*Neff);
theta = asind(x);
figure(1);
hold on;
plot(lamda,theta,'g-p');
xlabel('Wavelength (nm)');
ylabel('Angle');
```

```
d = 800;
lamda = (400:5:750);
Neff = 1.2;
m = 1;
x = (m*lamda)./(d*Neff);
theta = asind(x);
figure(1);
hold on;
plot(lamda,theta,'k-+');
xlabel('Wavelength (nm)');
ylabel('Angle');

d = 800;
lamda = (400:5:750);
Neff = 1.225;
m = 1;
x = (m*lamda)./(d*Neff);
theta = asind(x);
figure(1);
hold on;
plot(lamda,theta,'r-d');
xlabel('Wavelength (nm)');
ylabel('Angle');

d = 800;
lamda = (400:5:750);
Neff = 1.25;
m = 1;
x = (m*lamda)./(d*Neff);
theta = asind(x);
figure(1);
hold on;
plot(lamda,theta,'y-s');
xlabel('Wavelength (nm)');
ylabel('Angle');

d = 800;
lamda = (400:5:750);
Neff = 1.275;
m = 1;
x = (m*lamda)./(d*Neff);
theta = asind(x);
figure(1);
hold on;
plot(lamda,theta,'c-o');
xlabel('Wavelength (nm)');
ylabel('Angle');
```

Appendix C

COMSOL Simulation Modelling Procedure

MODEL WIZARD

1 Open COMSOL Multiphysics 5.1.

2 Click on the Model Wizard.

3 Click on the 2D button.

4 Click on the Optics module.

5 Click on the Electromagnetic Waves, Frequency Domain (ewfd).

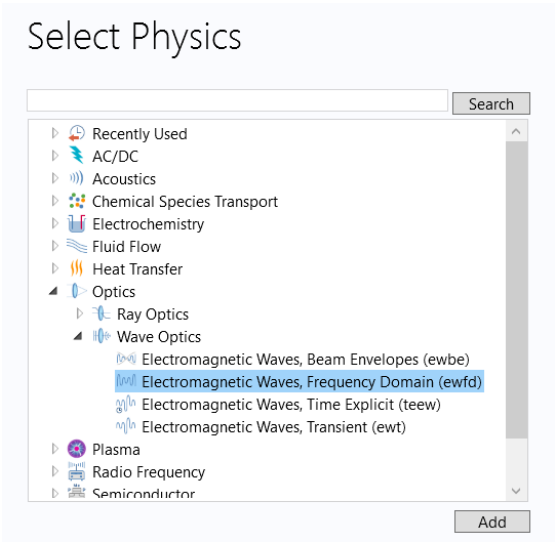

6 Click Add.

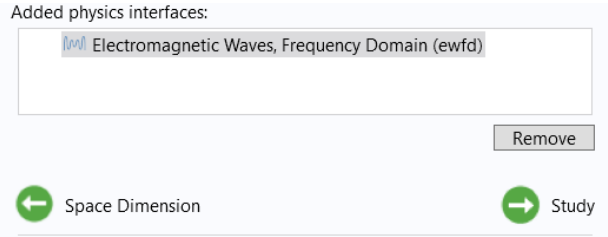

7 Click on the Study button.

8 Click on the Frequency Domain in the Preset Studies tree and now Click Done.

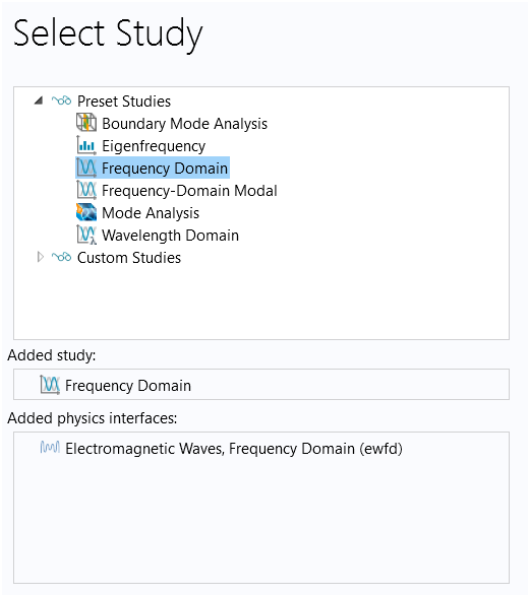

GLOBAL DEFINITIONS

1 In the Model Builder window, right-click on Global Definitions and select Parameters.

2 Input the following: lambda0 650[nm] Wavelength (Red Beam).

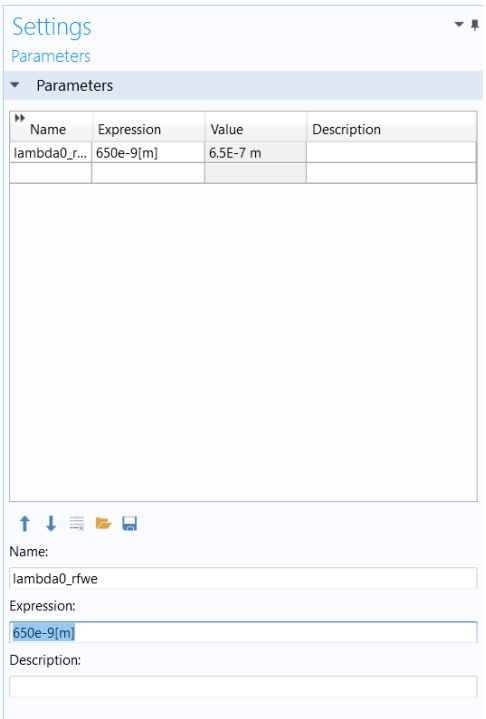

GEOMETRY

1 In the Model Builder window, right-click Geometry 1.

2. Add Rectangles with respective width, height and position.

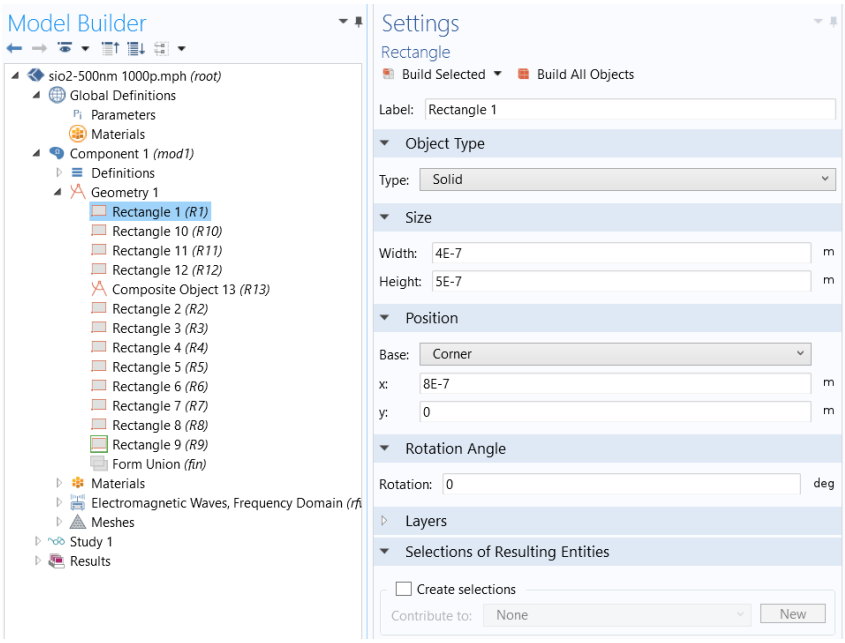

3 Model Builder window and select Rectangle. Click on Rectangle 1 in the Model Builder window and under the Position section input values. Similarly select a circle.

4 In the Operations section of the toolbar, select Intersection. Click on both the rectangle and circle in the Graphics window (highlighting both), then click on the Build All Objects button in the Intersection window.

5 Repeat part 3 within this section to draw more rectangles acting as grating as shown below and join them.

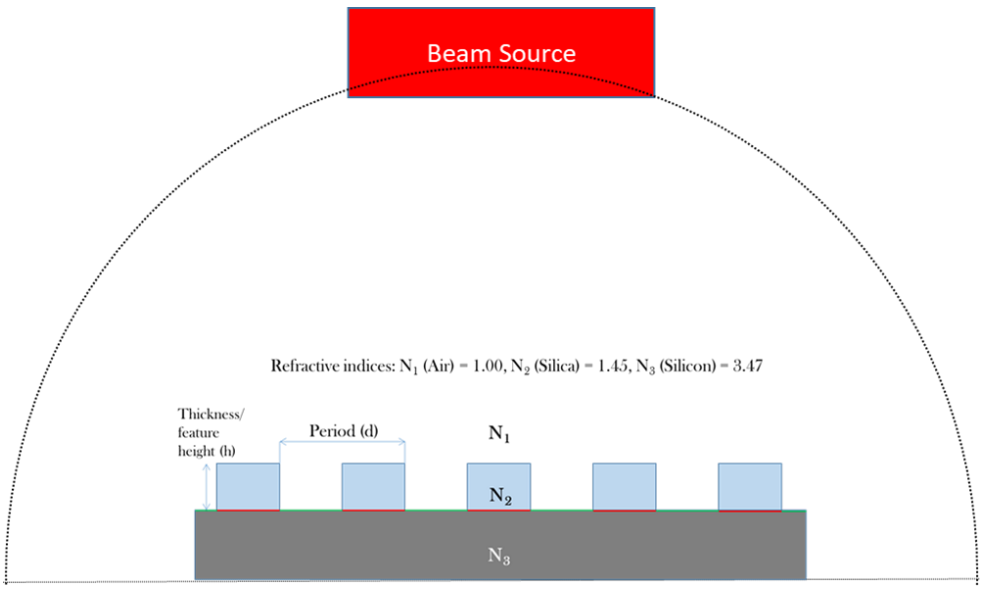

MATERIALS

Material 1 – Air

Material 2– Silica

Material 3 – Silicon

1 In the Model Builder window, right-click on Materials section and select New Material (Material 1).

2 In the Selection box select All domains, then manually remove Domains by clicking on it in the Selection box and clicking the Remove from selection button (minus symbol). Only domains for Material 1 should be highlighted.

3 In the Material window open the Material Properties list and then open the Electromagnetic Models tree. Click on Refractive Index and then click on the plus symbol or Add to selection button.

4 Input ‘real(nm)’ for Refractive Index and ‘imag(nm)’ for Refractive Index, Imaginary part in the Material Contents box.

5 Right-click on Material 1 under the Material section in the Model Builder window and click Rename as ‘Air’. Similarly add other materials for corresponding domains.

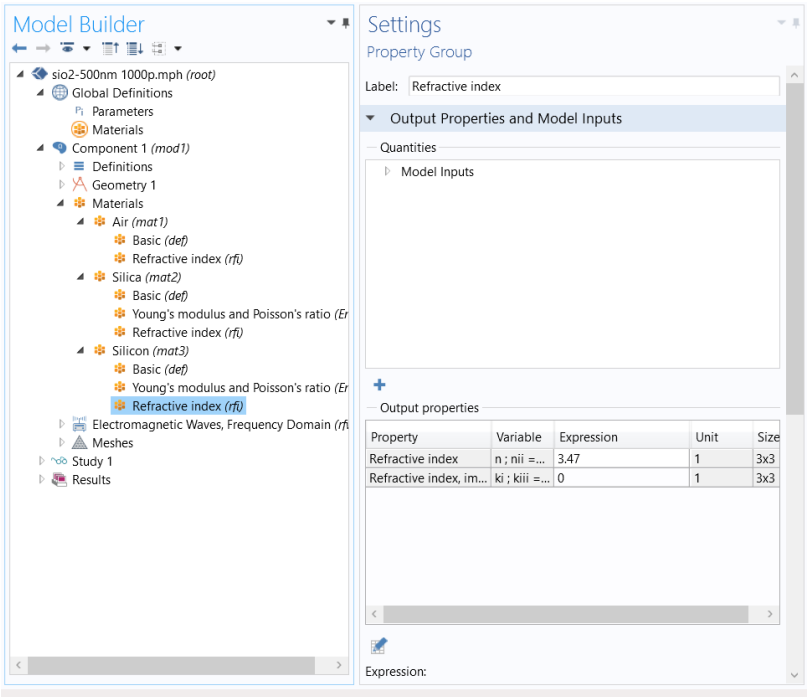

ELECTROMAGNETIC WAVES, FREQUENCY DOMAIN

Wave Equation, Electric 1

1 In the Model Builder window, find the section labelled Wave Equation, Electric 1 under the Electromagnetic Waves, Frequency Domain (ewfd) section in the Model Builder window.

2 Under the Electromagnetic Displacement Field check that the box labelled Electromagnetic Displacement Field Model is set to Refractive Index (Relative permittivity).

Scattering Boundary Condition 1

1 In the Model Builder window, right-click the field Electromagnetic Waves, Frequency Domain (ewfd) and pick Scattering Boundary Condition.

2 Find the Boundary Selection section in the Scattering Boundary Condition settings window. Similar to the domain selecting process used for material, choose all the boundaries except the top beam source boundary and enter zero for Ex, Ey and Ez.

Scattering Boundary Condition 2

1 Repeat step 1 from the section ‘Scattering Boundary Condition 1.

2 Repeat step 2 from the section ‘Scattering Boundary Condition 1’ but now only set the top beam source boundary.

3 Find the Scattering Boundary Condition section in the settings window and set the Ez value to 1 (leaving the Ex and Ey at 0).

Mesh 1

1 In the Model Builder window click on Mesh 1.

2 In the Mesh Settings window, set the Element Size.

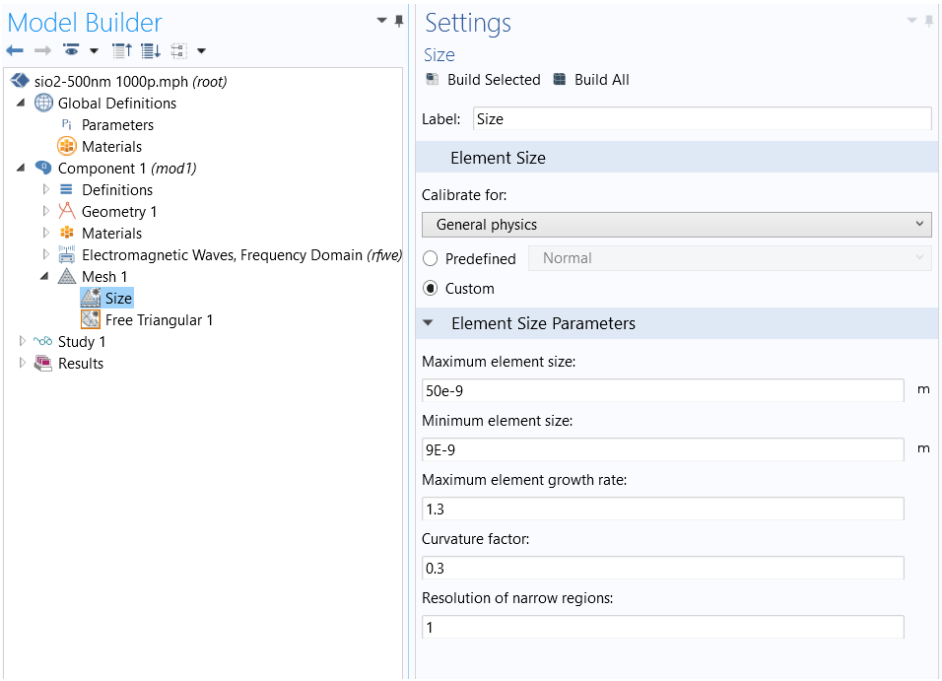

STUDY 1 Parametric Sweep

1 Right-click on Study 1 in the Model Builder window and select Parametric Sweep.

2 In the Parametric Sweep Study Settings window, click on the Add button and a drop down box should appear.

3 Select ‘lambda0 (Wavelength)’ in the Parameter Names box.

4 In the Parameter Value List box input the following: “445[nm],532[nm],650[nm]”.

5 In the Parametric Sweep Study Settings window, click on the Add button and a drop down box should appear.

6 Click on the Study ribbon (lining the top of the page) and click the Compute button.

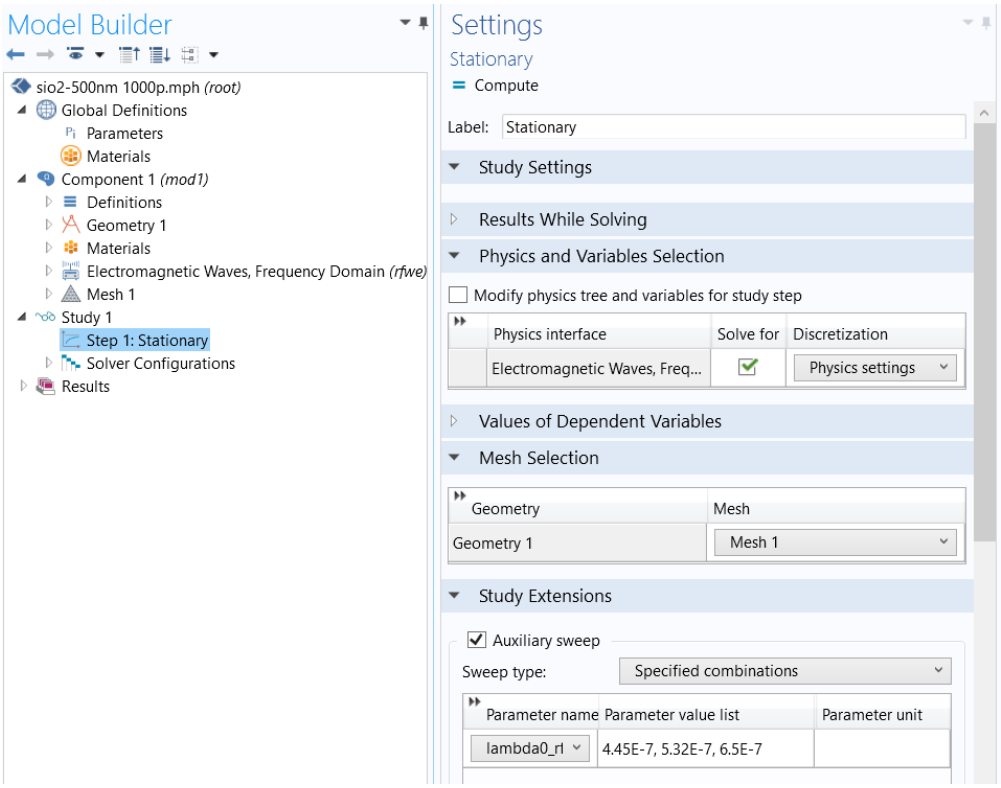

RESULTS

Data Sets

1 Right-click on Data Sets in the Results section and select Cut Line 2D.

2 Under the Data section set the Data Set to Solution 1.

3 Set the Data set to Cut Line 2D 1.

4 Under the Expression section click on the Replace expression button and locate and select Power outflow, time average.

5 Check that under the Integration Settings section that the Method is of Integration and the Integration order is set to 2.

Electric Field (ewfd)

1 In the Results section of the Model Builder window, locate and right-click Electric Field (ewfd) and select Surface 1 At the top of the Surface settings box check that the Data set is of Solution 1

1D Plot Group 1

1 Right-click the Results section and click the 1D Plot Group

2 Right Click on 1D Plot Group and select Point Graph.

3 Set the Data Set to Integral 1

4 Set the y-Axis Data expression to Power outflow, time average

5 Under the x-Axis Data section set the Parameter to Expression and then in the box below input “lambda0”.

6 Click Plot at the top of the Point Graph window

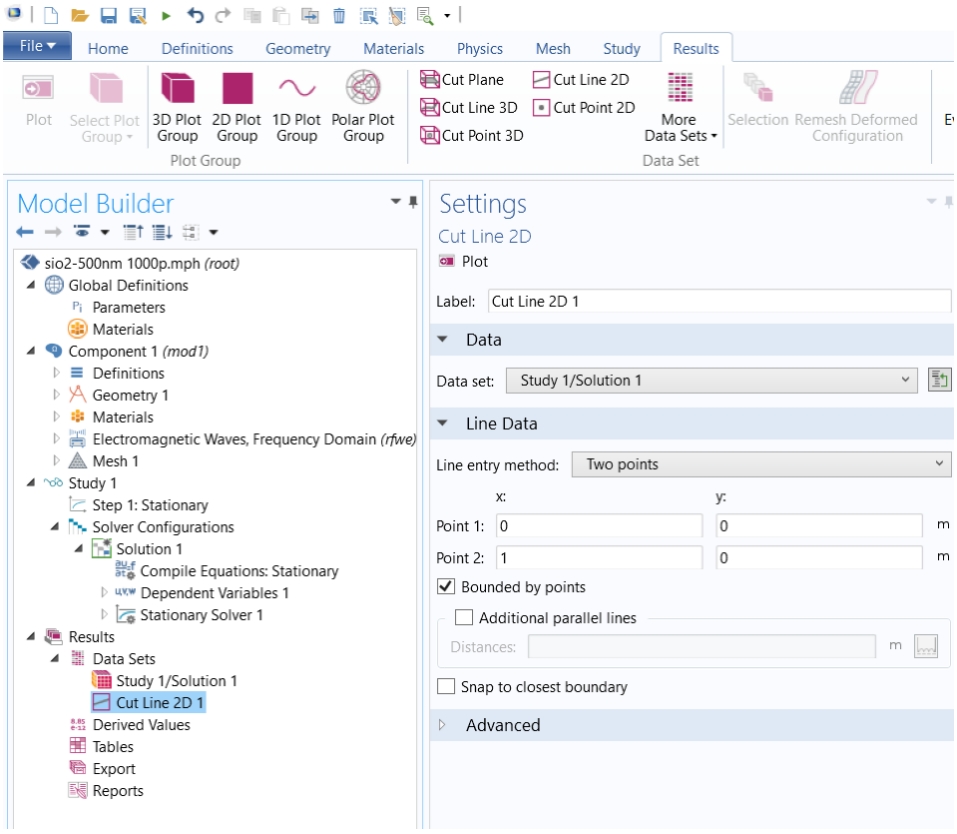

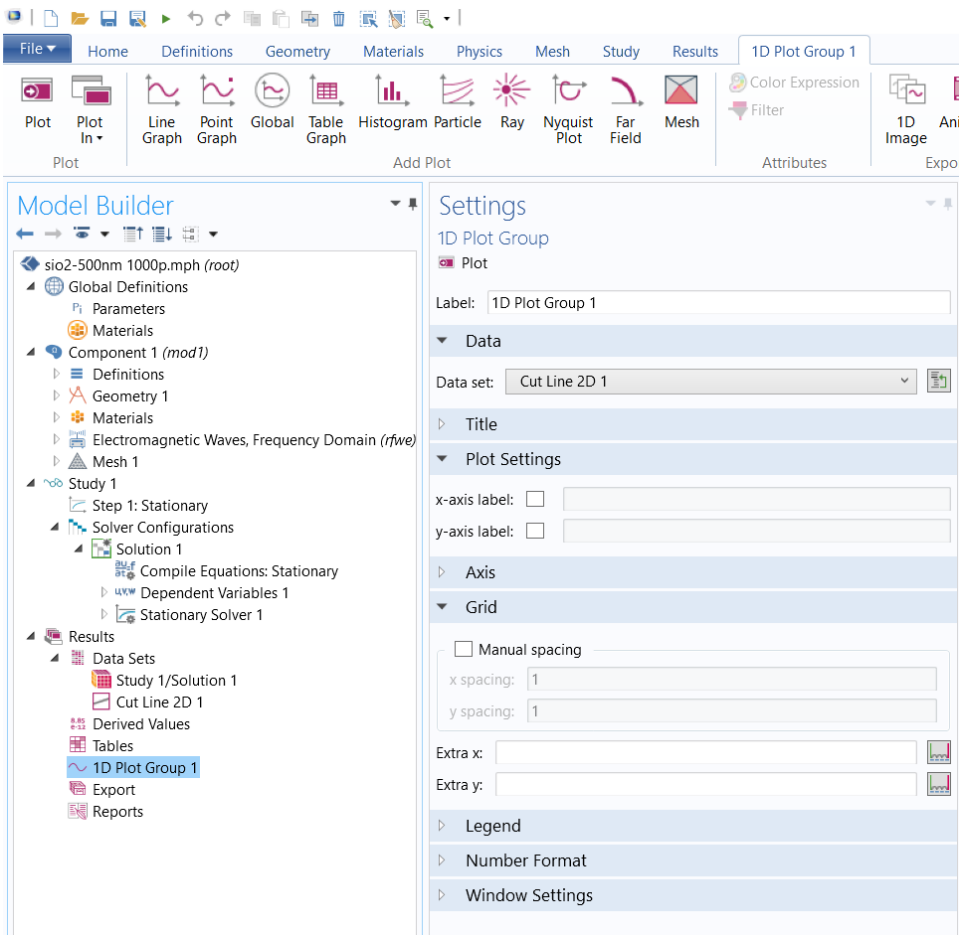
File
Home
Definitions
Geometry
Materials
Physics
Mesh
Study
Results
1D Plot Group 1
Plot
Plot In
Line Graph
Point Graph
Global
Table Graph
Histogram
Particle
Ray
Nyquist Plot
Far Field
Mesh
Color Expression
Filter
1D Image
Plot
Add Plot
Attributes
Model Builder
sio2-500nm 1000p.mph (root)
Global Definitions
Parameters
Materials
Component 1 (mod1)
Definitions
Geometry 1
Materials
Electromagnetic Waves, Frequency Domain (rfwe)
Mesh 1
Study 1
Step 1: Stationary
Solver Configurations
Solution 1
Compile Equations: Stationary
Dependent Variables 1
Stationary Solver 1
Results
Data Sets
Study 1/Solution 1
Cut Line 2D 1
Derived Values
Tables
1D Plot Group 1
Export
Reports
Settings
1D Plot Group
Plot
Label: 1D Plot Group 1
Data
Data set: Cut Line 2D 1
Title
Plot Settings
x-axis label:
y-axis label:
Axis
Grid
Manual spacing
x spacing: 1
y spacing: 1
Extra x:
Extra y:
Legend
Number Format
Window Settings

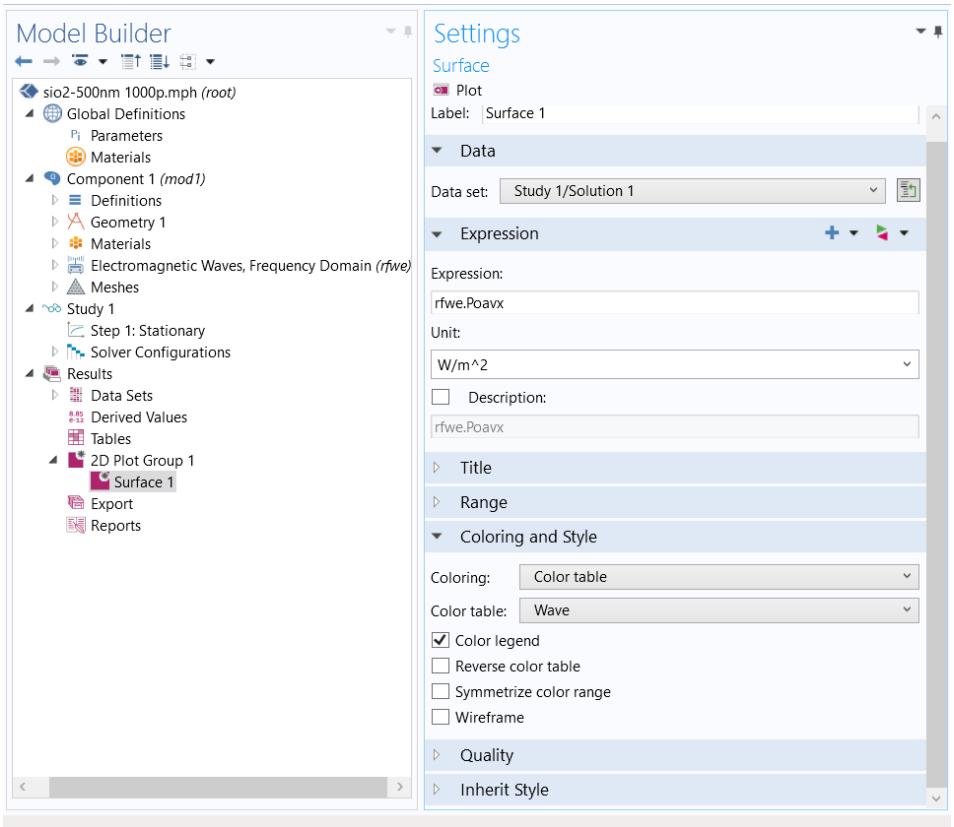
Model Builder
sio2-500nm 1000p.mph (root)
Global Definitions
Parameters
Materials
Component 1 (mod1)
Definitions
Geometry 1
Materials
Electromagnetic Waves, Frequency Domain (rfwe)
Meshes
Study 1
Step 1: Stationary
Solver Configurations
Results
Data Sets
Derived Values
Tables
2D Plot Group 1
Surface 1
Export
Reports
Settings
Surface
Plot
Label: Surface 1
Data
Data set: Study 1/Solution 1
Expression
Expression:
rfwe.Poavx
Unit:
W/m^2
Description:
rfwe.Poavx
Title
Range
Coloring and Style
Coloring: Color table
Color table: Wave
Color legend
Reverse color table
Symmetrize color range
Wireframe
Quality
Inherit Style

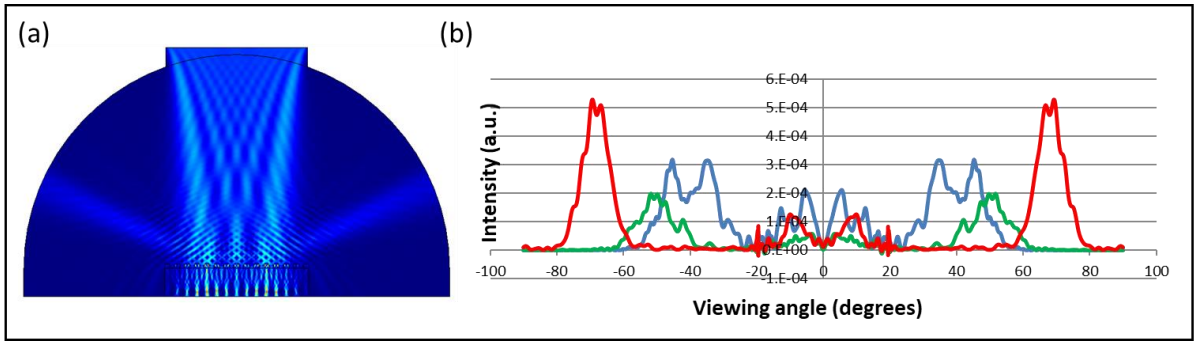

Figure S2. Plots display **(a)** Surface Plot (**b)** Angle versus Intensity plot for red, green and blue wavelengths